BOSTON UNIVERSITY

COLLEGE OF ENGINEERING

Dissertation

DIFFUSE AND NONLINEAR IMAGING FOR IN VIVO MONITORING OF STRUCTURE AND FUNCTION IN PRECLINICAL TUMORS

by

KAVON KARROBI

B.S., Boston University, 2014
M.S., Boston University, 2018

Submitted in partial fulfillment of the

requirements for the degree of

Doctor of Philosophy

2020

© 2020 by
KAVON KARROBI
All rights reserved, except for
Chapter 3 – All except 3.7.2, 3.7.3 © 2019 WILEY-VCH
Chapter 3 – Part 3.7.2 © 2018 SPIE
Chapter 3 – Part 3.7.3 © 2018 OSA

Approved by

First Reader

Darren Roblyer, Ph.D.
Associate Professor of Biomedical Engineering

Second Reader

Muhammad H. Zaman, Ph.D.
Professor of Biomedical Engineering
Professor of Materials Science and Engineering
Professor, Howard Hughes Medical Institute

Third Reader

Hadi T. Nia, Ph.D.
Assistant Professor of Biomedical Engineering

Fourth Reader

Thomas G. Bifano, Ph.D.
Professor of Mechanical Engineering
Professor of Materials Science and Engineering
Professor of Biomedical Engineering

Fifth Reader

David J. Waxman, Ph.D.
Professor of Biology
Professor of Medicine
Professor of Biomedical Engineering

DEDICATION

To Baba, Mom, Biji, Grandma, and Popo

ACKNOWLEDGMENTS

To Darren, our mentor-mentee relationship began when I first took your class, BE 511 Biomedical Instrumentation, as an undergraduate BME senior and since then it has been nothing short of nurturing, fruitful, and educational. Despite having little to no background in biomedical optics, you welcomed me into your lab with plenty of excitement and enthusiasm, and with your never ending support, guidance, and encouragement I was able to successfully navigate what was at first unfamiliar territory and eventually came to call the wonderful biomedical optics field and community my research home. Thank you for this enriching opportunity and experience, and above all else, thank you for your belief and confidence in me. I am truly grateful for the time we have had together and to have you as a mentor, and I very much look forward to our continued relationship in the years to come.

To my undergraduate research mentors, Tyrone Porter and Peter Duesberg, thank you for providing me with a strong research foundation to pursue a Ph.D. and beyond, and for your continued support and mentorship.

To my senior graduate research mentors, Irving Bigio and David Waxman, thank you for lending me your tremendous wisdom during my graduate studies.

To the rest of my committee members, including Muhammad Zaman, Tom Bifano, and Hadi Nia, thank you for your helpful insights, encouragement, and for pushing me to think critically about my work.

To all the official and honorary BOTLab members I have had the pleasure of getting to know, thank you for being a wonderful bunch to work with! In particular, I would like to thank those who helped with this work including: Anup, Matt, Cam, Syeda, Vivian, Kshama, and Asha. I would also like to thank the postdocs (Matt, Vivian, and Kshama) for being exceptional research role models for us graduate students.

To the BU BME community, I could not have asked for a more stimulating and friendlier environment to pursue my undergraduate and graduate education! Thank you to the following people for all of their administrative support, kindness, and patience throughout my graduate studies: Christen L. Bailey, Allie Gustin, Stephanie Johnson, Will Reich, Tara Sorrentino, and the BU animal facility folks including David Cawston.

To my undergraduate and graduate friends, thank you for making my journey at BU extremely memorable, especially my sushi amigo Samer Bou Jawde.

Most of all, to my loving family and Poling. Your sacrifices, support, love, and encouragement have made all of this possible. Thank you to my parents who have given me everything I have and for always believing in me – without a doubt, all of my accomplishments are yours. Poling, thank you for always being by my side – I am extremely fortunate to have you in my life. Finally, Baba, I will never forget how this all started with a simple conversation in the car before you dropped me off for my first day of school and what turned out to be a lifelong pursuit of knowledge.

DIFFUSE AND NONLINEAR IMAGING FOR IN VIVO MONITORING OF STRUCTURE AND FUNCTION IN PRECLINICAL TUMORS

KAVON KARROBI

Boston University College of Engineering, 2020

Major Professor: Darren Roblyer, Ph.D., Associate Professor of Biomedical Engineering

ABSTRACT

Diffuse Optical Imaging (DOI) technologies provide metabolic and hemodynamic information in tissue in a label-free manner using non-harmful near infrared light. Recently, DOI techniques have received significant interest as a non-invasive functional imaging tool for monitoring patient response to cancer therapies in the clinic. A number of reports have demonstrated that DOI can determine response within hours to weeks from the start of treatment. Despite these promising results, the potential impact, and ultimately adoption of DOI for cancer therapy monitoring in the clinic is limited in part by the lack of knowledge of the cellular, molecular, and biological origins of these clinical observations. Knowledge of the biological underpinnings of DOI response markers is likely to provide clinically relevant insights that can be used to manage and personalize cancer treatment strategies. To this end, the work presented in this dissertation was focused on developing methodology and instrumentation for a novel preclinical imaging technique called Diffuse and Nonlinear Imaging (DNI). DNI combines functional measurements of tumors obtained by wide-field DOI with the underlying tumor biology captured with intravital Multiphoton Microscopy (MPM). Specifically, DNI combines MPM with the DOI technique Spatial

Frequency Domain Imaging (SFDI) to provide multiscale datasets of tumor microvascular architecture coregistered within wide-field hemodynamic maps. A procedure was developed to image small animal tumor models with high x-y spatial coregistration accuracy and precision between SFDI and MPM, along with a novel method to match the imaging depths of both modalities by utilizing informed SFDI spatial frequency selection. A preliminary in vivo DNI study of murine mammary tumors revealed multiscale relationships between tumor oxygen saturation and microvessel diameter, and tumor oxygen saturation and microvessel length. Based on these encouraging results, an integrated DNI instrument was then designed and fabricated to acquire tumor vascular structure and function datasets in an inherently spatially coregistered manner from a single system, while simultaneously increasing the sampling resolution of functional spatial heterogeneity. Finally, a small longitudinal study was conducted with the DNI system to explore multiscale relationships between tumor vascular structure and function over space and time in different tumor models and treatment regimens. In summary, the work described in this dissertation resulted in a new method to investigate the relationships between clinically translational DOI hemodynamic markers and MPM metrics of vascular architecture. Ultimately, this work will help to pave a path towards DOI for personalized and precision medicine to significantly impact and inform adaptive therapy strategies tailored to the in vivo state of each patient's tumor.

TABLE OF CONTENTS

LIST OF TABLES

LIST OF FIGURES

LIST OF ABBREVIATIONS

AC	Alternating current
BF	Bonferroni
CCD	Charged coupled device
CLAHE	Contrast limited adaptive histogram equalization
DC	Direct current
DNI	Diffuse and nonlinear imaging
DOSI	Diffuse optical spectroscopic imaging
Hb	Hemoglobin
LED	Light-emitting diode
LUT	Look-up table
MC	Monte Carlo
MPM	Multiphoton microscopy
NIR	Near-infrared
PBS	Phosphate buffered saline
Ph.D.	Doctor of Philosophy
PMT	Photomultiplier tube
Rd	Diffuse reflectance
SD	Standard deviation
SFDI	Spatial frequency domain imaging
SHG	Second harmonic generation
StO_2	Tissue oxygen saturation
TCH	Tukey-Ciminera-Heyse
TPEF	Two-photon excited fluorescence

Chapter 1: Introduction

1.1 Motivation

In the last two decades, diffuse optical imaging (DOI) techniques have received significant interest as emerging non-invasive functional imaging tools for monitoring patient response to cancer therapies in the clinic. DOI techniques are able to provide important metabolic and hemodynamic information related to the in vivo tumor state[1,2]. In particular, a growing number of reports have successfully used DOI to monitor treatment response in cancer patients, with early hemodynamic and metabolic response markers reported within hours to weeks from the start of treatment[3–5]. For example, several reports have shown that decreases in hemoglobin content, decreases in water, and/or increases in lipid correlate with pathologic complete response in breast cancer patients receiving chemotherapy before surgery (i.e., neoadjuvant chemotherapy, NAC)[6–9]. Similarly, it has been reported that rapid increases in oxygenated hemoglobin within the first day of therapy is predictive of NAC outcomes[10]. While these results are encouraging, the potential impact, and ultimately adoption of DOI for cancer therapy monitoring in the clinic is limited in part by the lack of knowledge of the cellular, molecular, and biological origins of these clinical observations. Knowing how these macro DOI signatures relate to the biological underpinnings at the micro scale is key to providing clinically relevant insights that can be used to manage a cancer patient's treatment strategy with DOI feedback. Moreover, with a clear understanding of the relationships between DOI and the underlying tumor biology, it may be possible to use DOI for personalized and precision medicine to significantly impact and inform adaptive therapy strategies tailored to the in vivo state of each patient’s tumor.

1.2 Hypothesis

We hypothesized that: (1) clinically translatable DOI metrics measured at the tissue level could be tracked together with biological features at the cellular level in preclinical cancer models through the novel combination of DOI with intravital microscopy, and (2) this novel imaging method could enable the ability to investigate how these multiscale parameters relate to one another over space and time within individual preclinical tumors.

1.3 Aims

To test this hypothesis, three aims were set up with the primary objectives of first assessing the feasibility of the combined imaging method, constructing a fully integrated imaging system, and demonstrating that the integrated imaging modality can be used to track in vivo multiscale parameters and their potential relationships over space and time. The specific aim are:

Aim 1: To evaluate feasibility of combing DOI with intravital microscopy for in vivo monitoring of multiscale parameters in preclinical tumors.

Aim 2: To design, construct, and characterize the performance of a system that physically integrates DOI with intravital microscopy.

Aim 3: To demonstrate that the novel imaging method and system is able to track multiscale parameters and investigate multiscale relationships in vivo over space and time, all within a single tumor.

1.4 Structure of thesis

The thesis consists of 5 chapters. Chapter 1 provides the motivation behind this work by identifying the need to relate macroscopic DOI measurements to the underlying microscopic tumor biology to create a path towards DOI-guided adaptive therapy strategies to improve the efficacy of cancer therapies. Chapter 2 provides background on: (i) the current state of monitoring treatment response in breast cancer patients; (ii) Diffuse Optical Imaging (DOI) and its potential for monitoring treatment response; (iii) attempts made to correlate DOI metrics with histology to better understand the biological underpinnings of DOI treatment response monitoring; (iv) the role of intravital microscopy in elucidating biological makers of treatment response in preclinical tumor models; (v) the use of Spatial Frequency Domain Imaging (SFDI) as a non-contact , wide-field, label-free DOI technique for monitoring treatment response in preclinical tumors; (vi) intravital Multiphoton Microscopy (MPM) as the technique to combine with SFDI to investigate the relationships between DOI and the underlying tumor biology in concert; (vii) previous efforts to combine SFDI and MPM for multiscale imaging in non-tumor tissue types; and (viii) multiscale imaging of tumor vascular structure and function to lay the foundation for the novel imaging method and modality developed herein.

Chapters 3 and 4 together make up the aforementioned aims. Chapter 3 investigates the feasibility of combing SFDI with MPM for in vivo monitoring of multiscale vascular parameters in preclinical tumors through the developments of novel methods to coregister and depth match SFDI and MPM, followed by an in vivo study in a murine mammary tumor model. Chapter 4 details the development of a fully integrated SFDI-MPM system,

and our ability to use the integrated modality to conduct longitudinal and multiscale in vivo measurements of tumor vascular structure and function over a wide-field during the course of treatment in a breast cancer xenograft model to investigate multiscale relationships over space and time within a single tumor. Finally, Chapter 5 presents final conclusions and future directions for the method and system developed here, which include (i) exploring and validating novel drug combinations and scheduling, (ii) identifying translational imaging metrics of response and resistance, and (iii) creating a path toward diffuse optical image-guided adaptive therapy to improve the efficacy of cancer therapies.

Chapter 2: Background

2.1 Treatment response in breast cancer

Breast cancer is the most common type of cancer and is the second leading cause of cancer death in women in the U.S.[11] In 2019, an estimated 268,000 new cases of female breast cancer will be diagnosed in the U.S. (a 30% increase from 2014), and anticipated to account for 41,000 deaths[12]. Breast cancer deaths are typically a result of the eventual onset of therapy evasion/resistance, followed by metastasis. This is known to occur in the metastatic setting for a variety of anti-cancer agents, including drugs designed to target and kill breast cancer cells, such as trastuzumab (Herceptin®) for HER2 positive breast cancers[13]. Systemic therapies, including cytotoxic, hormonal, and immunotherapeutic agents, are initially active in approximately 90% of primary breast cancers and 50% of metastases[14]. Unfortunately many patients' tumors will eventually acquire therapy resistance with continued treatment due to the onset of resistance mechanisms such as increased expression of multidrug resistance (MDR) proteins (e.g. drug efflux pumps), mutated drug targets, and upregulation of alternate pathways[14]. These classes of resistance mechanisms can be broadly categorized as intrinsic resistance mechanisms, or resistance mechanisms operating intracellularly at the individual tumor cell level. The other class of resistance mechanisms are extrinsic resistance mechanisms, or extracellular mechanisms which are a result of changes to heterogeneities in the tumor microenvironment. Examples of extrinsic resistance mechanisms include those related to the various tumor-stroma interactions, such as the interactions between tumor cells and immune cells, and tumor cells and fibroblasts[15,16].

A potential strategy for avoiding tumor evasion/resistance to therapies in breast cancer would be to progressively alter the treatment regimen in a patient specific manner. Effective guiding and scheduling of personalized therapy will require longitudinal and frequent in vivo monitoring of functional information related to the tumor state. This is imperative for predicting treatment response to guide adaptive therapy decisions, including when to continue or when to stop and alter treatment. However, anticipating treatment response is a significant clinical challenge because current clinical imaging modalities (e.g. MRI, CT, PET-CT) are highly focused on anatomical structures rather than metabolic or molecular information, and the cost and safety concerns associated with current medical imaging techniques limit how often patients can be imaged during therapy. Notably the changes in commonly monitored parameters, including tumor volume or glucose-analog uptake, have been shown to be poor predictors of treatment response and often manifest only after a tumor has stop responding to therapy[17,18]. The ability to accurately predict treatment response would allow clinicians to make evidence-based therapy changes in a timely manner, which could substantially improve patient outcomes.

2.2 Diffuse Optical Imaging (DOI) for in vivo monitoring of treatment response

Diffuse Optical Imaging (DOI) techniques are ideally suited for monitoring treatment response as they provide endogenous label-free hemodynamic and metabolic tissue-level information of the in vivo tumor state[1,2], and have demonstrated clinical utility for continuous monitoring of early treatment response and frequent longitudinal monitoring of treatment efficacy[3–9]. Moreover, they have favorable safety profiles, are relatively inexpensive, and do not require dedicated infrastructure[1,2].

DOI methods, such as Diffuse Optical Spectroscopy (DOS), non-invasively launch near-infrared (NIR) light (650-1000 nm) into deep (mm to cm thick) biological tissue to quantify wavelength-dependent tissue optical properties (OPs), namely absorption $\mu_a(\lambda)$, and reduced scattering $\mu'_s(\lambda)$. NIR light in human tissue experiences minimal absorption, and thus penetrates on the order of several millimeters to several centimeters deep into tissue[2]. In heterogeneous tissue, such as tumors, photons are multiply scattered at distances greater than 1 to 2 mm from a source, and can be modeled as a photon diffusion process using the Radiative Transport Equation (RTE)[1,19]. Although the RTE model of diffuse light transport in tissue accounts for both the absorption and scattering of photons, it is difficult to solve analytically and is typically simulated using Monte Carlo (MC). An approximated diffusion equation is often used in practice to easily and analytically solve for μ_a and μ'_s based on measurement and boundary conditions, and the use of time/spatial domain versus frequency domain, laying the foundation for various DOI methods[1,2]. Measurements of μ_a at multiple wavelengths allows for the extraction of tissue hemodynamic parameters, including absolute concentrations of oxyhemoglobin (HbO_2) and deoxyhemoglobin (HHb), from which total hemoglobin (THb) concentration and tissue oxygen saturation (StO_2) can be determined[1]. μ'_s is related to and dictated by tissue structure such as the extracellular matrix, as well as density of cells and organelles[2]. Figure 2-1 provides examples of DOI methods and their applications in cancer.

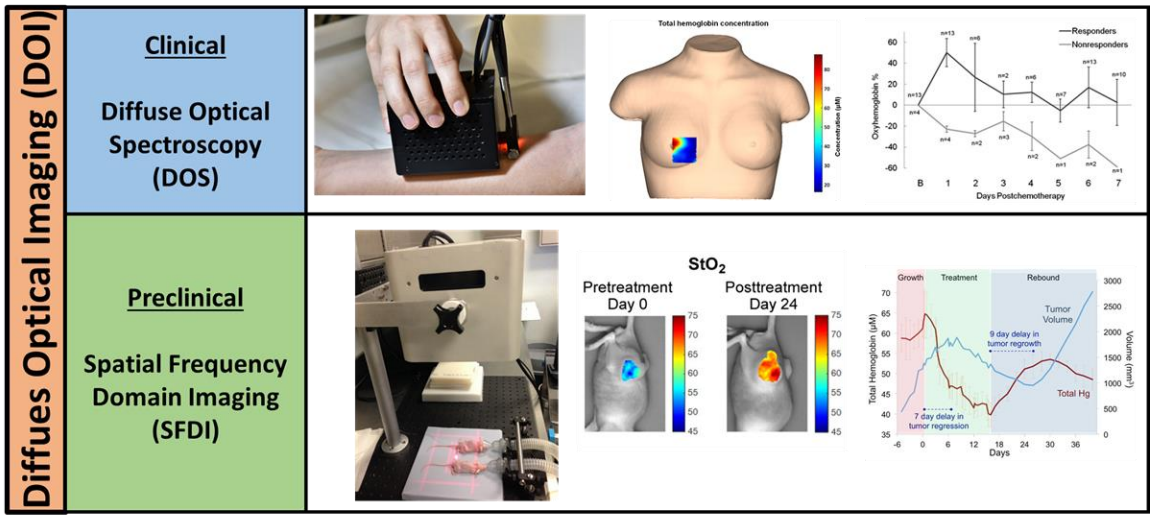

Figure 2-1: Examples of Diffuse Optical Imaging (DOI) technologies for treatment response monitoring in clinical and preclinical tumors[10,20,21].

DOI techniques have been used to monitor and predict treatment response on the macro to mesoscopic scales in the preclinical and clinical settings. For example, Roblyer et al. showed that a clinical frequency-domain DOS system can inform pathologic complete response (pCR) in breast cancer patients 1 day after their first chemotherapy infusion based on percent changes in HbO_2[10]. Moreover, Tabassum et al. demonstrated the feasibility of a wide-field, non-contact preclinical DOI technique called Spatial Frequency Domain Imaging (SFDI) to optically characterize a preclinical prostate cancer model[21]. Initial findings showed that μ'_s and StO_2 are predictive of tumor rebound several days prior to uncontrolled exponential tumor growth. These and other published work demonstrate that DOI is sensitive to treatment response with clinical potential based on functional and metabolic measurements made at the tissue-level. However, for clinicians to make informed decisions on a cancer patient's treatment strategy using DOI feedback, it will be imperative for them to know how any changes (or lack of changes) they observe with DOI are ultimately indicative of the underlying biological mechanisms taking place within the patient's tumor. Although efforts have been made to bridge this gap and provide a biological basis for DOI measurements in tumors, these multiscale relationships between DOI metrics and the biological underpinnings remain to be elusive. This is in part due to a lack of appropriate tools/methods available to investigate potential multiscale relationships between DOI and the underlying tumor biology with high fidelity so as to ensure clear and accurate biological interpretations of DOI measurements in tumors.

2.3 Correlating DOI with histology

In the last two decades, several reports have tried to link DOI with histology in an attempt to establish robust correlations between key DOI and underlying biologic measures of tumors[9,22–26]. However, there are several limitations with this approach.

One limitation is being able to achieve high coregistration accuracy between DOI and histology[26]. This is usually a difficult and cumbersome manual task to extract tissue samples for histology that precisely match where imaging took place inside the live intact tissue to correlate molecular metrics with imaging metrics, leaving room for doubt and error in those correlations. Furthermore, while DOI generally measures volume-averaged tissue, histology typically looks at single slice from a single tumor location and therefore only captures a small fraction of the tumor volume and does not adequately capture heterogeneities sampled with DOI[26].

Another limitation is that there may be important microscale markers of treatment response to correlate with DOI that are difficult to capture and quantify through histology. For example, tumor microvascular metrics such as tortuosity, vessel length, and vascular permeability are difficult to assess and measure with conventional immunohistochemistry (IHC)[27,28], but could be invaluable microscale indicators of treatment response, such as in the context of antiangiogenic therapies[29]. Moreover, the tissue fixation and processing steps of IHC can introduce artifacts and disrupt the native architecture of the various micro-morphologies in the tumor such as the microvascular network, and therefore may result in estimation errors of these markers from histology[27].

Finally, being able to investigate and verify the potential correlations between the temporal changes in DOI and underlying biologic parameters in response to therapy is imperative to clearly establish the accuracy with which DOI can track treatment response. The relevant timescales for identifying key biological markers of treatment response during therapy can be within the first 24 to 48 hours of the first treatment, to multiple consecutive days following the start of treatment. However, taking many tissue samples for histology within the first 24 to 48 hours, followed by multiple consecutive days is impractical for both the clinical and preclinical settings. Although one may anticipate how biological parameters may change during treatment, it is less clear when these key changes are expected to take place over the course of treatment. Thus, it is difficult to know when to take tissue samples for IHC analysis of key time-points for comparison with imaging.

Ultimately, to link key DOI and underlying biologic measures of tumors in a reliable manner, the ideal method would need to accomplish the following: (i) enable superior interrogation of the same intact and sampled in vivo tissue volumes between DOI and biological metrics via accurate and precise coregistration, and (ii) accurately capture relevant in vivo biological markers of treatment response in a noninvasive manner for correlative analysis with DOI measurements taken at the same time and over multiple time-points within a single tumor. The preclinical setting is ideal for testing these ideas as this will require careful control over treatments and imaging, with regular access to tumors. Notably, it will be important to measure the same parameters as clinical DOI techniques to translate potential findings to the clinic and provide a pathway for adaptive therapy strategies based on diffuse optical monitoring of treatment response.

2.4 Imaging biological markers of treatment response in preclinical tumors with intravital microscopy

Intravital microscopy has played a key role in longitudinally characterizing in vivo biological markers of treatment response in the preclinical setting. For instance, intravital microscopy techniques have enabled the visualization and study of in vivo structural and functional changes to the tumor microvasculature, and as a result have transformed our understanding of angiogenesis and treatment effects related to the tumor microvasculature. For example, using intravital fluorescence microscopy, Yuan et al. revealed that tumor vascular permeability is spatially heterogeneous due to the formation of abnormal microvascular architecture during angiogenesis[30].

More recently, intravital microscopy techniques have been used to investigate the role of the tumor microvasculature during response and resistance, and how the tumor microvasculature can even differ between responsive and resistant tumors. For example, Nakasone et al. showed through in vivo spinning disk confocal microscopy that extrinsic factors in mammary tumors, such as vascular leakage, impact drug distribution and the inflammatory response which can influence tumor resistance[15]. Notably, McCormack et al. demonstrated through hyperspectral intravital microscopy that tumor microvessel density and oxygenation can track differential treatment responses in trastuzumab-sensitive and –resistant tumors[31]. Specifically, in comparison to the trastuzumab-resistant tumors, the authors observed in the trastuzumab-sensitive tumors significant increases and decreases in microvessel density and oxygenation, respectively, five days into trastuzumab therapy. Moreover, this observation was followed by significant decreases and increases in the

tumor volumes of trastuzumab-sensitive and –resistant tumors, respectively, 48 hours later. Using hyperspectral intravital microscopy, this study revealed the potential prognostic value of in vivo tumor microvasculature dynamics differentiating response from resistance during therapy. However, these and other similar intravital microscopy techniques are limited to superficial imaging (<150 μm deep) in tumors due to the use of visible wavelengths (350-750 nm) for single photon imaging, which experience high amounts of absorption (e.g., due to blood in superficial tumor vasculature) and scattering that limit their imaging depth in biological tissue.

Conversely, intravital multiphoton microscopy (MPM) uses longer wavelengths in the NIR to short-wave infrared (SWIR, 1000-1300 nm) regions for two (or more) photon imaging, which experience significantly less absorption and scattering and can therefore image deeper into biological tissue (~ 1 mm). Given this and other advantages of intravital MPM over other intravital microscopy techniques (see Section 2.6 for details), MPM has revolutionized in vivo imaging of preclinical tumors by providing exquisite molecular, cellular, and physiological information and key insights into tumor pathophysiology that ultimately influenced new drug targets and strategies for treating tumors[32]. The various MPM contrasts mechanisms that have been exploited for tumor imaging in the preclinical setting include two-photon excitation (TPE), second harmonic generation (SHG), and fluorescence lifetime imaging microscopy (FLIM)[33,34]. For example, through TPE of fluorescently labeled cells, Wyckoff et al. were able to directly visualize macrophage-assisted tumor cell migration and intravasation mediated by paracrine signaling between tumor cells and tumor-associated macrophages in mammary tumors[35,36]. Szulczewski et al.

were able to track heterogeneity in breast tumor cells and the surrounding microenvironment in a live mouse model using TPE and FLIM to excite and monitor the endogenous fluorescence of the metabolic co-factors NADH and FAD in tumor cells, along with SHG to see collagen[37]. Shah et al. demonstrated that metabolic subpopulations within tumors measured with TPE and FLIM imaging of NADH and FAD provide metrics predictive of treatment response and resistance in animal models[38]. Finally, building upon the single photon intravital microscopy work with the tumor microvasculature, MPM has made it possible to characterize with exquisite detail both structural and functional changes in the tumor microvasculature across space and time during tumor development and during the course of treatment[32]. For example, Tong et al. characterized vascular normalization upon the administration of an antiangiogenic agent using intravital MPM, noting decreases in vascular density, vessel diameter, tortuosity, and vascular permeability[29]. The authors also found an induced pressure gradient across the tumor vasculature, along with increases in drug penetration as a result of vascular normalization[29]. Such observations of the tumor microvasculature have led to important insights with regard to the dosing and scheduling of different therapy regimens.

However, it is worth noting that treatment response studies using intravital microscopy have mainly emphasized fundamental cancer biology, and thus highly focused on the microscale without a direct means for clinical translation. Moreover, clinical translation of these biological mechanisms for effective monitoring of treatment response is challenging in part due to sampling of small regions within a tumor that do not fully recapitulate the global response state as a function of the entire spatial heterogeneity

throughout the tumor. Nonetheless, intravital microscopy techniques such as MPM for deep, high resolution, 3D in vivo imaging of tumors, have the potential for elucidating biological markers of treatment response at the microscale based on changes to the underlying tumor biology as a function of different therapy regimens. Accordingly, with careful attention to proper integration and systematic characterization, the combination of intravital microscopy with DOI could be the ideal method to track together clinically translatable DOI metrics measured at the tissue level with biological features captured at the cellular level with intravital microscopy, all within a single tumor in the preclinical setting. Furthermore, such a multiscale imaging approach could provide the opportunity to bridge biological mechanisms with clinical outcomes, and as a result enable for the first time direct information flow between cancer biology and clinical oncology.

2.5 In vivo diffuse optical monitoring of preclinical tumors with Spatial Frequency Domain Imaging (SFDI)

Spatial Frequency Domain Imaging (SFDI) is a DOI technique that can quantify volume-averaged tissue optical absorption and scattering on a pixel by pixel basis over a two-dimensional area[39,40]. Measurements of tissue optical absorption at different wavelengths enables the extraction of molar concentrations of tissue chromophores over a wide-field, providing a non-contact and label-free means to assess tissue viability, oxygenation, micro-architecture, and molecular content[1]. Details regarding the theory, instrumentation, image acquisition, and data processing for SFDI have been described elsewhere[39–42]. Figure 2-2 provides a diagram of a typical SFDI setup and imaging geometry, and data processing workflow.

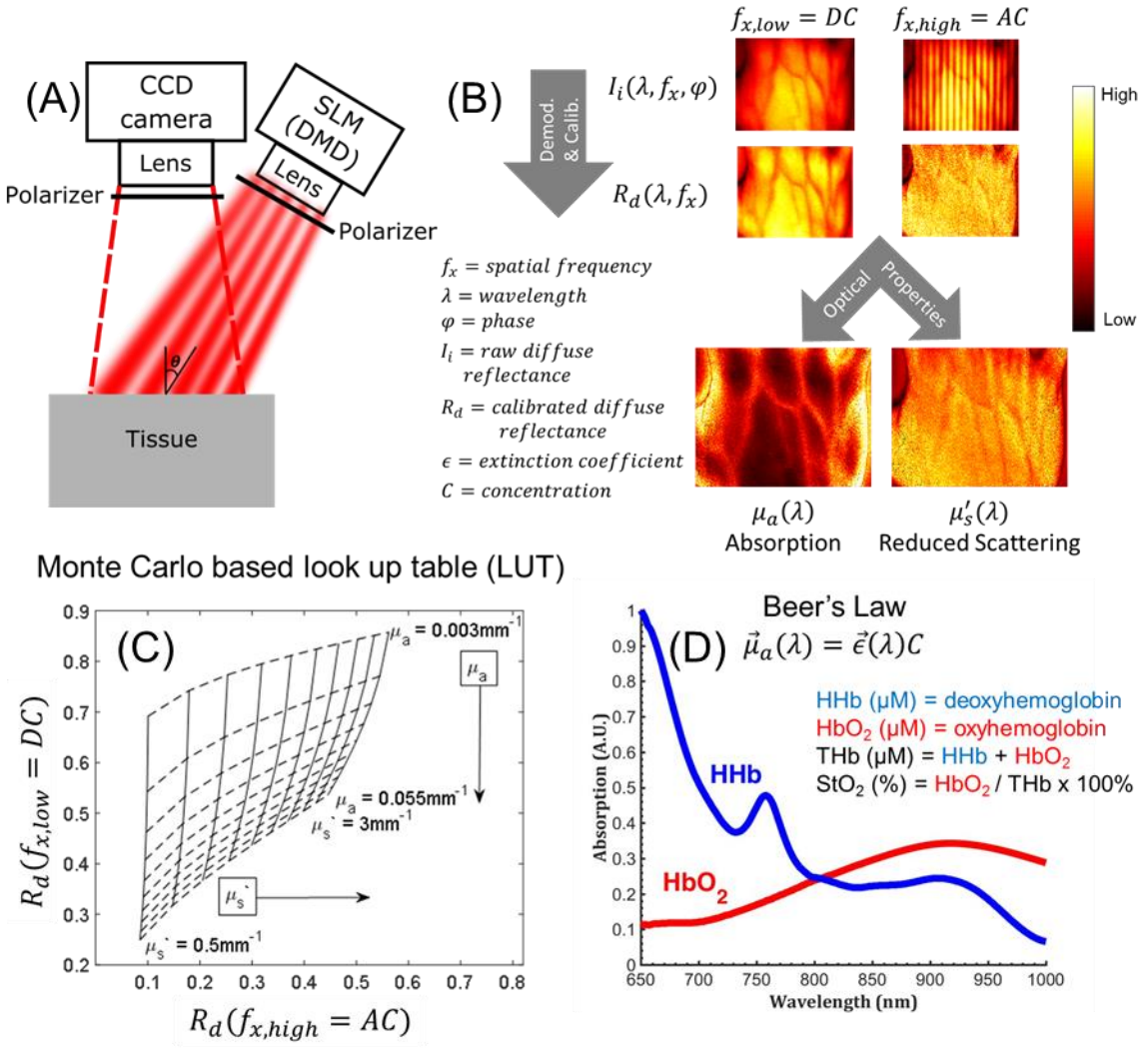

Figure 2-2: Spatial Frequency Domain Imaging (SFDI) (A) setup and imaging geometry (θ ~15 deg), and (B-D) data processing workflow[21].

Briefly, SFDI is a noncontact, wide-field imaging system that projects spatially modulated sinusoidal patterns of light at different wavelengths and spatial frequencies onto diffusive media to separate the relative contributions of reduced scattering $\mu'_s(\lambda)$ and absorption $\mu_a(\lambda)$ within the sample of interest. At each wavelength and spatial frequency (in this case along one spatial dimension, f_x), raw reflectance images at three different phases (0°, 120°, and 240°) are sequentially projected using a digital micro-mirror device (DMD) or other spatial light modulator (SLM) and measured with a camera[43].

The planar (DC) and sinusoidal (AC) projections are measured and then demodulated to extract the amplitude envelope ($M_{AC}(f_x)$) of the measurement using a conventional communications algorithm[40]. A separate reference measurement ($M_{AC,ref}(f_x)$) at the same wavelengths and spatial frequencies is made on a calibration phantom with known optical properties to calibrate for the source intensity and the instrument response of the imaging system. Additionally, a Monte Carlo (MC) based or analytical forward model of photon propagation in diffusive media is used to predict the calibration phantom's diffuse reflectance ($R_{d,ref}(f_x)$) based on prior knowledge of the calibration phantom's optical properties at each measurement wavelength[40]. Using Equation 2.1 the amplitude envelopes of the sample ($M_{AC}(f_x)$) and calibration phantom ($M_{AC,ref}(f_x)$), in addition to the predicted diffuse reflectance of the calibration phantom ($R_{d,ref}(f_x)$), are used to determine the calibrated diffuse reflectance of the sample ($R_d(f_x)$) with unknown optical properties for each wavelength and spatial frequency.

$$R_d(f_x) = \frac{M_{AC}(f_x)}{M_{AC,ref}(f_x)} R_{d,ref}(f_x) \tag{2.1}$$

The calibrated diffuse reflectance of the sample (i.e., the modulation transfer function (MTF) of the turbid sample as a function of spatial frequency) serves as an input to an inverse model, in this case a MC-based two-f_x look-up-table (LUT) method, to extract the optical property values ($\mu_a(\lambda)$ and $\mu'_s(\lambda)$) of the sample of interest on a pixel-by-pixel basis at each measurement wavelength. The LUTs can be generated by running MC simulations, and/or by scaling a single MC simulation[44,45]. Finally, the absolute concentrations of tissue-dominant absorbing chromophores, such as HbO_2 (μM) and HHb (μM), are calculated from their known extinction coefficients and the extracted $\mu_a(\lambda)$ values from each wavelength by performing a least-squares fit with the Beer's Law (see Equation 3.1)[46]. From HbO_2 and HHb, total hemoglobin (THb (μM) = HbO_2 + HHb) and tissue oxygen saturation (StO_2 (%) = 100 × HbO_2 / THb) can be calculated.

The ability of SFDI to provide quantitative functional and molecular information in tissue, combined with its relative simplicity, safety, and low-cost has led to its use for a variety of biomedical applications. Some examples include SFDI monitoring of reconstructive surgery, burn wound healing, vascular occlusion, vascular impairment during the progression of Alzheimer's disease, and drug delivery to brain tissue[47–52]. Less explored with SFDI are applications in tumor monitoring. The few examples include evaluation of non-melanoma skin cancer for optimizing photodynamic therapy (PDT), monitoring of doxorubicin (DOX) release, characterization of resected tumor specimens for heterogeneity in tissue structure for breast conserving surgery, guided resection of gliomas, and monitoring of palpable breast lesions[53–60]. Recently, our group is working on demonstrating for the first time that SFDI can be used to longitudinally monitor therapy

response in a preclinical prostate cancer model, and have shown that SFDI can predict tumor rebound[21]. However, the links between biological phenomena at the cellular level and SFDI metrics at the tissue level have yet to be demonstrated during treatment response, although efforts in our group are ongoing to compare SFDI and ex vivo tissue parameters over the course of treatment. Nonetheless, SFDI monitoring of cancer therapies can provide key insights into treatment response in the preclinical setting. Notably, SFDI measures the same parameters as clinical DOI systems such as DOS, and therefore provides a pathway to the clinic for adaptive therapy strategies based on diffuse optical monitoring of treatment response. In light of all of this, we have reason to believe that SFDI is the appropriate DOI technology to investigate the biological origins of treatment-induced changes observed with DOI in the preclinical setting.

2.6 Intravital Multiphoton Microscopy (MPM)

Given its precedence in identifying in vivo biological makers of treatment response in preclinical tumors (see Section 2.4) and its ability to do so relatively deeply into tissue ($\leq$ 1 mm), intravital MPM could be an excellent candidate modality to combine with SFDI and explore the biological underpinnings of key DOI markers. To successfully integrate both imaging modalities and their respective datasets, it is imperative to understand their respective underlying theories and practical implementations. Here we provide the relevant theory and practical aspects of intravital MPM.

Firstly, the important advantages of MPM over other intravital microscopy techniques include: (i) higher resolution and rejection of out-of-focus background, (ii) deep tissue imaging (~1 mm), (iii) the ability to capture fast dynamics, (iv) intrinsic 3D imaging,

and importantly (v) having access to a range of contrast mechanisms[33]. The higher resolution, rejection of out-of-focus background, and 3D imaging are due to two or more photons needed to generate nonlinear processes, of which the two main ones are multiphoton excitation and harmonic generation. The probability of a nonlinear process generated from two or more photons interacting simultaneously with a molecule are extremely low, but is increased with the use of a pulsed laser and goes as the average incident laser intensity raised to the order of the nonlinear process[33]. Thus, such processes mainly take place at the focal plane where most of the average incident laser intensity is concentrated, and very little outside the focal plane where the probability drops off rapidly. This not only minimizes out-of-focus background and photo-damage to the sample, but also provides superior spatial resolution and intrinsic optical sectioning, enabling 3D resolution imaging (Figure 3 and Eq. (3))[33]. Figure 2-3a and 2-3b provide visual demonstrations of one- and two-photon excitation in a fluorescent medium, and Equation 2.2 (from thorlabs.com) provides an analytical expression for the theoretical lateral resolution of MPM for microscope objectives with numerical apertures (NA) greater than 0.7, which are typically used for intravital MPM.

$$MPM\ lateral\ resolution = \frac{0.383\lambda_{ex}}{(NA)^{0.91}}\ , where\ NA > 0.7 \qquad (2.2)$$

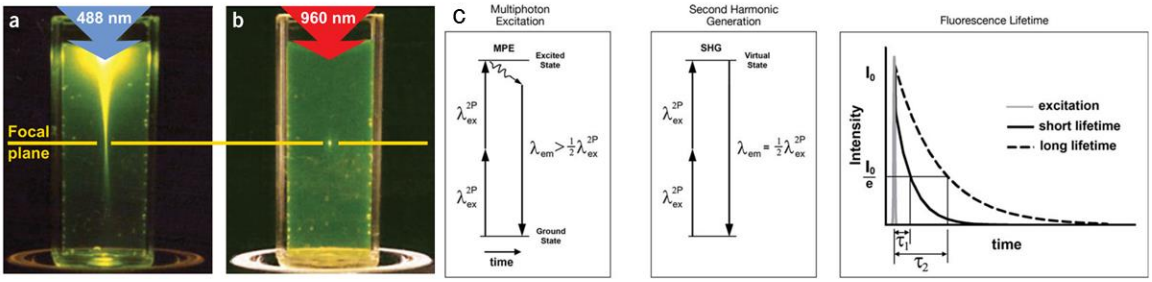

Figure 2-3: Demonstration of (a) single-photon versus (b) two-photon excited fluorescence[33]. (c) Various nonlinear multiphoton modes of contrast/imaging[34].

The ability to image deep into tissue is a result of using longer wavelengths in the NIR to short-wave infrared (SWIR) regions (700-1300 nm) as opposed to traditional one-photon imaging at UV and visible wavelengths (300-750 nm). Individual photons at longer wavelengths have less energy than single photons at shorter wavelengths, but the simultaneous interaction of two or more lower-energy photons with a molecule provides the same effective energy as a high-energy single photon needed for processes such as excited fluorescence[33]. Moreover, the NIR and SWIR wavelengths incur less absorption and scattering compared to UV and visible wavelengths in biological tissue, and thus penetrate deeper.

However, one barrier to deep multiphoton imaging in preclinical tumors in vivo is the skin, as it is highly attenuating due to mostly scattering. This has been overcome by employing techniques that provide direct access to the tumor mass for imaging, such as skin-flaps and window chambers[32,61,62]. Such techniques vary with regard to how often and long a single tumor can be imaged based on the nature of the technique[63]. It is also worth noting that there is concern that techniques for direct visualization of tumors, such as skin-flaps and window chambers, potentially disrupt the native tumor behavior. Nonetheless, the techniques for direct intravital imaging of tumors have proved useful in helping to elucidate underlying mechanisms related to the hallmarks of cancer, and are employed in Chapters 3 and 4 of this thesis.

2.7 Multiscale imaging with SFDI and MPM

The concept of multiscale imaging with SFDI and MPM has been briefly explored before, but never for applications in oncology and never done in a fully integrated and

coregistered fashion. For example, Balu et al. demonstrated during an arterial occlusion that changes in wide-field hemodynamics measured with SFDI strongly correlate with changes in NADH auto-fluorescence of cells measured with MPM near the basal layer of human skin, and found that no such correlations were observed in the epidermal layers near the surface of the skin[64]. Additionally, Saager et al. showed that independent measurements of melanin volume fraction and distribution thickness by SFDI and MPM across various human skin types were strongly correlated[65]. Although these studies did not investigate spatial heterogeneity in multiscale relationships by exploring how microscale phenomena are spatially correlated throughout the tissue-level scale, they strongly suggest that there is much to be gained from exploring multiscale relationships to generate a holistic picture of underlying biological and physiological mechanisms. A fully coregistered SFDI and MPM imaging system will enable the study of complementary tumor metrics across multiple imaging length scales (e.g., micro-vessel structure and tissue-level hemodynamics) and allow for a deeper investigation into the multiscale relationships to ultimately understand how microscale treatment-induced changes manifest in tumor functional and metabolic changes at the tissue-level. Such knowledge will lay the foundation for identifying translational imaging metrics of treatment response, and create a path towards diffuse optical image-guided adaptive therapy for long term tumor control.

2.8 Multiscale imaging of tumor vascular structure and function

It is becoming increasingly evident that heterogeneities in the tumor microenvironment, in particular spatial variations in the tumor vascular network, can play a major role in treatment response. The variability in vessel structure and function

throughout the tumor can enhance sensitivity to therapy in some tumor regions and exacerbate resistance in other tumor regions. For example, areas within a tumor that have highly tortuous and poorly perfused vasculature can experience impaired delivery of systemic agents, allowing tumor cells in those areas to grow unchallenged[32]. Conversely, tumor regions with well-ordered and highly perfused vessels will experience effective drug delivery to tumor cells to mitigate growth and proliferation in those regions[66]. Studies have also observed ischemic and hypoxic tumor regions preceding elevated angiogenesis and tumor progression[67]. Ischemia and hypoxia can arise from tumor regions that have outgrown their vascular supply network[68,69]. Furthermore, hypoxia has been linked to cultivating resilient and aggressive phenotypes, as well as evasion of therapy[70–72]. All of this suggests that monitoring tumor vascular structure and function can provide key insights into treatment response. Importantly, this thesis will demonstrate that the combination of SFDI and MPM can be used to investigate potential multiscale relationships between DOI and the underlying tumor biology through multiscale imaging of tumor vascular structure and function, therefore establishing a method/tool to explore the biological underpinnings of DOI measurements in tumors.

Chapter 3: Diffuse and nonlinear imaging of multiscale vascular parameters for in vivo monitoring of preclinical mammary tumors

Diffuse optical imaging (DOI) techniques provide a wide-field or macro assessment of the functional tumor state and have shown substantial promise for monitoring treatment efficacy in cancer. Conversely, intravital microscopy provides a high-resolution view of the tumor state and has played a key role in characterizing treatment response in the preclinical setting. There has been little prior work in investigating how the macro and micro spatial scales can be combined to develop a more comprehensive and translational view of treatment response. To address this, a new multiscale preclinical imaging technique called diffuse and nonlinear imaging (DNI) was developed. DNI combines multiphoton microscopy with spatial frequency domain imaging (SFDI) to provide multiscale data sets of tumor microvascular architecture coregistered within wide-field hemodynamic maps. A novel method was developed to match the imaging depths of both modalities by utilizing informed SFDI spatial frequency selection. An in vivo DNI study of murine mammary tumors revealed multiscale relationships between tumor oxygen saturation and microvessel diameter, and tumor oxygen saturation and microvessel length ($|\text{Pearson's } \rho| \geq 0.5$, $P < 0.05$). Going forward, DNI will be uniquely enabling for the investigation of multiscale relationships in tumors during treatment.

The work in Chapter 3 is published in the Journal of Biophotonics[73] with the following contributing authors:

Kavon Karrobi,[a] Anup Tank,[a] Syeda Tabassum,[b] Vivian Pera,[a] and Darren Roblyer[a]

[a] Department of Biomedical Engineering, Boston University, Boston, Massachusetts, United States

[b] Department of Electrical and Computer Engineering, Boston University, Boston, Massachusetts, United States

3.1 Introduction

Diffuse optical imaging (DOI) is a non-invasive and label-free technique that uses near-infrared light (650-1000 nm) to characterize biological tissue. DOI techniques typically provide multi-wavelength estimates of tissue optical absorption (μ_a) and reduced scattering (μ'_s), which can be used to define diagnostic or prognostic thresholds for a wide range of conditions and pathologies[1,2]. Optical absorption can be used to extract concentrations of oxyhemoglobin (HbO_2) and deoxyhemoglobin (HHb), from which total hemoglobin (THb) and tissue oxygen saturation (StO_2) can be determined[1]. Optical scattering is related to tissue microstructure and can provide information about the extracellular matrix, density of cells and relative dimensions of organelles[2]. DOI has been highly used to characterize the in vivo tumor state in both the preclinical and clinical settings[10,21,74]. There is a growing number of reports in which DOI technologies have been successfully used to monitor treatment response in cancer patients, with early response markers reported within hours to weeks from the start of treatment[4,5,10,75–77]. While these results are encouraging, DOI techniques are limited in that they provide only a wide-field or macro view of the tumor state and lack the spatial resolution needed to visualize how

micro-scale features, including microvascular architecture, contribute to the tumor state. Nonetheless, knowing how these macro DOI signatures relate to the tumor biology at the micro-scale is key to providing clinically relevant insights that can be used to manage a patient's treatment strategy. Several prior studies have attempted to correlate DOI metrics with histopathology to better characterize the biological underpinnings of key imaging markers[22–26]. However, coregistration between noninvasive DOI and ex vivo tissue is challenging and can only characterize tissue at a single point in time, limiting the ability to understand and monitor the dynamic in vivo tumor state.

Conversely, intravital microscopy provides a high-resolution view of the tumor state and has played a key role in characterizing treatment response in the preclinical setting[32,34]. In particular, changes to the tumor microvasculature architecture have been studied extensively in the context of treatment response in small animal tumor models[29,30,78–81]. For example, Tong et al.[29] characterized vascular normalization upon the administration of an antiangiogenic agent using intravital multiphoton microscopy (MPM), noting decreased vascular density, vessel diameter, tortuosity and vascular permeability, along with increased drug penetration as a result of vascular normalization. These observations have led to important insights with regard to the dosing and scheduling of different therapy regimens[32,81]. Intravital MPM is limited, however, in that it can only image a small fraction of the tumor volume during a single measurement and may not adequately capture heterogeneities.

While both the macro and micro spatial scales have value for monitoring the in vivo tumor state, there has been little prior work in investigating how these spatial scales can be

combined to develop a more comprehensive and translational view of treatment response. In this work, we address this issue by combining wide-field DOI with intravital MPM to create a new multiscale preclinical imaging technique called diffuse and nonlinear imaging (DNI). DNI provides structure-function relationships by combining DOI measurements of tumor oxygenation over a wide-field (function) as well as coregistered MPM measurements of microvascular architecture (structure). DNI has key advantages over the commonly used technique of manually correlating imaging markers with ex vivo histology[22–26]. These include the intrinsic ability to coregister macro- and micro-scale parameters over a large field-of-view (FOV), thus capturing tumor heterogeneity while avoiding sampling bias[82]. In addition, to the best of our knowledge, several microvascular metrics including tortuosity, vessel length and vascular permeability cannot be quantified with standard ex vivo histopathology techniques[27]. Furthermore, the integration of these modalities potentially allows for longitudinal in vivo monitoring of these multiscale relationships over time, which may lead to a more comprehensive understanding of treatment response and resistance. Finally, since intravital imaging has long been used to characterize tumor microvasculature during angiogenesis, treatment and the development of resistance[15,29–31,83], DNI provides a means to place new findings within the context of this rich prior work.

In the following sections, we first describe the two techniques that combine to make DNI: spatial frequency domain imaging (SFDI) and MPM. We then present the methods used to compare the imaging depth of both modalities, and describe a novel method to match imaging depths by adjusting the choice of SFDI spatial frequency. We then

characterize the tradeoffs between depth matching and the ability to extract optical properties. We then describe the procedures developed to image tumors in a coregistered fashion. Finally, we describe the metrics extracted from each modality, and present suggestive novel multiscale correlations revealed with DNI during preclinical tumor imaging.

3.2 Methods

3.2.1 Spatial frequency domain imaging

All SFDI measurements were made with the OxImager RS SFDI system (Modulated Imaging Inc., Irvine, California). A diagram of the SFDI system is shown in Figure 3-1A. The SFDI system has nine LEDs from 471 to 851 nm for spatially modulated illumination and a charged-coupled device (CCD) camera (1392 × 1040 pixels) to measure the reflected light. The spatial patterns were projected over a 20 × 15 cm area at an incident angle of 15 degrees with respect to the surface normal (θ in Figure 3-1A) to reduce specular reflection. Crossed linear polarizers were used in front of the projection and detection lenses to further eliminate specular reflection. The measured reflectance was collected perpendicular to the sample surface, with an effective detection NA of 0.26 (Imaging lens: Xenoplan 1.9/35; Schneider Optics, Hauppauge, New York). The SFDI system was operated at a working distance of 32 cm, with a detection of FOV of 8.7 × 6.5 cm.

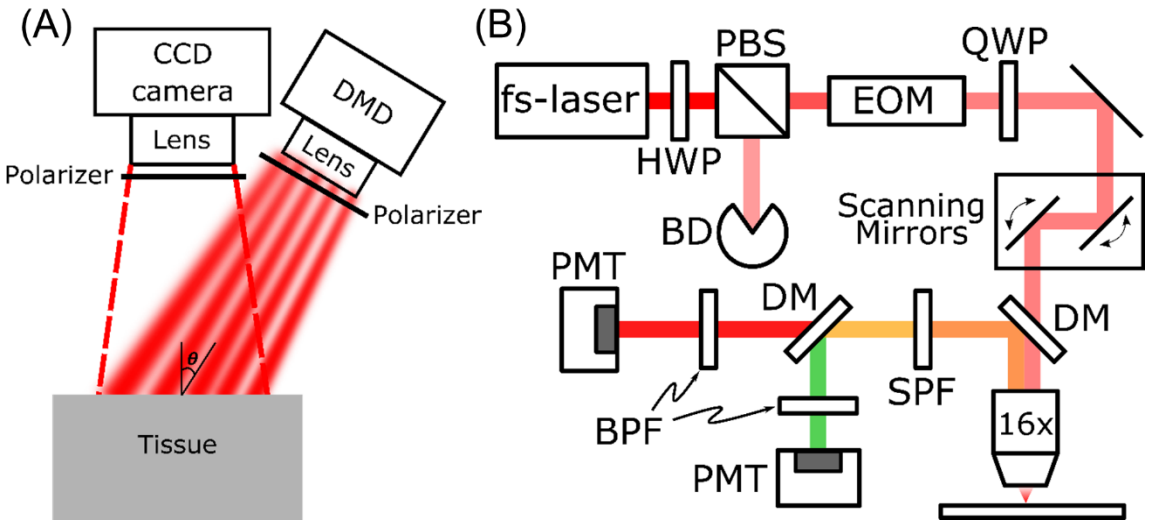

Figure 3-1: The diffuse and nonlinear imaging (DNI) system combines coregistered spatial frequency domain imaging (SFDI) and multiphoton microscopy (MPM). (A) A generalized schematic of the SFDI system. A digital micro-mirror device (DMD) was used to structure light from LEDs into sinusoidal 1-D patterns, which were projected onto a sample of interest. The reflected signal was collected with a CCD camera. (B) Schematic of the MPM system. Pulses of light from a femtosecond tunable laser (680-1300 nm) were passed through a half-wave plate (HWP) before being split by a polarizing beamsplitting (PBS) cube, which diverts approximately half of the laser power to a beam dump (BD). The remaining half was passed through an electro-optic modulator (EOM or Pockels cell) used to control the power of the excitation beam at the sample. The excitation and emission paths were coupled through a 16× long working distance (3 mm) water immersion objective (0.8 NA), and separated by a dichroic mirror (DM, 755 nm long-pass). A short-pass filter (SPF) in the detection path was used to further clean up the collected emission before splitting it into two channels with a dichroic mirror (DM, 565 nm long-pass). Band pass filters (BPF), 525/70 nm and 700/75 nm, were used to further isolate the emitted light. Each emission channel was collected with photomultiplier tubes (PMT). A quarter-wave plate (QWP) was placed in the excitation path to circularly polarize the light for second harmonic generation (SHG) imaging of collagen, which was not analyzed for the purposes detailed herein.

Optical properties and hemoglobin concentrations were determined on a pixel-by-pixel basis as described in detail elsewhere[21,40]. Briefly, the SFDI system was used to project one-dimensional sinusoidal spatial patterns at multiple wavelengths onto the sample of interest (e.g., phantom or tumor). For each spatial frequency (f_x), three different phase offsets were projected (0°, 120° and 240°). The acquired images were then demodulated to extract the amplitude envelope at each spatial frequency measurement using an established amplitude demodulation method[40]. The demodulated images were compared with equivalent measurements made on a calibration phantom with known optical properties to remove the instrument response and obtain the calibrated diffuse reflectance ($R_d(f_x)$) of the sample at each spatial frequency. All experimental and calibration measurements were performed at the same height/image plane to avoid the need for height correction during processing. Absorption ($\mu_a(\lambda)$) and reduced scattering ($\mu'_s(\lambda)$) were recovered using a two-f_x inversion algorithm which indexed a lookup table (LUT) relating Rd to optical properties for a given f_x pair. LUTs were generated from Monte Carlo (MC) simulation results as described elsewhere[84]. For in vivo measurements, HbO_2 (μM) and HHb concentrations (μM) were calculated by performing a least squares fit with Equation 3.1 using known extinction coefficients for HbO_2 and HHb, and measured μ_a values at [659, 691, 731, 851] nm:

$$\vec{\mu}_a(\lambda) = \vec{\varepsilon}_{HbO_2}(\lambda)C_{HbO_2} + \vec{\varepsilon}_{HHb}(\lambda)C_{HHb}. \quad (3.3)$$

Total hemoglobin (THb (μM) = HbO_2 + HHb) and tissue oxygen saturation (StO_2 (%) = 100 × HbO_2 / THb) were also determined. All SFDI processing was performed in MATLAB R2015a (MathWorks, Natick, Massachusetts).

3.2.2 Multiphoton microscopy

A schematic of the MPM system is shown in Figure 3-1B. Two-photon excited fluorescence (TPEF) was performed with an upright MPM system (Ultima Investigator; Bruker, Billerica, Massachusetts) with a femtosecond laser source tunable from 680 to 1300 nm (Spectra Physics, Insight DS+, Santa Clara, California). A Pockels cell was used to control the laser power at the sample (Model 350-80LA EOM, Model 302RM Driver, Conoptics, Danbury, Connecticut). The excitation and emission paths were coupled through a 16× long working distance (3 mm) water immersion objective (0.8 NA) (Nikon, CFl75 LWD 16X W, Tokyo, Japan), and separated by a dichroic mirror (Chroma, 755 nm long-pass, Bellows Falls, Vermont). A 750 nm short-pass filter was used as a clean-up filter in the detection path. The collected emission was split with a dichroic mirror (565 nm long-pass) into two detection channels, one with a 525/70 nm bandpass filter and the other with a 700/75 nm bandpass filter (Chroma). Multi-alkali PMTs (Hamamatsu Photonics, R6357, Hamamatsu City, Japan) were used for detection in both channels. Prairie View software (supplied by Bruker) was used to operate the MPM system and acquire images. The MPM FOV was 825 × 825 μm, with a sampling resolution of 805 nm/pixel.

3.2.3 Evaluating the imaging depth of MPM and SFDI

Imaging parameters from both SFDI and MPM modalities were used to characterize mouse mammary tumors. As these parameters were correlated across platforms, it was necessary to establish the imaging depth of both modalities to ensure the same tissue volumes were probed. This requires that the depth sensitivity of SFDI skew shallower given that the depth limiting modality is MPM. Ultimately, this means the longest

wavelength from a SFDI measurement (in this case, 851 nm) should not exceed the depth sensitivity of MPM. We describe here the methods utilized to evaluate imaging depth for both SFDI and MPM.

A phantom study was performed to compare the drop-off in contrast as a function of depth between the diffuse and nonlinear imaging techniques. A liquid phantom composed of deionized water, nigrosin (Sigma-Aldrich, St. Louis, Missouri) and titanium dioxide (Sigma-Aldrich) was fabricated to mimic average tumor optical properties (μ_a = 0.046 mm^{-1}, μ'_s = 0.71 mm^{-1}) that were determined from an in vivo study described in section 3.2.6. A glass capillary tube (~ 1 mm inner diameter) (Carolina Biological Supply Company, Product No. 711040, Burlington, North Carolina) was inserted horizontally through the phantom. The tube was filled with bovine blood (Carolina Biological Supply Company) to provide absorption contrast. Triton X-100 detergent (Sigma-Aldrich) was added to the liquid phantom at 0.1% V/V to alleviate surface tension between the liquid phantom and glass tube. The depth of the blood tube started at 0 mm (liquid phantom surface), and was effectively lowered by 0.1 mm increments by adding additional volume to the liquid phantom to a depth of 1.5 mm. A vertical translation stage was used to keep the surface of the liquid phantom at the same image plane, avoiding the need for SFDI height correction. SFDI measurements were made at 851 nm at the following spatial frequencies: f_x = [0, 0.05, 0.1] mm^{-1} (note that 0 mm^{-1} = DC).

The experiment was repeated to evaluate MPM contrast using a mixture of bovine blood and Evans Blue dye (2p-ex/em 1050/680 nm, MW 960.81 Da, Sigma-Aldrich, E2129) in the capillary tube. The concentration of the dye matched the concentration used

during intravital imaging (1.28 mg/mL). A glass coverslip (No. 1, 22 × 22 mm, Sigma-Aldrich, CLS284522) was placed between the objective and liquid phantom surface to protect the objective from the phantom. For each depth, the fluorescent blood tube was imaged with 2-by-3 tiling, where each tile had a FOV of 825 × 825 μm. Images were stitched together using a stitching plugin in FIJI[85]. To ensure that photobleaching was not responsible for the decay in fluorescence with depth, reverse (i.e., deeper to shallower) depth measurements were made and the fluorescent signal was found to be comparable to the fluorescent signal of the forward (i.e., shallower to deeper) depth measurements (data not shown).

The contrast-to-noise ratio (CNR) of the tube relative to the background was calculated at each depth for both modalities using

$$CNR = \frac{\mu_{tube} - \mu_{background}}{\left[w_{tube}\sigma_{tube}^2 + w_{background}\sigma_{background}^2\right]^{\frac{1}{2}}}, \quad (3.4)$$

where μ_{tube} is the mean signal from a region-of-interest (ROI) chosen on the tube, $\mu_{background}$ is the mean signal from an ROI within the background liquid phantom, σ_{tube} and $\sigma_{background}$ are the standard deviations (SD) calculated from these ROIs, and w_{tube} = #ROIpixels$_{tube}$ / (#ROIpixels$_{tube}$ + #ROIpixels$_{background}$) and $w_{background}$ = #ROIpixels$_{background}$ / (#ROIpixels$_{tube}$ + #ROIpixels$_{background}$) are the noise weights[86]. For SFDI, three equivalently sized line profiles were used as ROIs, one selected down the middle of the tube (μ_{tube}, σ_{tube}, #ROIpixels$_{tube}$), and two selected equally distant on either side of the tube ($\mu_{background}$, $\sigma_{background}$, #ROIpixels$_{background}$). CNR was calculated using μ_a at 851 nm for the following f_x pairs: (a) 0 and 0.1 mm^{-1}, and (b) 0.05 and 0.1 mm^{-1}. The choice of spatial frequencies

is based on our prior work which utilized MC simulations to show how SFDI depth sensitivity decreases with increasing f_x[87], and demonstrated how the choice of f_x pair affects optical property extraction errors[88]. For MPM, square ROIs were used for CNR analysis. The ROIs for SFDI and MPM CNR analysis were matched in terms of physical area. For each imaging domain, a single exponential decay curve was fit to the normalized CNR ($CNR_{normalized,fit}$) vs. depth (d) data to extract the exponential decay constant (α) of CNR with depth, which served as a measure for comparing depth sensitivities between imaging regimes:

$$CNR_{normalized,fit} = e^{-\alpha d}. \quad (3.5)$$

3.2.4 Estimating optical property uncertainties for SFDI

The choice of SFDI spatial frequency pair influences both the depth sensitivity and the ability to accurately extract optical properties. Optical property extraction uncertainties were quantified for different spatial frequency pairs using phantom measurements. Two tissue-simulating silicone-based homogeneous optical phantoms (both 21 × 21 cm) were measured with SDFI at nine different wavelengths ([471, 526, 591, 621, 659, 691, 731, 811 and 851] nm), giving a total of 18 different optical property pairs that spanned the following ranges: μ_a = 0.006-0.06 mm^{-1}, μ'_s = 0.668-1.50 mm^{-1}. Optical properties were processed for all measured wavelengths for the following f_x pairs: (a) 0 and 0.1 mm^{-1}, and (b) 0.05 and 0.1 mm^{-1}. Optical property averages and uncertainties were calculated for all 18 optical properties for each f_x pair by taking the mean and SD, respectively, over the entire detection FOV (8.7 × 6.5 cm).

3.2.5 Py230 murine mammary tumor model

The Py230 murine mammary tumor model was used for all tumor imaging. This cell line was originally derived from spontaneous mammary tumors arising from C57BL/6 MMTV-PyMT female mice[89]. Py230 cells were purchased from the American Type Culture Center (ATCC CRL-3279, Manassas, Virginia) and grown and expanded at 37°C in a humidified 5% CO_2 atmosphere in F-12 K culture medium containing 5% fetal clone II serum and supplemented with MITO serum extender, 100 Units/ml penicillin and 100 μg/mL streptomycin, and passaged in 1:3 when cells reach 70% to 80% confluency. Female C57BL/6 mice, approximately 5 to 6 weeks old (15-18 g), were purchased from Taconic Biosciences (model #B6-F, Rensselaer, New York) and were housed in the Boston University Laboratory Animal Care Facility. Approximately 10^6 Py230 cells were injected orthotopically into the inguinal 4th mammary fat pad in 50 μL 1X PBS using a U-100 insulin syringe with a 28.5 gauge needle (Product No. 329461, BD Biosciences, Franklin Lakes, New Jersey). Both mouse body weights and tumor volumes were measured every 3 to 4 days. Tumor length (L) and width (W) were measured using digital calipers (VWR International, Radnor, Pennsylvania), and tumor volume was calculated as $V_t = (\pi / 6) \times (L \times W)^{3/2}$. During window chamber surgeries and DNI measurements, mice were anesthetized using isoflurane by inhalation (5% induction, 2% inhalation) and kept on a 37°C circulating water heating pad to maintain physiological temperature. All animal work was reviewed and approved by the Boston University Institutional Animal Care and Use Committee.

3.2.6 Diffuse and nonlinear imaging of Py230 tumors through mammary imaging windows

Figure 3-2 provides a flowchart of DNI measurements of Py230 tumors. When tumor volumes reached ~150 mm^3, mice were implanted with a mammary imaging window (MIW) by removing the skin covering the tumor and using tissue adhesive to glue the surrounding skin onto the base of the MIW. Each MIW was fabricated a day before imaging as described elsewhere[62,90]. Briefly, the MIW consisted of a tissue grade plastic base and an 8 mm diameter circular glass coverslip (Product No. 64–0701, Harvard Apparatus, Holliston, Massachusetts). The plastic base was fashioned from a sterile polystyrene petri dish (AS4052; Thermo Fisher Scientific, Waltham, Massachusetts) using a heat-gun and dremel to form it into a flat washer-like structure with an outer diameter of 12 mm and an inner hole diameter of 7 mm. Superglue was then used to glue the 8 mm circular glass coverslip over the 7 mm inner hole of the plastic base, and the glue was allowed to dry for 15 to 20 minutes before sterilizing the entire MIW with 70% ethanol. On the day of imaging for each mouse, the MIW was sterilized again with 70% ethanol and allowed to dry before implanting it over the exposed mammary tumor. After implanting the MIW, SFDI measurements were taken through the MIW in live anesthetized mice at the following wavelengths and spatial frequencies: λ = [659, 691, 731, 851] nm, f_x = [0, 0.05, 0.1] mm^{-1}.

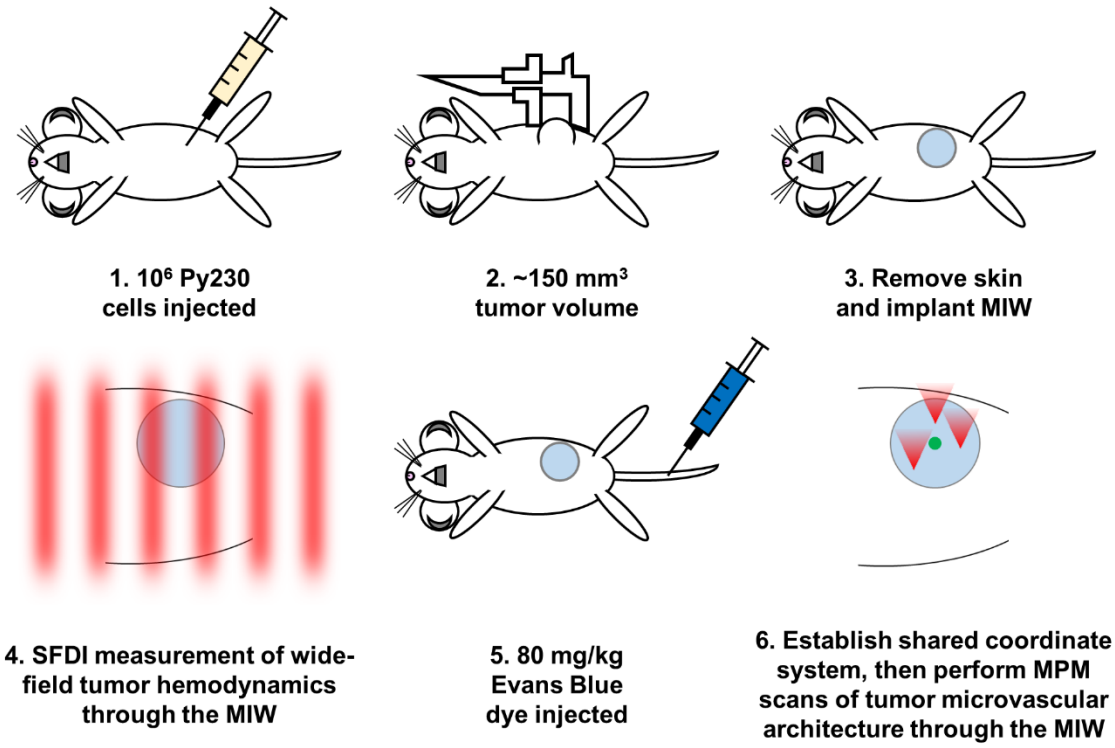

Figure 3-2: DNI mouse imaging procedure. (1) 10^6 Py230 murine mammary tumor cells were injected orthotopically into the inguinal 4th mammary fat pad of 5- to 6-week-old C57BL/6 female mice. (2) Tumors were allowed to grow untreated to approximately 150 mm^3. (3) At that point, the skin covering the tumor was removed and a MIW (7 mm imaging diameter) was implanted over the tumor. (4) SFDI measurements were made through the MIW at the following wavelengths and spatial frequencies: λ = [659, 691, 731, 851] nm, fx = [0, 0.05, 0.1] mm^{-1}. Following the SFDI measurements, a fluorescent marker (<1 mm in diameter) was applied to the MIW, and a planar illumination SFDI measurement was taken to establish the imaging origin in SFDI space for coregistration. (5) Evans Blue dye (2P-Ex/Em 1050/680 nm) was injected via the tail vein at a dose of 80 mg/kg to fluorescently label the tumor microvasculature. (6) After establishing the fluorescent fiducial mark as the origin in MPM space using a translation stage, two-photon scans of tumor microvascular architecture were performed throughout the MIW while recording the x-y spatial location of each scan relative to the fluorescent fiducial mark.

Following the SFDI measurement, a small fiducial mark (diameter < 1 mm) was applied to the center of the MIW using the tip of a 30.5 gauge needle dipped in yellow highlighter ink. With the mouse kept in the same position, a planar illumination SFDI measurement at 659 nm was taken to establish a frame of reference for spatial coregistration in post-processing. The mouse was then moved to the MPM sample stage, with the MIW directly underneath the MPM objective. To maintain rotational consistency between the systems, the heads and tails of the mice were always positioned in the same orientation for each imaging session for both instruments. A solution of Evans Blue dye (2p-ex/em 1050/680 nm) in 1X PBS was then injected via the tail vein at a dose of 80 mg/kg to fluorescently label the tumor microvasculature. After waiting 30 to 60 seconds for the dye to completely circulate, the mouse was euthanized. Immediately following euthanization, the yellow highlighter fiducial mark was established as the frame of reference using the MPM system's translation stage. Two-photon scanned 3D stacks of tumor microvascular architecture were then acquired throughout the MIW while recording the x-y spatial location of each scan relative to the fiducial mark.

The presence of the glass MIW imposed a linear perturbation to the sample's native diffuse reflectance (and thus optical properties) during SFDI measurements. This effect was empirically quantified by performing SFDI measurements on tissue-simulating optical phantoms with μ_a and μ'_s values that approximated Py230 tumor optical properties with and without glass coverslips covering the phantom (Supporting Information Figure S1). A linear R_d correction factor was then determined for each spatial frequency and wavelength and used to correct the in vivo Rd measurements of tumors imaged with SFDI.

3.2.7 Extraction of tumor microvasculature metrics from MPM data

The vascular image processing methods used and described herein are based on a pipeline developed by Gil et al.[91]. Moreover, each processing step has been used and validated for vascular image processing in prior works, and relevant references have been cited for each step. We have organized the text in this section to denote which steps are preprocessing steps, and which steps are vessel segmentation and metrics extraction steps. Tumor microvessel metrics, including vessel diameter, length, tortuosity, and density were extracted from the collected MPM 3D image stacks of tumor microvasculature using MATLAB R2017b. Figure 3-3 shows the processing flowchart.

Preprocessing: Each stack was first converted into a maximum intensity projection (MIP) image, where each pixel value in the MIP is the maximum value at the particular pixel location over all images in the stack. The MIP was then evaluated for artifacts and, if present, a mask was manually generated to exclude the identified artifacts. Quantification of microvascular metrics was only done within the unmasked region. To correct for non-uniform background levels, morphological erosion and dilation were performed on the MIP using the built-in MATLAB functions "imopen" and "strel" with a disk-shaped kernel to remove vessels with diameters less than 400 μm, leaving behind the background[92]. The result of this spatially filtered MIP was then subtracted from the original MIP. The image was then normalized between 0 and 1, followed by a contrast limited adaptive histogram equalization (CLAHE) process to increase local contrast in the image by making the vessel intensities more uniform[93–95].

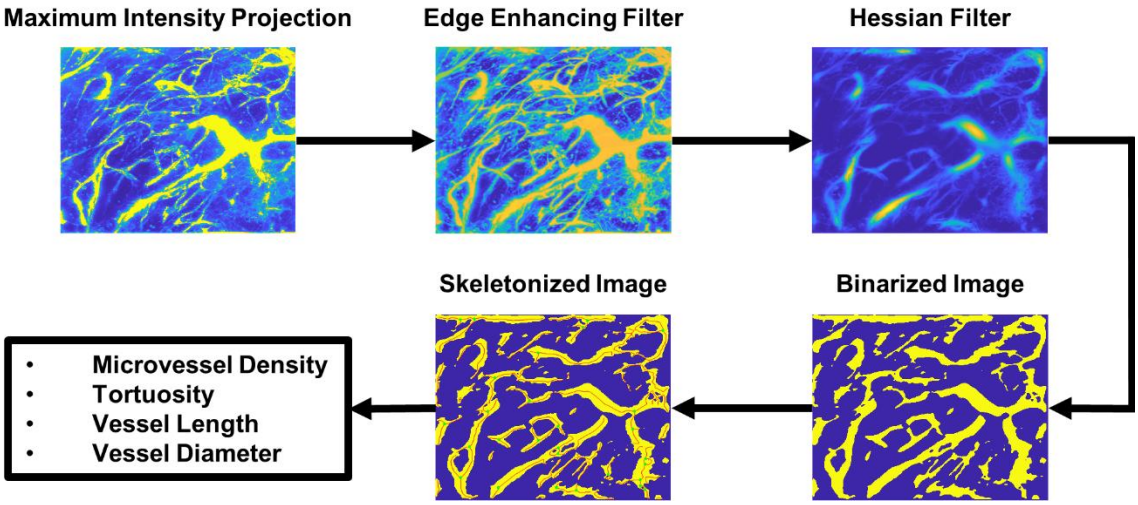

Figure 3-3: Processing flow for extracting microvascular architecture metrics from MPM scans of the tumor microvasculature through the MIW. After converting each microvascular stack into a MIP image, an anisotropic diffusion (edge enhancing) filter was used to enhance the edges of vessels, followed by a multiscale Hessian filter to accentuate vessel-like features relative to background. The filtered MIP images then underwent a binarization process to calculate microvessel density, followed by a skeletonization process to then extract microvascular metrics such as the diameter, length and tortuosity of each vessel.

Vessel segmentation: An anisotropic diffusion filter was applied to the resultant CLAHE processed image to enhance microvessel edges and suppress noise[96–100]. Another CLAHE process was performed on the diffusion filtered image, followed by multiscale Hessian filtering to accentuate vessel-like features[101]. Local adaptive segmentation was applied to the Hessian filtered image to binarize and isolate microvessels[102,103]. The binarized image and Hessian filtered image were fed into a Geodesic Active Contour segmentation algorithm using the built-in MATLAB function "activecontour" that resulted in a more refined segmented and binarized image with vessels in the foreground[104].

Metrics extraction: Tumor microvessel density for the final processed image was calculated by summing the number of vessel pixels and dividing by the total number of pixels in the unmasked region[105]. A skeletonized version of the final processed image with identified branch points was created using the built-in MATLAB function "bwmorph," defining a single vessel as between two branch points, from which the average diameter, length, and tortuosity values were calculated[106]. The diameter of each vessel was determined by using the distance transform of the segmented skeletonized vessels[105]. Length of each vessel was calculated as the sum of all the pixels between branch points multiplied by the MPM sampling resolution (0.805 μm/pixel)[105]. And finally, average tortuosity was calculated as the sum of all the vessel path lengths divided by the sum of all Euclidean distances between branch points[105].

3.2.8 Calculation of multiscale tumor vascular structure-function relationships

The fiducial mark on the MIW was used to establish the frame of reference for coregistration between SFDI and MPM. This marker was defined as the imaging origin (0,

0 μm), and the recorded x-y coordinates from the MPM scans were used to find the equivalent locations within the wide-field SFDI hemoglobin maps (HbO_2, HHb, THb and StO_2). Additional details about the coregistration process and the accuracy and precision of coregistration are included in Supporting Information (Figure S2). At each location, average hemoglobin metrics were determined within a square ROI with the same physical size as an MPM FOV (~825 × 825 μm). After pairing hemoglobin metrics with their corresponding microvascular metrics (i.e., microvessel diameter, length, tortuosity and density) for each MPM location within the MIW across all mice, the multiscale data set underwent an exploratory data analysis step to identify correlations between tumor microvascular architecture metrics and tissue-level hemodynamics. Correlation matrices were computed for all microvascular and hemodynamic metrics to identify multiscale pairwise correlations using the MATLAB function "corr." Correlation analyses were performed for both spatial frequency pairs (0 and 0.1 mm^{-1}, and 0.05 and 0.1 mm^{-1}).

3.2.9 Statistical analysis

We used the Pearson correlation coefficient (ρ_P) to evaluate multiscale correlations between each SFDI metric (HbO_2, HHb, THb and StO_2) with each MPM metric (microvessel density, tortuosity, vessel length and vessel diameter). We also employed the Spearman's rank correlation coefficient (ρ_S) as it evaluates a more general monotonic relationship between two metrics that is not specifically linear as is the case with Pearson, and it does not assume a bivariate normal distribution in the paired metrics when determining statistical significance. We assessed normality in the multiscale metrics using the Shapiro-Wilk test and made note of when a metric was rejected by the test (‡, i.e.,

metric is not from a normally distributed population). We took note of correlations with unadjusted P values less than 0.05 (*), and noted any correlations in which their adjusted P values were less than 0.05 (†). P values were adjusted using the Bonferroni (BF, conservative) and the Tukey-Ciminera-Heyse (TCH, less conservative) procedures to control for the type I error rate[107]. Table S1 summarizes our analysis.

3.3 Results

3.3.1 Multiscale depth penetration

Figure 3-4A depicts the experimental setup for evaluating the imaging depth of MPM and SFDI. Additionally, Figures 3-4B and 3-4C show the analyses and visualizations for the drop-off in contrast with depth for MPM and SFDI, respectively. Fluorescence contrast from MPM is visually apparent up to approximately 1 mm. For SFDI, the sensitivity to blood absorption contrast in the tube is visually apparent past 1 mm, although the contrast at the higher spatial frequencies (e.g., 0.1 mm^{-1}) drops-off more rapidly compared with lower spatial frequencies (e.g., DC). This agrees with our prior work which utilized MC simulations to show how SFDI depth sensitivity decreases with increasing f_x[87].

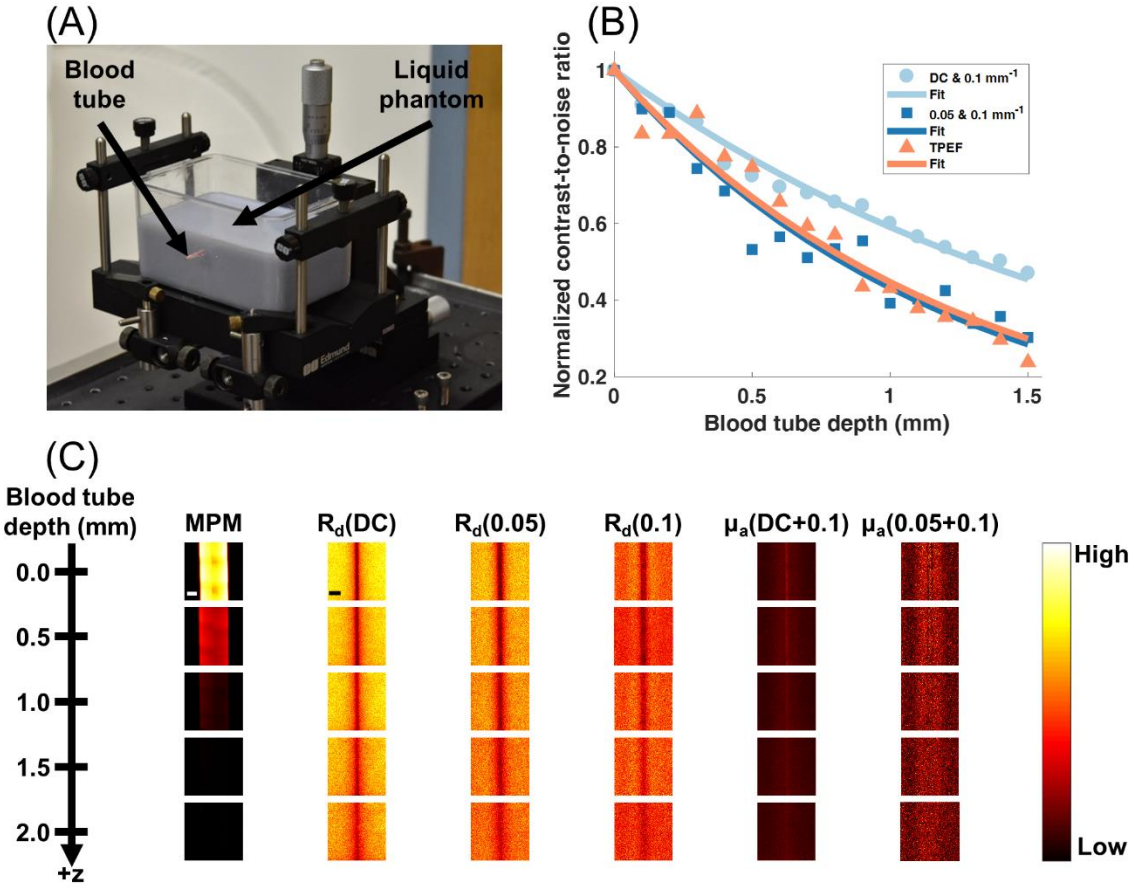

Figure 3-4: Comparison of depth penetration between SFDI and MPM based on imaging contrast as a function of depth. The depths at which either imaging regime loses sensitivity to their respective form of contrast (SFDI: hemoglobin absorption, MPM: fluorescently labeled vasculature) can serve as a metric for imaging depth penetration. (A) Experimental setup for evaluating contrast dependent depth penetration. For evaluating SFDI depth penetration, a 1 mm diameter glass capillary tube was filled with bovine blood and submerged in a liquid phantom that mimicked average Py230 tumor OPs (μ_a = 0.046 mm^{-1}, μ'_s = 0.71 mm^{-1}). The blood tube was measured with SFDI at incremental depths below the surface of the liquid phantom. For evaluating MPM depth penetration, the same experimental setup and procedure as SFDI was performed, with the addition of Evans Blue dye being mixed with bovine blood in the capillary tube to mimic fluorescent labeling of vasculature at a concentration similar to that used for in vivo imaging. The experiment was carried out on a single experimental setup. (B) A plot of normalized contrast-to-noise (CNR) versus blood tube depth beneath the surface of the liquid phantom. The orange triangle (▲) data points represent two-photon imaging of Evans Blue dye mixed with bovine blood in the capillary tube (TPEF Ex/Em 1050/680 nm). The blue circle (●) and square (■) data points represent the different SFDI CNR versus depth curves based on hemoglobin absorption contrast at 851 nm for different pairs of spatial frequencies, demonstrating the tunability of SFDI imaging depth with spatial frequency choices. The following are the exponential decay constants (α) with their 95% confidence bounds, and goodness-of-fit (R^2) values for [DC & 0.1 mm^{-1}, 0.05

& 0.1 mm^{-1}, TPEF], respectively: = [0.53, 0.84, 0.81]/mm, 95% confidence bounds on α = [(0.50, 0.55), (0.76, 0.91), (0.73, 0.88)]/mm, R2 = [0.98, 0.94, 0.95]. (C) Visualization of contrast dependent depth penetration for both modalities. Diffuse reflectance (R_d) and absorption (μ_a) images are at 851 nm. Measurements at 2 mm were taken to visually demonstrate the deeper penetration with DC as compared to higher spatial frequencies. MPM (white) scale bar = 250 µm, SFDI (black) scale bar = 5 mm.

Crucially, we found that the depth sensitivity in μ_a can be tuned based on the choice of SFDI spatial frequency pairs. For example, we found that a choice of 0.05 and 0.1 mm^{-1} skews substantially shallower compared with DC and 0.1 mm^{-1}, and this effect can be used to match the dropoff in contrast with MPM. This can be visually seen when comparing the μ_a columns in Figure 3-4C. The tube contrast disappears at approximately 1 mm with 0.05 and 0.1 mm^{-1}, whereas the tube can be seen beyond 1 mm with DC and 0.1 mm^{-1}. This can also be seen in Figure 3-4B, which shows the normalized CNR as a function of depth. The drop-off in contrast for 0.05 and 0.1 mm^{-1} ($\alpha = 0.84$ mm^{-1}) more closely matched that of MPM ($\alpha = 0.81$ mm^{-1}) compared with DC and 0.1 mm^{-1} ($\alpha = 0.53$ mm^{-1}). These results were repeated for other SFDI wavelengths (Figure S3). Because chromophore concentrations are directly linked to μ_a values through a linear transformation using Beer's law, chromophore contrast will follow similar decay characteristics. This suggests the hemoglobin depth contrast with SFDI, at 0.05 and 0.1 mm^{-1}, closely matches MPM microvascular depth contrast for our setup. This provides the opportunity to correlate structure-function relationships between the systems with matching depth sensitivities.

3.3.2 Optical property uncertainties as a function of spatial frequency choices

The choice of SFDI f_x pairs affects both the depth sensitivity of SFDI (as demonstrated in the previous section), as well as the ability to accurately extract optical

properties[87,88]. To assess tradeoffs between these two factors, we quantified optical property uncertainties for DC and 0.1 mm^{-1}, and 0.05 and 0.1 mm^{-1} given that the former has been identified as a f_x pair that minimizes optical property extraction errors[21,88], and the latter was found to provide good agreement in depth sensitivity between SFDI and MPM. We found that there was good agreement in extracting optical properties between the two spatial frequency pairs for a range of optical properties (Figure 3-5). On average, the 0.05 and 0.1 mm^{-1} f_x pair overestimated μ_a by 0.00026 mm−1 and underestimated μ'_s by 0.00097 mm^{-1} compared with the DC and 0.1 mm^{-1} f_x pair, demonstrating very little bias. However, we found a 3× increase in uncertainty in μ_a and a 1.4× increase in uncertainty in μ'_s with 0.05 and 0.1 mm^{-1} compared with DC and 0.1 mm^{-1} when considering the tumor optical property range (gray-shaded areas in Figure 3-5 plots). These results agreed with the SFDI optical property uncertainties predicted using the Cramér-Rao lower bound methodology recently described by Pera et al. (3.4× and 1.4×, respectively)[88]. It should be noted that uncertainties in either μ_a or μ'_s for a given sample are dependent on both the μ_a and μ'_s of that sample, as well as on the diffuse reflectance error model that is unique to the SFDI instrumentation. Together these results indicate that the 0.05 and 0.1 mm^{-1} fx pair better matches MPM in imaging depth, although at the cost of a modest sacrifice in optical property uncertainties.

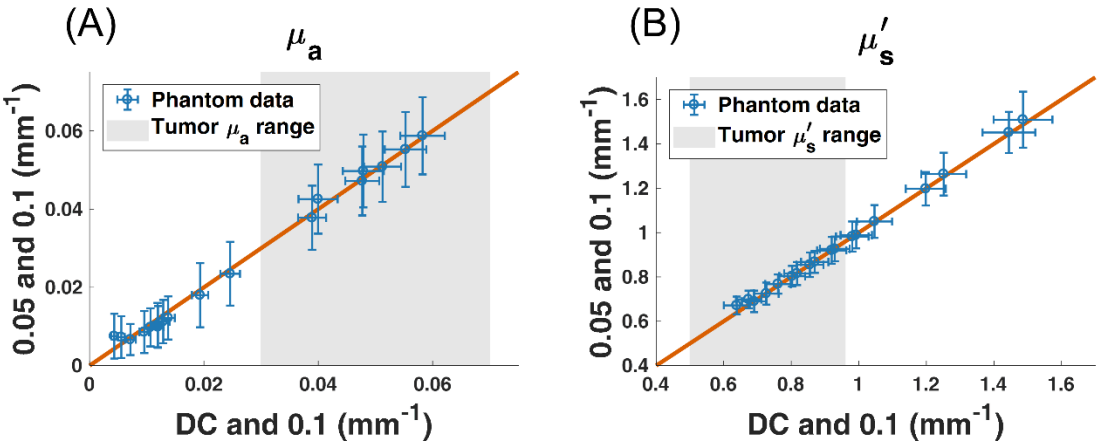

Figure 3-5: Comparison of (A) absorption (μ_a) and (B) reduced scattering (μ'_s) uncertainties for SFDI measurements taken with DC and 0.1 mm^{-1} vs 0.05 and 0.1 mm^{-1} f_x pairs in homogeneous tissue-mimicking optical phantoms. Two phantoms were measured with SFDI at nine different wavelengths ([471, 526, 591, 621, 659, 691, 731, 811, 851] nm), giving a total of 18 different optical property (OP) pairs. The gray region in each plot represents the OPs that fall within the 10% to 90% range of Py230 OPs (μ_a = 0.03:0.07 mm^{-1}, μ'_s = 0.50:0.96 mm^{-1}). OP extraction at 0.05 and 0.1 mm^{-1} are plotted against OP extraction at DC and 0.1 mm^{-1}, with the identity line shown. Uncertainty (error bars) was determined by calculating the SD over the entire imaging field-of-view (8.7 × 6.5 cm^2) for each OP measurement. Note that the errors in OP extractions are a function of both μ_a and μ'_s.

3.3.3 DNI of multiscale vascular parameters in murine mammary tumors

Figure 3-6 provides an example of DNI in a single mouse. Figure 3-6A shows a white light image of the tissue within the MIW. The MIW in this mouse was implanted such that at least half of the MIW contained tumor tissue with the rest of the window containing mammary fat pad and muscle. The spatial location of each tissue type relative to the fiducial mark was recorded. Figure 3-6C shows a THb map across the MIW, with representative coregistered MPM scans of vascular architecture. Substantial differences in THb and vascular architecture were observed in the different tissue types. For example, the muscle region was well vascularized with normalized vascular architecture, which corresponded with high levels of THb. On the other hand, the tumor regions contained abnormal vascular architecture, with corresponding low levels of THb. The fat pad was less vascularized, corresponding to low levels of THb. The table in Figure 6 provides technical specifications for the DNI method.

In total, DNI was used to measure eight tumors from eight female C57BL/6 mice, of which six had good quality SFDI and MPM data. The average tumor volume was 170 ± 78 mm^3. On average, the maximum depth of imaging with MPM in the tumors was approximately 600 μm. The number of MPM ROIs collected per mouse was on average 4 to 5 regions. Each DNI session took on average 30 to 45 minutes.

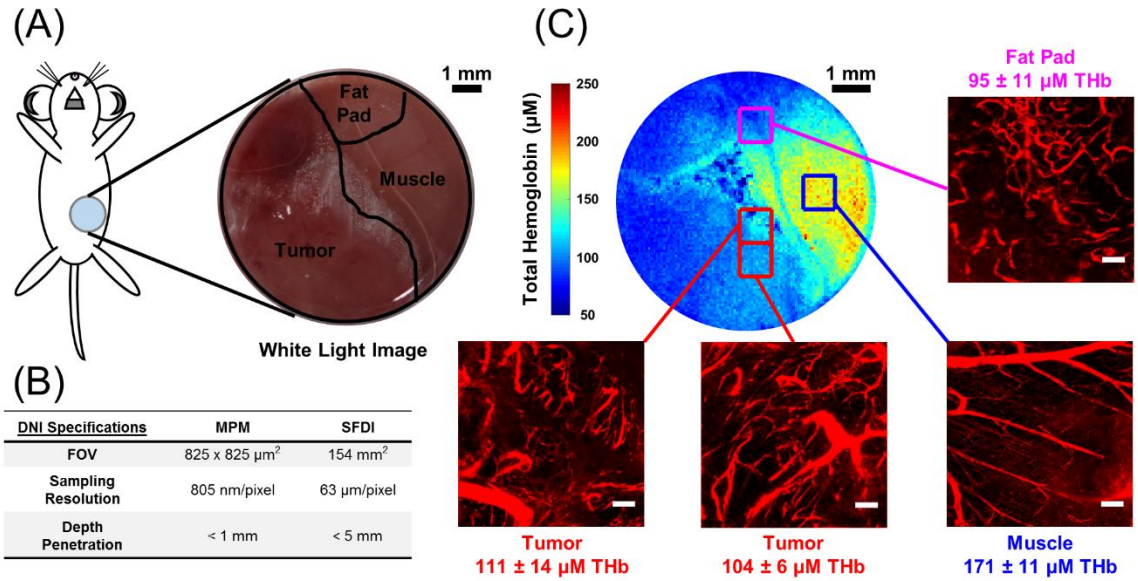

DNI Specifications	MPM	SFDI
FOV	825 x 825 μm^2	154 mm^2
Sampling Resolution	805 nm/pixel	63 μm/pixel
Depth Penetration	< 1 mm	< 5 mm

Figure 3-6: An example of in vivo DNI in a Py230 murine mammary tumor through a MIW. (A) A white light image of tumor and non-tumor tissue underneath the MIW, with different tissue regions identified. (B) A table detailing imaging specifications of the DNI technique. (C) The corresponding wide-field map of total hemoglobin (THb) concentration from SFDI is shown over the MIW from (A), followed by several two-photon scanned microvascular regions coregistered within the wide-field map. This particular example demonstrates the simultaneous functional and architectural differences between tumor regions and non-tumor regions. White scale bars = 100 μm.

To evaluate whether the choice of SFDI f_x pair affected the strength of multiscale vascular structure-function relationships, all SFDI measurements were processed with both DC and 0.1 mm^{-1}, and 0.05 and 0.1 mm^{-1} For each spatial frequency pair, we evaluated multiscale correlations using both the Pearson correlation coefficient (ρ_P) and Spearman's rank correlation coefficient (ρ_S) between each SFDI metric (HbO_2, HHb, THb and StO_2) with each MPM metric (microvessel density, tortuosity, vessel length and vessel diameter). This resulted in 16 multiscale correlations being evaluated simultaneously for a given correlation test and spatial frequency pair. Table S3-1 summarizes our overall findings. There were two identified Pearson correlations for 0.05 and 0.1 mm^{-1} with unadjusted P values less than 0.05 (StO_2 and vessel diameter, StO_2 and vessel length) and none for DC and 0.1 mm^{-1}. The same two Pearson correlations were also identified with Spearman for 0.05 and 0.1 mm^{-1} with unadjusted P values less than 0.05, and no identified Spearman correlation in the case of DC and 0.1 mm^{-1}. The two 0.05 and 0.1 mm^{-1} Pearson correlations had TCH adjusted P values less than 0.05. No correlations were deemed significant at a significance level of 0.05 when adjusting P values with the Bonferroni procedure.

In addition, we found that the 0.05 and 0.1 mm^{-1} f_x pair strengthened the two identified multiscale vascular relationships that were not discernable when processed with DC and 0.1 mm^{-1}, which may be attributable to the improved depth matching between SFDI and MPM. Figures 3-7A and 3-7B demonstrate the difference between the spatial frequency pairs when analyzing the relationship between tumor oxygen saturation (StO_2) captured with SFDI and vessel diameter extracted from MPM from the six tumors (25 ROIs). A weak negative correlation between StO_2 and vessel diameter was observed with

DC and 0.1 mm^{-1} ($\rho_P = -0.20$, $P = 0.33$ | $\rho_S = -0.10$, $P = 0.65$), and a much stronger negative correlation was observed with 0.05 and 0.1 mm^{-1} ($\rho_P = -0.50$, *†$P = 0.010$ | $\rho_S = -0.49$, *$P = 0.014$). Likewise, a similar phenomenon was observed when analyzing the relationship between StO_2 and vessel length for the same six tumors (25 ROIs). A weak negative correlation between StO_2 and vessel length was observed with DC and 0.1 mm^{-1} ($\rho_P = -0.28$, $P = 0.18$ | $\rho_S = -0.14$, $P = 0.52$), and a much stronger negative correlation was observed with 0.05 and 0.1 mm^{-1} ($\rho_P = -0.50$, *†$P = 0.011$ | $\rho_S = -0.48$, *$P = 0.016$). Figure S4 in Supporting Information shows representative MPM microvascular images from each mouse (n = 6) plotted next to their respective multiscale vascular parameter data points to visualize microvascular morphology in the context of extracted metrics.

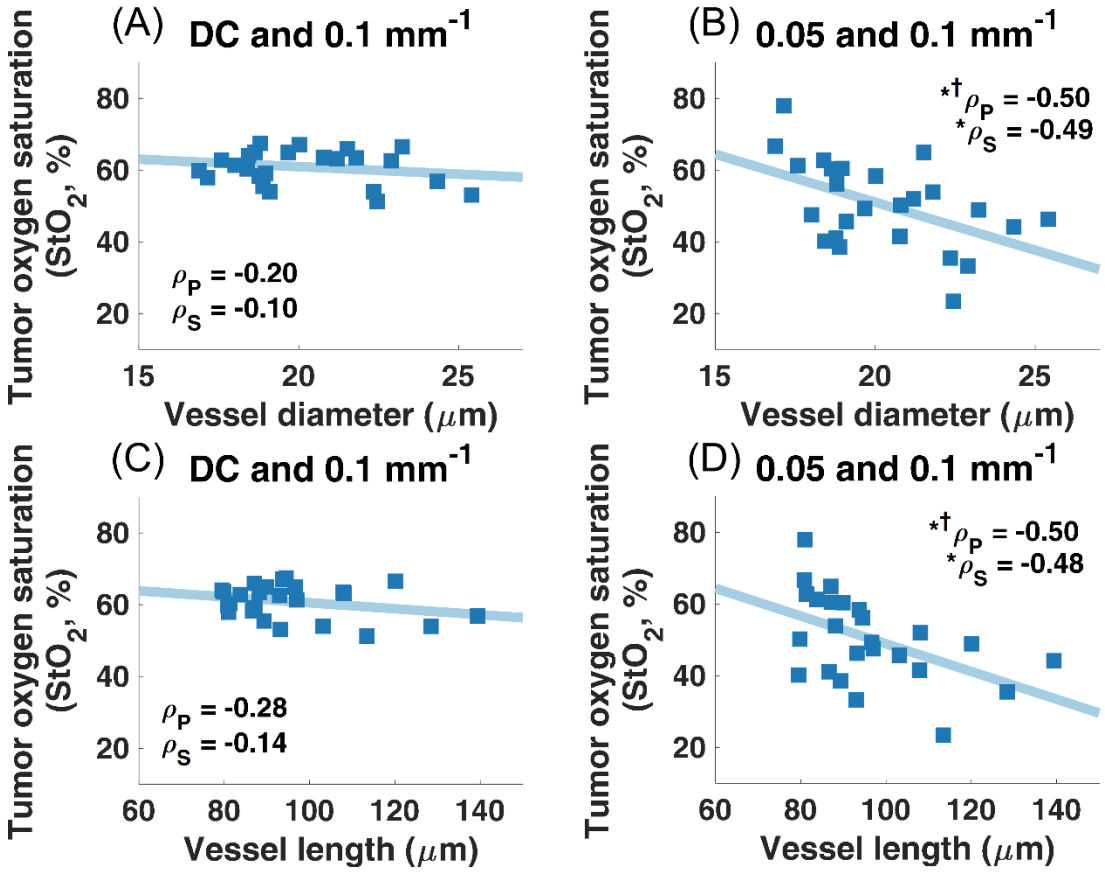

Figure 3-7: Multiscale relationships between tumor vasculature structure and function in Py230 tumors. These multiscale relationships became stronger when the 0.05 and 0.1 mm^{-1} f_x pair (B and D) was used for SFDI compared with the DC and 0.1 mm^{-1} f_x pair (A and C). Each point in the plots represents multiscale data from a tumor region in the MIW equivalent in size to the MPM FOV (~825 × 825 µm). Each axis, and thus each data point, represents average values within a given region extracted from their respective imaging modality and over the same region (SFDI: StO_2; MPM: vessel diameter, vessel length extracted from MIPs). The data comes from 25 regions from six tumors. The lines represent the lines of best fit to the data in each plot. The Pearson's ρ (ρ_P) and Spearman's ρ (ρ_S) are reported for each plot. *Denotes unadjusted P < 0.05, and † denotes Tukey-Ciminera-Heyse (TCH) adjusted P < 0.05.

3.4 Discussion

In this work, we developed and validated DNI as a new multiscale preclinical imaging method for the coregistration of tissue-level tumor hemodynamics captured with SFDI, and tumor microvascular architecture imaged with MPM. High x-y spatial coregistration accuracy and precision (≤50 μm) was demonstrated between SFDI and MPM. In addition, the appropriate selection of SFDI spatial frequency pair was shown to aid in matching MPM imaging depth. Importantly, this proved to be useful in elucidating multiscale vascular structure-function relationships in a proof-of-concept study in which DNI was used to image untreated murine mammary tumors through MIWs.

One of the enabling features of this work was the ability to match imaging depth of SFDI and MPM. The enhanced similarity in imaging depth between SFDI and MPM with 0.05 and 0.1 mm^{-1} as opposed to DC and 0.1 mm^{-1} can be largely attributed to SFDI depth sensitivity decreasing with increasing f_x^{87}. We believe this effect largely contributed to the increased strength of the identified multiscale correlations. It is of note that correlation strength for the identified multiscale correlations increased when using 0.05 and 0.1 mm^{-1} despite the slightly higher uncertainty in μ_a extractions, suggesting depth matching is highly important for evaluating these correlations, and that microvessel morphology may change with tumor depth. This was confirmed by CD31 staining of a resected tumor which demonstrated that tumor microvasculature varies substantially with depth (Figure S5).

Following depth matching, we found that wide-field StO_2 had strong negative correlations with microvessel diameter and length. This suggestive correlation between StO_2 and microvessel diameter is consistent with prior reports that have shown hypoxic

tumor regions are associated with dilated microvessels[80,81]. Likewise, the suggestive correlation between StO_2 and microvessel length may be also be related to the abnormal growth of microvasculature in hypoxic regions, although this relationship has not been studied to the same extent in prior work.

This work has several important implications. First, multiscale DNI metrics provide a link between the large but previously disconnected bodies of prior work focused on either the preclinical and clinical settings. For example, microvascular metrics, including vessel diameter, length, and tortuosity, have been studied extensively in the context of treatment response in small animal tumor models[29,30,78–81]. In contrast, wide-field hemodynamic metrics (StO_2, THb, etc.) have been studied extensively in the clinical setting with DOI technologies[1,2,4,5,10,74–77,108]. DNI allows these parameters to be tracked together within a single tumor, which provides a means to explore new agents and treatment schedules in the preclinical setting while evaluating the likely clinical manifestations of these treatments. Several reports have shown a positive correlation between THb concentration measured with DOI and vessel density quantified from histology of tumor biopsy specimens from breast cancer patients[22–26]. For example, in 2011, it was reported that pretreatment THb concentrations correlated with pretreatment mean vessel density of CD105-expressing neovasculature in breast cancer patients with a pathologic complete response[22]. While this prior work is encouraging, DNI expands the repertoire of multiscale metrics that can be studied while providing a means to track them longitudinally in a spatially coregistered manner. Finally, both diffuse and nonlinear imaging can measure a wide variety of contrasts beyond those related to the vasculature, such as optical scattering

with DOI, and cellular metabolism/redox and collagen architecture with nonlinear microscopy techniques such as TPEF/fluorescence lifetime imaging microscopy and second harmonic generation (SHG), respectively[34,109]. These contrast mechanisms can be exploited to validate and discover an array of novel biological and physiological multiscale relationships to obtain a more complete picture of the in vivo tumor state.

While this is the first study to combine SFDI and MPM for tumor imaging, this combination of modalities has been previously utilized for applications in human skin. For example, Balu et al.[64] demonstrated that changes in wide-field hemodynamics measured with SFDI strongly correlate with changes in NADH fluorescence measured with MPM during an arterial occlusion. In addition, Saager et al.[65] showed that independent measurements of melanin volume fraction and distribution thickness by SFDI and MPM across various human skin types were strongly correlated. These studies suggest that there is much to be gained from exploring multiscale relationships to generate a holistic picture of underlying biological and physiological mechanisms. We add to this work novel methods of coregistering and depth matching SFDI and MPM, applying the methods to small animal tumor imaging, and investigating spatial heterogeneity in multiscale relationships.

The DNI method presented here has limitations that can be mitigated going forward. For example, although we achieved high accuracy and precision in coregistration through the use of a fiducial marker, this aspect could be further improved through the use of a single sample stage so that both forms of imaging can be performed through an intrinsically shared coordinate system. Additionally, for this feasibility study we performed

MPM imaging in euthanized mice to avoid the need to correct for motion artifacts. The microvascular architecture remained intact within 1 hour post-euthanization as indicated by minimal dye leakage (data not shown). Going forward, longitudinal monitoring of multiscale vascular relationships in live mice will enhance the ability to understand treatment response and resistance.

3.5 Conclusion

In conclusion, we have developed a diffuse and nonlinear imaging method to quantify tumor vascular structure– function relationships across length scales. This will lay the foundation for identifying translational imaging metrics of response and resistance, and create a path toward diffuse optical image-guided adaptive therapy for long term tumor control.

3.6 Acknowledgements

The authors would like to thank the following individuals for their helpful discussions: Matthew Applegate, Carole Hayakawa, Vasan Venugopalan and Irving Bigio. The authors would also like to thank Matthew Applegate for providing the MPM system diagram and Irving Bigio for lending the vertical translation stage. The authors thank Asha Pant and John Jiang for assistance with the conducted mice study, Daniel Gil for sharing base code to process MIPs of microvascular architecture for the extraction of microvessel metrics, Fay Wang for assistance with MIW fabrication, Elizabeth Suki for use of the bright-field microscope to image histology slides, and Raeef Istfan for making the silicone phantoms measured in this study. The authors gratefully acknowledge funding from the

U.S. Department of Defense (DoD) (Award No. W81XWH-15-1-0070), as well as funding from the National Cancer Institute of the National Institutes of Health (NIH) (Award No. F99CA223014). The content is solely the responsibility of the authors and does not necessarily represent the official views of the NIH.

3.7 Supplementary Materials

3.7.1 Supporting information

The material in Section 3.7.1 were submitted as supporting information for work published in the Journal of Biophotonics[73] with the following contributing authors:

Kavon Karrobi[a], Anup Tank[a], Syeda Tabassum[b], Vivian Pera[a], and Darren Roblyer[a]

[a] Department of Biomedical Engineering, Boston University, Boston, Massachusetts

[b] Department of Electrical and Computer Engineering, Boston University, Boston, Massachusetts

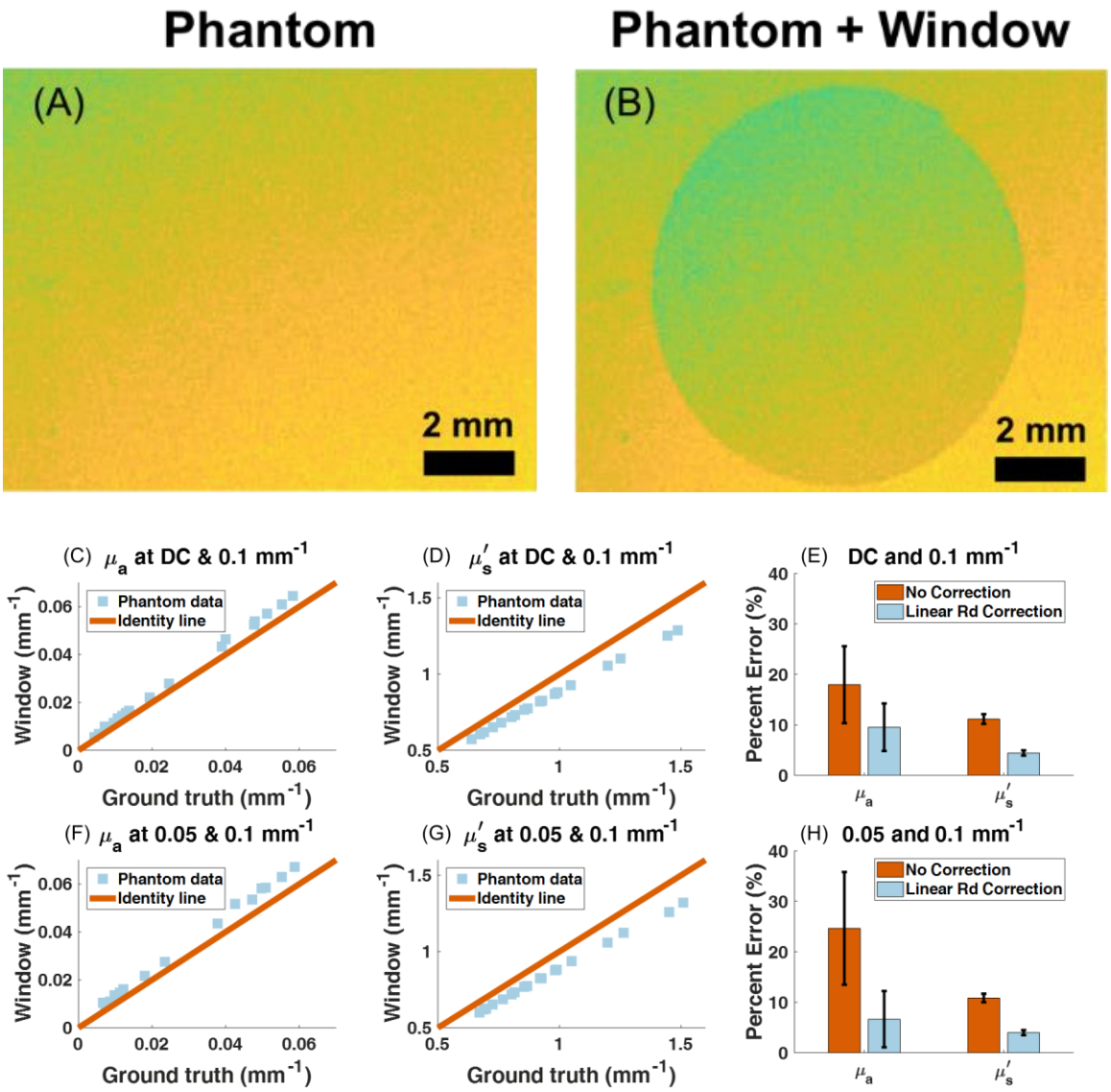

Figure S3-8: Correcting for the influence of the MIW on optical property extractions. Two homogeneous tissue-mimicking optical silicone phantoms were imaged with SFDI at 9 different wavelengths (([471 526 591 621 659 691 731 811 851] nm) and 8 different spatial frequencies ([DC 0.05 0.1 0.15 0.2 0.3 0.4 0.5] mm^{-1}), with and without an imaging glass (i.e., window) covering the entire FOV. This is shown in (A) and (B) at 471 nm DC illumination. The window introduced a linear deviation from the ground truth optical properties as shown in (C), (D), (F), and (G). This linear deviation was also observed in R_d (not shown). (E) and (H) show the comparison between no correction and applying a linear correction in R_d to account for the window. This correction minimizes the optical property error to below 10% for both μ_a and μ'_s.

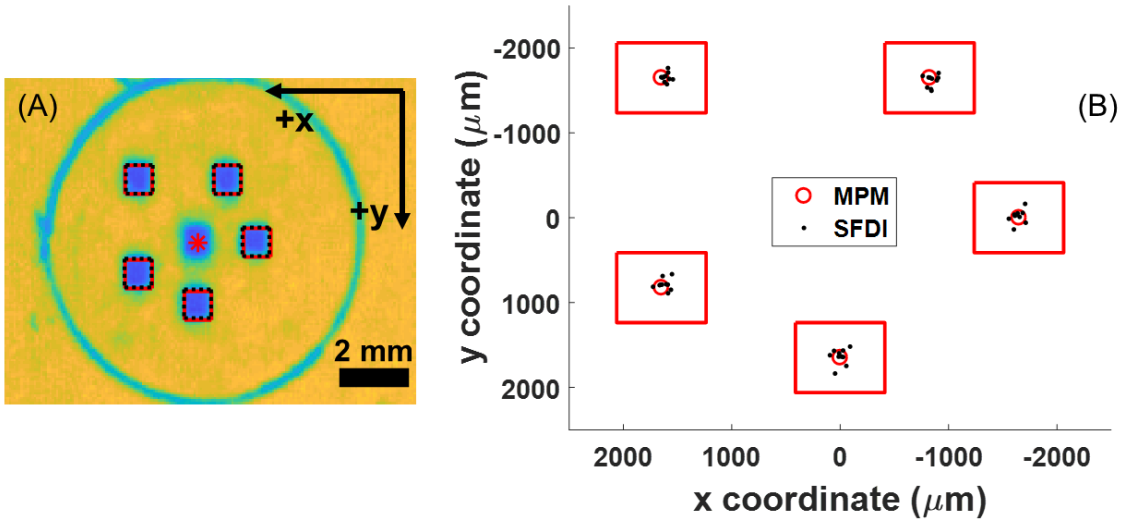

(C)

Spatial coordinate	Accuracy	Precision
X	43 μm	30 μm
Y	55 μm	51 μm

Figure S3-9: DNI coregistration accuracy and precision. (A) A custom calibration target was fabricated to quantify the (x,y) spatial coregistration between the SFDI and MPM imaging systems. The calibration target was fashioned from thermal-sensitive paper. Six square 824.57 by 824.57 μm^2 areas were burned into the target using two-photon absorption. The center square was deemed as the "fiducial mark," and its x-y location (red asterisk) was defined as (0 μm, 0 μm) on the MPM translation stage. The remaining five surrounding squares were deemed as regions-of-interest (ROIs) and their locations were defined in reference to the fiducial mark. The calibration target was then imaged with SFDI. The locations of each ROI within the SFDI image were then predicted based on their respective (x,y) coordinates (red solid squares). These locations were compared to the center-of-mass locations of each ROI calculated from the SFDI planer image (black dotted squares). The red asterisk in (A) indicates the origin (0,0) μm in SFDI space. (B) A plot representing the 5 surrounding ROIs from the calibration target with red squares, with the red center circle in each square representing the MPM spatial coordinates, and the black dots representing the SFDI spatial coordinates determined from center of mass calculations for 10 trials for each of the ROIs. (C) The accuracy of coregistration was calculated based on the x and y discrepancies between the predicted (MPM) and measured (SFDI) ROI locations, and this was repeated 10 times to calculate precision.

wide-field (SFDI)	μ-vascular (MPM)	0.05 and 0.1 mm^{-1}								
		Pearson's ρ	Unadjusted p-value	TCH adjusted p-value	BF adjusted p-value	Spearman's ρ	Unadjusted p-value	TCH adjusted p-value	BF adjusted p-value	|Fisher's z|
$^{*PaSa,\dagger Pa}StO_2$ (%)	$^{*PaSa,\dagger Pa}$diameter (μm)	-0.503	0.010	0.041	0.165	-0.489	0.014	0.055	0.224	0.554
$^{*PaSa,\dagger Pa}StO_2$ (%)	$^{*PaSa,\dagger Pa,\ddagger}$length (μm)	-0.499	0.011	0.044	0.178	-0.479	0.016	0.064	0.262	0.548
$^{\ddagger b}$HHb (μM)	‡length (μm)	0.325	0.113	0.380	1.000	0.356	0.081	0.287	1.000	0.337
$^{\ddagger a}HbO_2$ (μM)	diameter (μm)	-0.315	0.125	0.415	1.000	-0.290	0.159	0.501	1.000	0.326
$^{\ddagger a}HbO_2$ (μM)	‡length (μm)	-0.262	0.206	0.603	1.000	-0.138	0.508	0.941	1.000	0.268
$^{\ddagger b}$HHb (μM)	tortuosity	0.249	0.230	0.649	1.000	0.275	0.183	0.555	1.000	0.254
$^{\ddagger b}$HHb (μM)	diameter (μm)	0.214	0.304	0.765	1.000	0.182	0.381	0.854	1.000	0.218
StO_2 (%)	density (%)	-0.196	0.348	0.819	1.000	-0.103	0.623	0.980	1.000	0.198
$^{\ddagger a}$THb (μM)	diameter (μm)	-0.192	0.358	0.831	1.000	-0.049	0.815	0.999	1.000	0.194
$^{\ddagger a}$THb (μM)	tortuosity	0.177	0.398	0.869	1.000	0.162	0.439	0.901	1.000	0.179
StO_2 (%)	tortuosity	-0.142	0.497	0.936	1.000	-0.124	0.554	0.960	1.000	0.143
$^{\ddagger a}$THb (μM)	‡length (μm)	-0.125	0.552	0.960	1.000	0.110	0.599	0.974	1.000	0.125
$^{\ddagger a}HbO_2$ (μM)	tortuosity	0.119	0.572	0.966	1.000	0.074	0.725	0.994	1.000	0.119
$^{\ddagger a}HbO_2$ (μM)	density (%)	-0.040	0.850	0.999	1.000	-0.101	0.631	0.981	1.000	0.040
$^{\ddagger b}$HHb (μM)	density (%)	0.020	0.923	1.000	1.000	-0.118	0.574	0.967	1.000	0.020
$^{\ddagger a}$THb (μM)	density (%)	0.000	0.999	1.000	1.000	-0.094	0.654	0.986	1.000	0.000

wide-field (SFDI)	μ-vascular (MPM)	DC and 0.1 mm^{-1}								
		Pearson's ρ	Unadjusted p-value	TCH adjusted p-value	BF adjusted p-value	Spearman's ρ	Unadjusted p-value	TCH adjusted p-value	BF adjusted p-value	|Fisher's z|
$_{*}^{PaSa,\dagger Pa}StO_2$ (%)	$_{*}^{PaSa,\dagger Pa}$diameter (μm)	-0.203	0.329	0.798	1.000	-0.096	0.646	0.984	1.000	0.206
$_{*}^{PaSa,\dagger Pa}StO_2$ (%)	$_{*}^{PaSa,\dagger Pa,\ddagger}$length (μm)	-0.278	0.178	0.544	1.000	-0.135	0.517	0.946	1.000	0.286
$^{\ddagger b}$HHb (μM)	‡length (μm)	0.175	0.403	0.873	1.000	0.361	0.077	0.275	1.000	0.177
$^{\ddagger a}HbO_2$ (μM)	diameter (μm)	-0.183	0.381	0.854	1.000	-0.158	0.448	0.907	1.000	0.185
$^{\ddagger a}HbO_2$ (μM)	‡length (μm)	-0.175	0.402	0.872	1.000	-0.048	0.818	0.999	1.000	0.177
$^{\ddagger b}$HHb (μM)	tortuosity	0.262	0.206	0.603	1.000	0.293	0.155	0.490	1.000	0.268
$^{\ddagger b}$HHb (μM)	diameter (μm)	0.012	0.954	1.000	1.000	0.099	0.636	0.982	1.000	0.012
StO_2 (%)	density (%)	-0.014	0.947	1.000	1.000	0.068	0.747	0.996	1.000	0.014
$^{\ddagger a}$THb (μM)	diameter (μm)	-0.170	0.418	0.885	1.000	-0.098	0.641	0.983	1.000	0.171
$^{\ddagger a}$THb (μM)	tortuosity	0.091	0.666	0.988	1.000	0.128	0.541	0.956	1.000	0.091
StO_2 (%)	tortuosity	-0.066	0.752	0.996	1.000	-0.080	0.703	0.992	1.000	0.067
$^{\ddagger a}$THb (μM)	‡length (μm)	-0.121	0.563	0.964	1.000	0.002	0.993	1.000	1.000	0.122
$^{\ddagger a}HbO_2$ (μM)	tortuosity	0.027	0.899	1.000	1.000	0.018	0.931	1.000	1.000	0.027
$^{\ddagger a}HbO_2$ (μM)	density (%)	-0.125	0.550	0.959	1.000	-0.095	0.649	0.985	1.000	0.126
$^{\ddagger b}$HHb (μM)	density (%)	-0.162	0.440	0.902	1.000	-0.294	0.154	0.487	1.000	0.163
$^{\ddagger a}$THb (μM)	density (%)	-0.159	0.448	0.907	1.000	-0.110	0.599	0.974	1.000	0.160

Table S3-1: Multiscale vascular relationships explored in Py230 tumors. This table includes all 16 multiscale correlations tested between MPM (μ-vascular) metrics and SFDI (wide-field) metrics for each spatial frequency pair (a = 0.05 and 0.1 mm^{-1}, b = DC and 0.1 mm^{-1}). For each evaluated multiscale correlation for a given frequency pair, the Pearson (P) correlation coefficient and Spearman's (S) rank correlation coefficient were computed, along with their respective unadjusted p-values. The p-values were adjusted using both the Tukey-Ciminera-Heyse (TCH) and Bonferroni (BF) procedures to control for the type I error rate. The absolute value of the Fisher z-transformation was also computed from the Pearson's ρ, and the multiscale correlations were arranged from largest to smallest (going down the table) based on the absolute value of their computed Fisher's z. * indicates that the unadjusted p-value is < 0.05 for a given correlation metric of a given multiscale relationship (e.g., *PaSa indicates that the unadjusted p-values are < 0.05 for both the Pearson and Spearman correlation coefficients only for the frequency pair 0.05 and 0.1 mm^{-1}). † indicates that the TCH adjusted p-value is < 0.05 for a given correlation metric of a given multiscale relationship (e.g., †Pa indicates that the TCH adjusted p-value is < 0.05 for the Pearson correlation coefficient only for the frequency pair 0.05 and 0.1 mm^{-1}). ‡ indicates that a given vascular metric did not pass the Shapiro-Wilk test (i.e., metric is not from a normally distributed population). a or b next to ‡ indicates that the SFDI metric was rejected by the Shapiro-Wilk test for a given spatial frequency pair.

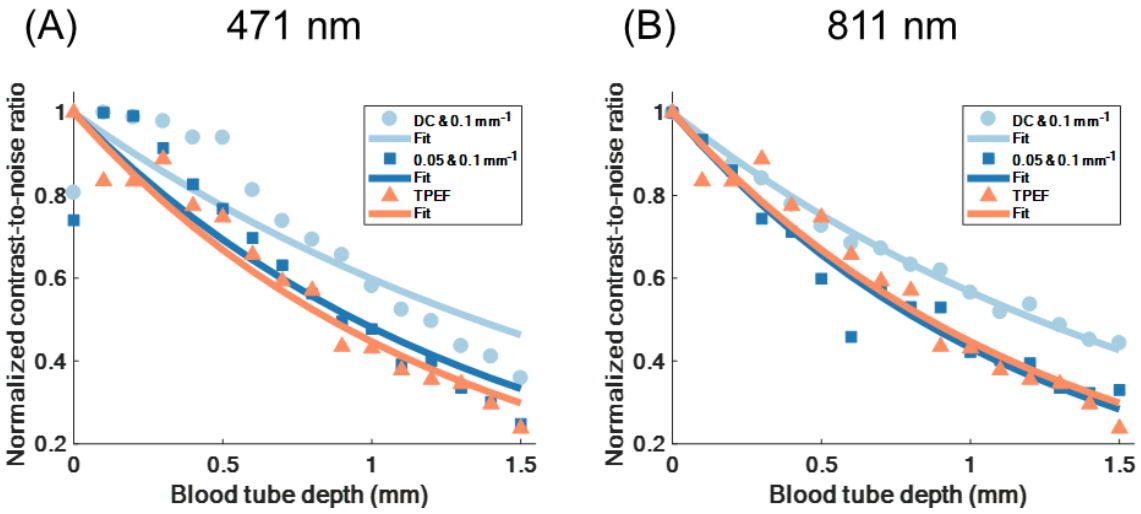

Figure S3-10: Plots of normalized contrast-to-noise ratio (CNR) versus blood tube depth beneath the surface of a liquid phantom that mimicked average Py230 tumor OPs (μ_a = 0.046 mm^{-1}, μ'_s = 0.71 mm^{-1}). The orange triangle (▲) data points represent two-photon imaging of Evans Blue dye mixed with bovine blood in the capillary tube (TPEF Ex/Em 1050/680 nm). The blue circle (●) and square (■) data points represent the different SFDI CNR vs depth curves based on hemoglobin absorption contrast at (A) 471 nm and (B) 811 nm for different pairs of spatial frequencies, demonstrating experimental repeatability at other wavelengths. The following are the exponential decay constants (α) with their 95% confidence bounds, and goodness-of-fit (R2) values for [DC & 0.1 mm^{-1}, 0.05 & 0.1 mm^{-1}, TPEF], respectively: (A) α = [0.51, 0.73, 0.81]/mm, 95% confidence bounds on α = [(0.41, 0.62), (0.61, 0.86), (0.73, 0.88)]/mm, R^2 = [0.81, 0.85, 0.95]. (B) α = [0.57, 0.84, 0.81]/mm, 95% confidence bounds = [(0.55, 0.59), (0.77, 0.91), (0.73, 0.88)]/mm, R^2 = [0.99, 0.95, 0.95].

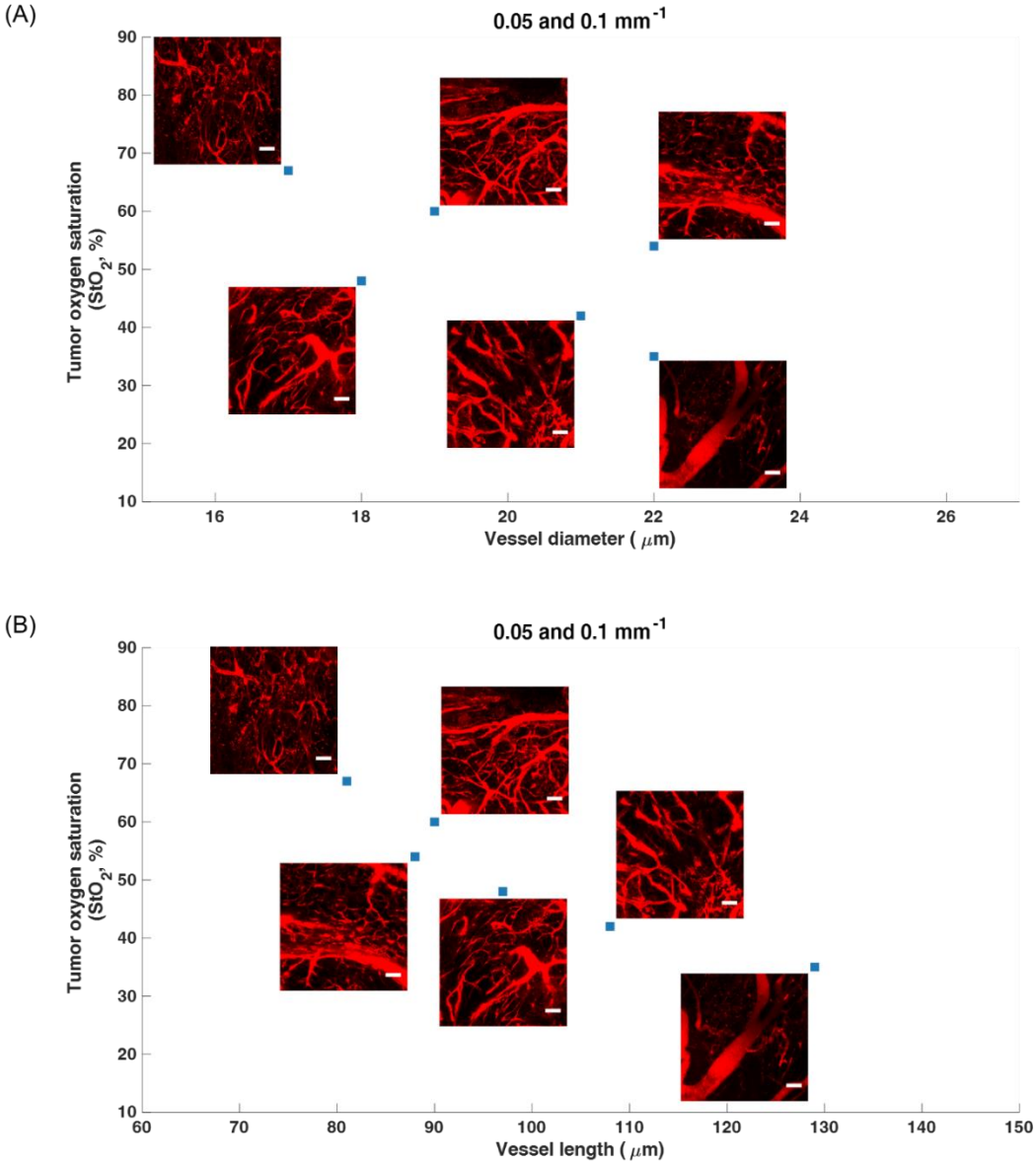

Figure S3-11: Representative MPM microvascular images from each mouse (n = 6) plotted next to their respective multiscale vascular parameter data points to visualize microvascular morphology in the context of extracted metrics. (A) Plot of average tumor oxygen saturation (StO_2, %) versus average vessel diameter (µm) for the spatial frequency pair 0.05 and 0.1 mm^{-1}. (B) Plot of average tumor oxygen saturation (StO_2, %) versus average vessel length (µm) for the spatial frequency pair 0.05 and 0.1 mm^{-1}. White scale bars = 100 µm.

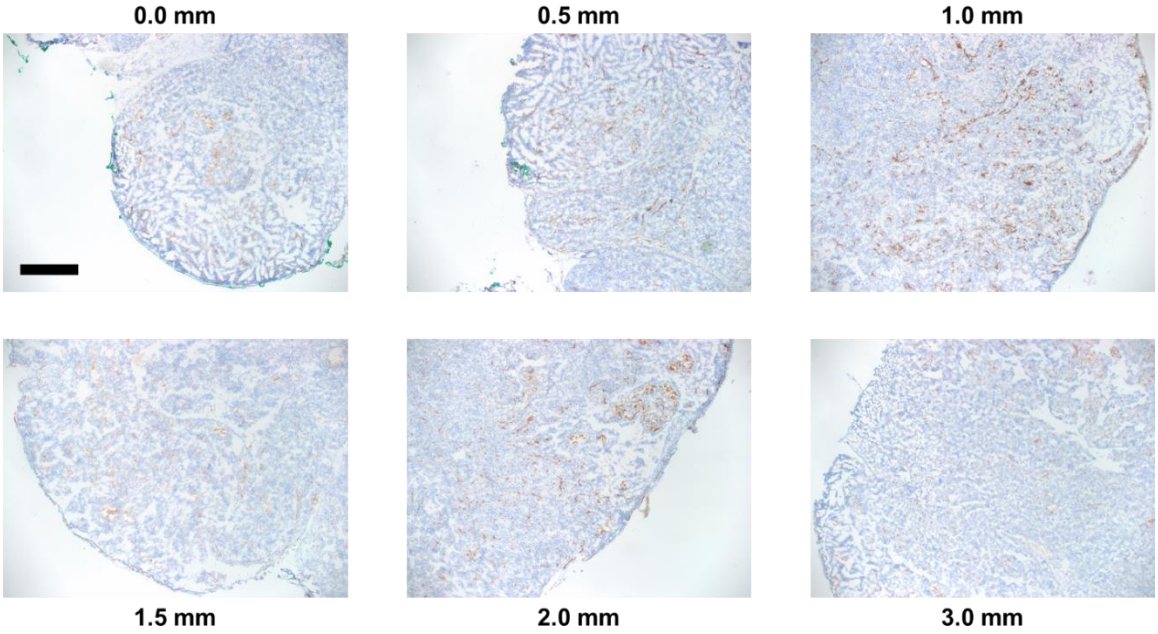
0.0 mm
0.5 mm
1.0 mm
1.5 mm
2.0 mm
3.0 mm

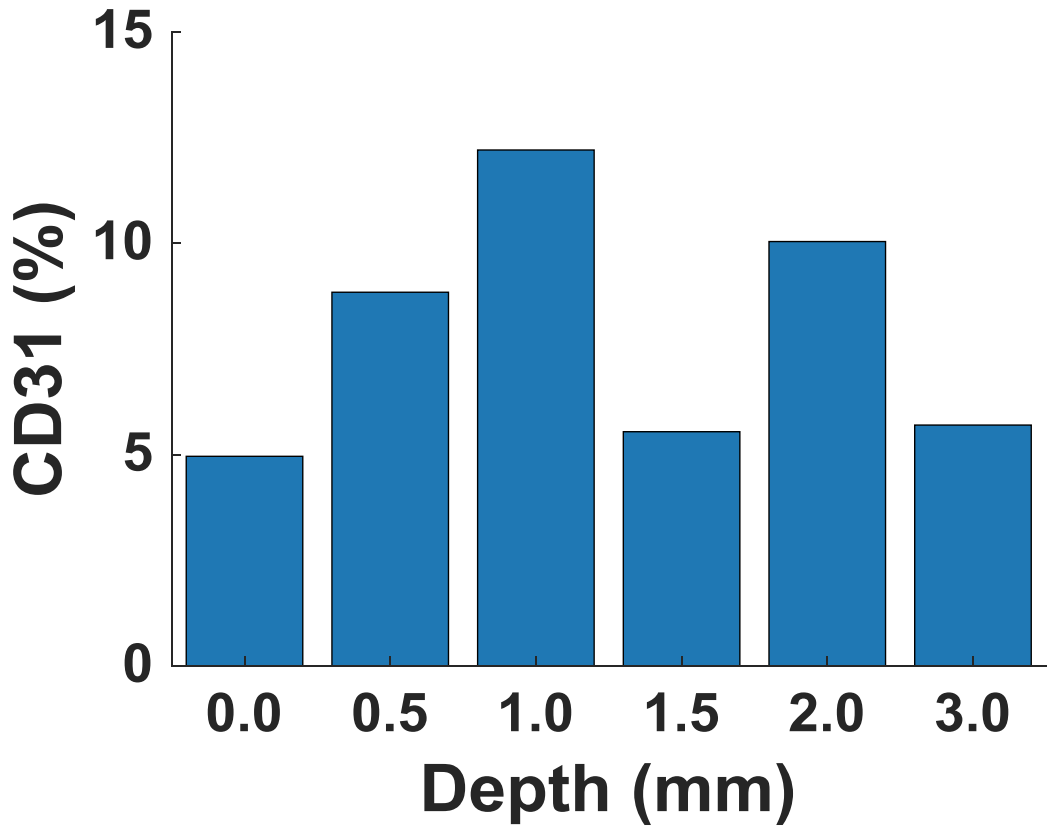
CD31 (%)
15
10
5
0
0.0
0.5
1.0
1.5
2.0
3.0
Depth (mm)

Figure S3-12: Heterogeneity in tumor vascular content as a function of depth. The images show representative regions of hematoxylin (blue) and CD31 (brown) stained tissue sections taken from a single Py230 tumor at different depths. The slides were sent to the Brigham and Women's Hospital Pathology Core (Boston, MA) for hematoxylin (H) and CD31 staining, after which the stained tissue sections were imaged with an upright bright-field microscope outfitted with a color camera and a 4x objective (Nikon Eclipse 50i microscope and SPOT camera, Micro Video Instruments, Avon, MA). For each section (i.e., depth), images were stitched together using a stitching method in FIJI[85]. The stitched images were then deconvolved into H and CD31 channels using a color deconvolution method in FIJI[110]. CD31 was then quantified by taking the total number of CD31 pixels and dividing by the sum of CD31 plus H pixels using the deconvolved images. The bar plot shows the resultant CD31 analysis. Since vascular content is not homogeneous with depth throughout the tumor, this emphasizes the importance of matching sampling volumes between the diffuse and nonlinear imaging regimes to establish robust multiscale correlations across tumor microvascular structure and function. Importantly, this reinforces the need for SFDI to match MPM in depth sensitivity, otherwise SFDI measurements would be volume averaging hemoglobin information from vasculature beyond the depth limitation of MPM and undermine any elucidated multiscale correlations. Scale bar is 500 μm.

3.7.2 Optical sampling depth in the spatial frequency domain

The material in Section 3.7.2 supported the work in Chapter 3 and are based off of work published in the Journal of Biomedical Optics[87] with the following contributing authors:

Carole K. Hayakawa,[a,b] Kavon Karrobi,[c] Vivian Pera,[c] Darren Roblyer,[c] and Vasan Venugopalan[a,b]

[a] Department of Chemical Engineering and Materials Science, University of California at Irvine, Irvine, California, United States

[b] Beckman Laser Institute, Laser Microbeam and Medical Program, University of California at Irvine, Irvine, California, United States

[c] Department of Biomedical Engineering, Boston University, Boston, Massachusetts, United States

Knowledge of tissue depths sampled by SFDI is important for understanding and contextualizing measurements of layered and heterogeneous tissue, and is therefore relevant to nearly all clinical and preclinical applications of SFDI. Importantly, DNI, in which SFDI is combined with the optical sectioning technique MPM, would benefit from knowledge of SFDI photon sampling depth to ensure data from each modality is sampling similar tissue volumes.

To this end, Dr. Hayakawa and Dr. Venugopalan from the University of California at Irvine helped to develop a method to determine optical sampling depth statistics for SFDI measurements using Monte Carlo (MC) simulations. We then performed a series of experimental SFDI measurements on fabricated phantoms to validate the simulated results. These measurements were taken in a two-layer phantom designed to determine the optical sampling depth as a function of spatial frequency. The two-layer phantom was housed in a container with (L × W × H) dimensions of 7.2 cm × 10.8 cm × 6.1 cm. The top layer of the phantom was a liquid composed of water, nigrosin, and TiO_2 particles with optical properties $\mu'_s / \mu_a = 100$ and $l^* = 1 / (\mu_a + \mu'_s) = 2$ mm at $\lambda = 731$ nm (where l^* is the transport mean-free path). The bottom layer was a highly absorbing solid phantom composed of agar, water, and nigrosin, and occupied a total volume of 350 mL in the container. The top layer thickness d was varied from [0-7.5] × l^*. Figure S3-13 provides a schematic of the setup.

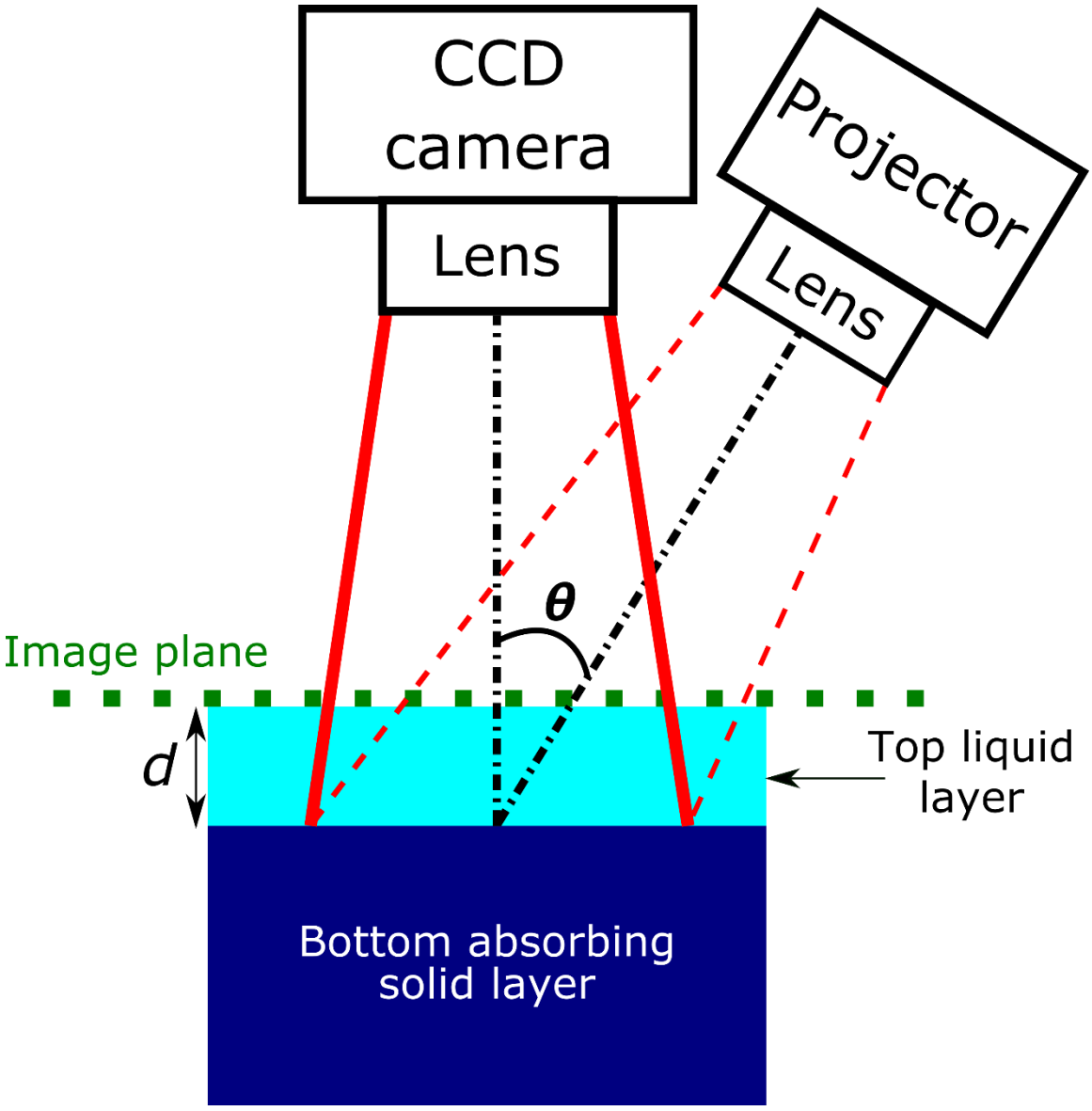

Figure S3-13: Experimental setup and schematic of two-layer phantom with top layer thickness d varying from [0−7.5] × l^* where l^* = 2 mm. Theta (θ) is 15 deg. This experimental setup was used to acquire reflectance as a function of spatial frequency (f_x) and layer thickness d. All measurements were performed at λ = 731 nm.

We used the OxImager RS SFDI system (Modulated Imaging Inc., Irvine, California) to measure the two-layer phantom. The SFDI system utilized crossed linear polarizers in front of the projection and detection lenses to minimize the effect of specular reflection and select for diffuse reflection. The projection field of view (FOV) was 20 cm × 15 cm and directed to the tissue surface at an angle of 15 deg relative to the surface normal. Detection was performed perpendicular to the surface of the phantom with a FOV of 8 cm × 6 cm (effective NA = 0.253). A vertical translation stage was used to support and adjust the height of the container with the two-layer phantom. After taking the first measurement of the highly absorbing solid phantom (i.e., d = 0 mm), incremental amounts of the liquid phantom were added successively with a predetermined volume such that the top liquid layer thickness d above the solid phantom increased by 0.5 mm between each measurement following the d = 0 mm measurement. The micrometer on the translation stage was used to lower the two-layer phantom system by 0.5 mm following each measurement such that the top surface of the two-layer phantom system remained at a constant image plane for all top layer thicknesses measured. This was done to avoid the need for height correction during data processing. All measurements were performed at a wavelength λ = 731 nm with spatial frequencies f_x = [0, 0.0125, 0.025, 0.0375, 0.05, 0.0625, 0.075, 0.0875, 0.1, 0.125, 0.15, 0.175, 0.2, 0.25, 0.3] mm^{-1}. At each spatial frequency (in this case, along one spatial dimension x), raw reflectance images at three different phases (0, $2\pi/3$, and $4\pi/3$ radians) were sequentially projected onto the phantom using a digital micromirror device. The resulting reflected light was imaged with a camera. The images were then demodulated to extract the amplitude envelope for each spatial

frequency measurement using an established amplitude demodulation algorithm[39,40]. A separate reference measurement at the same spatial frequencies was made on a calibration phantom with known optical properties for calibration of the SFDI source intensity and instrument response. This calibration enables the measured reflectance to be converted to absolute reflectance. This is achieved by comparing the measured reflectance from the calibration phantom with its predicted diffuse reflectance from an MC-based forward model using the phantom's known optical properties. The region of interest (ROI) chosen for data analysis was centered in the detection FOV to avoid edge effects and measured 7.5 cm × 2 cm. The reported experimental data are average values taken over the ROI.

The experimental setup consisted of SFDI measurements taken of a two-layer phantom with a highly absorbing bottom layer placed at various depths d that extinguished any photons that propagated to that depth. The resulting measured reflectance was therefore only composed of photons that never reached depths $z > d$, i.e., the photons detected possess trajectories with a maximum $z \leq d$. This was compared to the analogous computational result where only photons that visited a maximum $z \leq d$ and were subsequently detected were tallied and contributed to simulated reflectance measurements up to and including d (termed "$P_{z,max}(z \leq d)$"; please refer to Hayakawa et al.[87] for complete details and derivations).

Figure S3-14 shows the calibrated experimental measurements of diffuse reflectance versus top layer thickness d and plots of $P_{z,max}(z \leq d)$ and their difference. The plots show a subset of the measured f_x values for clarity. The depths d and the spatial frequencies have been normalized to $l^* = 1$ mm. For normalized spatial frequency $f_x l^* = 0$,

the plot rises from 0 and reaches a value of 0.595 for top layer thickness of 7.5 d/l^*. The plot rises monotonically as the top layer thickness increases because increasing numbers of photons fail to be extinguished by the bottom layer and are able to return to the surface to contribute to reflectance. As the spatial frequency increases, the measured diffuse reflectance flattens at a certain depth indicating that spatially modulated light for this frequency does not interrogate the tissue below that depth. For example, for $f_x l^* = 0.3$, the spatially modulated reflectance rises from 0 and rises to 0.05 for top layer thickness of 1.0 d/l^* without further increases for larger top layer thicknesses. The absolute difference between the experimental measurements and the computational predictions ranged between $[-0.012, 0.025]$.

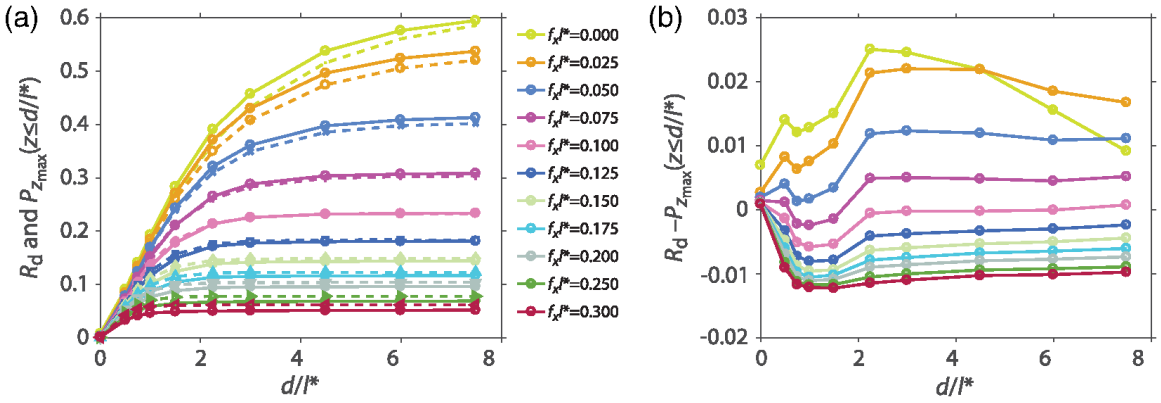

Figure S3-14: (a) Experimentally measured and calibrated R_d (solid lines) and $P_{z,max}(z \le d/l^*)$ from simulation (dashed lines) and (b) their difference.

After experimentally validating the MC predictions, we used the MC method to predict optical sampling depth statistics for SFDI measurements of real tissue. Specifically, the method allows us to determine the fraction (X) of the total measured diffuse reflectance that sampled tissue depths d_X or less for a given spatial frequency. X is calculated by dividing $P_{z,max}(z \leq d_X)$ by the total simulated diffuse reflectance (i.e., the integral over all depths where the contribution of each simulated detected photon is isolated to its maximum visited depth). For example, if a given tissue has a d_{90} = 5 mm for a given f_x, the user is certain that 90% of the measured reflectance at that f_x is restricted to tissue depths ≤ 5 mm, and only 10% of the measured reflectance at that f_x sampled tissue depths > 5 mm. By using the MC method to simulate a range of optical properties and spatial frequencies, a lookup table with general optical properties was generated that can be scaled and interpolated to estimate sampling depths for any arbitrary tissue given knowledge of the optical properties for the tissue of interest. Figure S3-15 provides an example depth statistic plot generated from the lookup table using average Py230 tumor optical properties (μ_a = 0.046 mm^{-1}, μ'_s = 0.71 mm^{-1}).

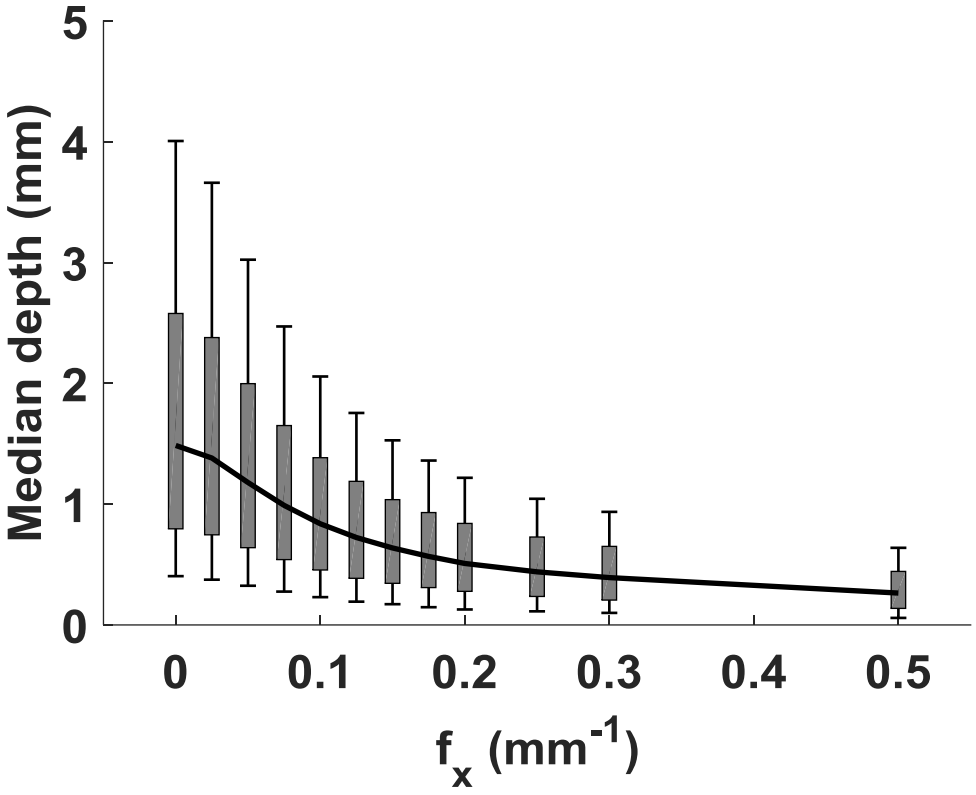

Figure S3-15: Median sampling depth (d_{50}) with [25 to 75]% (gray rectangle) and [10 to 90]% (vertical-capped line) intervals versus f_x for media with optical properties $\mu'_s / \mu_a = 15.4$ and $l^* = 1.3$ mm.

The advantage of this lookup table method is that it dispenses with the need to execute a MC simulation for the specific tissue optical properties in question and enables rapid estimation of SFDI sampling depths. When comparing the lookup table method with the MC method for a range of optical properties and spatial frequencies, the results agree to within 7%, suggesting that the lookup table provides an accurate and convenient method for determining depth predictions.

In conclusion, a MC method was developed to determine SFDI optical sampling depth statistics. We then experimentally validated the sampling depth predictions using SFDI measurements taken on a custom fabricated two-layer phantom system. Excellent agreement was obtained between these measurements and our MC predictions. A non-dimensionalized 2-D lookup table was generated based on the MC method to determine sampling depth statistics for any tissue given knowledge of the absorption and reduced scattering properties of the tissue. Collectively, this work in Section 3.7.2 provides a method and convenient means to determine optical sampling depth for SFDI measurements. Importantly, this work informed the novel depth matching method we developed for DNI in Sections 3.2.3 and 3.3.1 to ensure data from SFDI and MPM were sampling similar tissue volumes.

3.7.3 Optical property uncertainty estimates for spatial frequency domain imaging

The material in Section 3.7.3 supported the work in Chapter 3 and are based off of work published in Biomedical Optics Express[88] with the following contributing authors: Vivian Pera,[a] Kavon Karrobi,[a] Syeda Tabassum,[b] Fei Teng,[b] and Darren Roblyer[a]

[a] Department of Biomedical Engineering, Boston University, Boston, Massachusetts, United States

[b] Department of Electrical and Computer Engineering, Boston University, Boston, Massachusetts, United States

While the work in Section 3.7.2 helped us gain insight into the appropriate selection of SFDI spatial frequencies to match MPM imaging depth in preclinical tumors, we needed to balance this choice with any potential tradeoffs with optical property extraction errors. Our first insight into reconciling both concerns came from using the Cramér-Rao lower bound (CRB) methodology described in Pera et al.[88] to explore the theoretical performance of the SFDI system we used in Chapter 3 as a function of spatial frequency pair choices and sample optical properties. Since the accuracy of the predicted performance with the CRB methodology relies on the diffuse reflectance error model ($\sigma_{Rd}(f_x)$) that is unique to the SFDI instrumentation and operating conditions, we needed to characterize the precision of our SFDI system described in Section 3.2.1. We did this by measuring 16 tissue-simulating phantoms that spanned a range of optical properties. The phantoms were homogeneous silicone blocks with nigrosin and TiO_2 added to control μ_a and μ'_s, respectively. The phantoms ranged in size with (L × W × H) dimensions from (7 cm × 11 cm × 3 cm) to (13 cm × 20 cm × 3 cm). We made 10 measurements of each phantom at each wavelength and spatial frequency. In Table S3-2, we summarize the relevant properties of our SFDI instrument and data acquisition and processing parameters. We converted the acquired data to calibrated diffuse reflectance as described in Section 3.2.1.

Instrument	
Model	OxImager RS (Modulated Imaging, Irvine, CA)
Source	LEDs at 9 wavelengths (470–970 nm) + white light
Detector	CCD camera: 12-bit, 1.4 MP (1392 x 1040 pixels)
Field of view	20 cm x 15 cm (maximum)
Pixel size (at sample)	0.14 mm x 0.14 mm
Data Acquistion Parameters	
Spectral wavelengths	659, 691, 731, 851 nm (4 total)
Spatial frequencies	0, 0.025, 0.05, 0.075, 0.1, 0.15, 0.2, 0.25, 0.3, 0.35, 0.4, 0.45, 0.5 mm^{-1} (13 total)
No. of measurements	10 (per wavelength per frequency)
Data Processing Parameters	
2 x 2 binning	Sum data over 2 x 2 groups of pixels

Table S3-2: SFDI instrument, data acquisition, and data processing parameters.

Figure S3-16(a) shows the range of optical properties spanned by the 16 tissue-simulating phantoms we measured. The phantoms were divided into two groups: 8 in the training set, and 8 in the test set, as shown in Figure S3-16(a), such that the training set spanned the range of optical properties of interest. The diffuse reflectance error model was constructed by averaging the ratio of the standard deviation (σ_{Rd}) to the mean value (at each wavelength and spatial frequency) of the phantoms in the training set. The data in the test set was used to validate the model.

The diffuse reflectance error model for our SFDI system is shown in Figure S3-16(b). We note that the noise as a function of spatial frequency was rather flat, while the mean diffuse reflectance decreased with increasing spatial frequency, as expected. This results in the increasing trends of σ_{Rd} / mean for all four spectral wavelengths, i.e., the SNR worsens with increasing spatial frequency. The differences due to spectral wavelengths are likely caused by the particular properties of the LEDs in our SFDI instrument.

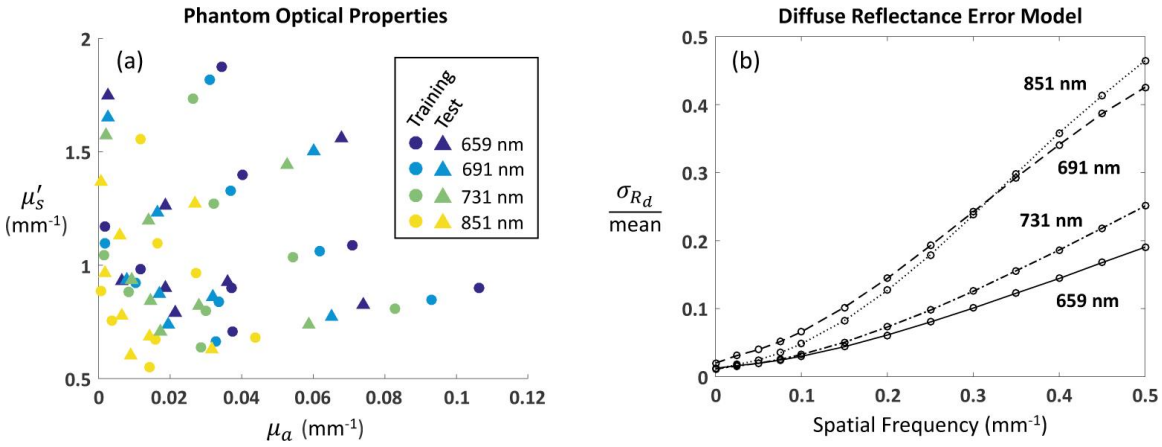

Figure S3-16: (a) Phantom optical properties for training (circles) and test (triangles) sets. (b) Diffuse reflectance error model. Data at 13 spatial frequencies and 4 spectral wavelengths.

We then used our SFDI system's diffuse reflectance error model in conjunction with the CRB methodology to obtain theoretical predictions of our optical property uncertainties for estimating Py230 tumor optical properties (average μ_a = 0.046 mm^{-1}, average μ'_s = 0.71 mm^{-1}) with DC and 0.1 mm^{-1}, and 0.05 and 0.1 mm^{-1} using our SFDI system. As detailed in Section 3.3.1, we showed that the latter spatial frequency pair provided better agreement in depth sensitivity between SFDI and MPM compared to the former spatial frequency pair. Figure S3-17 shows the theoretical predicted uncertainties for each optical property and spatial frequency pair. We note that the CRB methodology predicts that 0.05 and 0.1 mm^{-1} should have approximately 3.4× more uncertainty in μ_a and 1.4× more uncertainty in μ'_s compared to DC and 0.1 mm^{-1} when measuring Py230 tumor optical properties with our SFDI system. As noted in Section 3.3.2, these CRB predicted optical property uncertainties were in agreement with optical property extraction uncertainties that we quantified experimentally in phantoms with optical properties that spanned the range of Py230 tumor optical properties. Importantly, this work helped us to evaluate the tradeoffs between matching MPM imaging depth and optical property extraction errors with SFDI when choosing spatial frequencies to measure preclinical tumors.

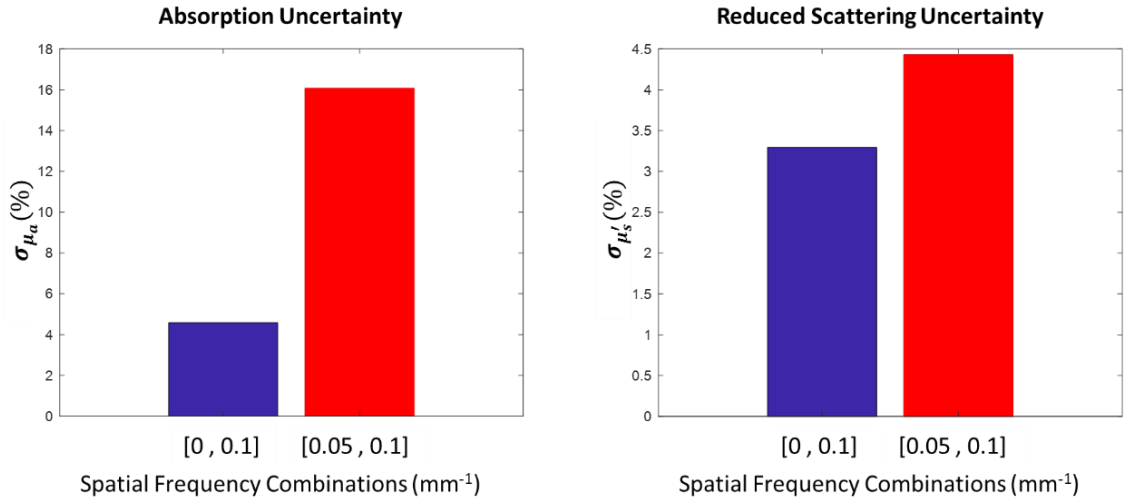

Figure S3-17: Cramér-Rao bounds for absorption and reduced scattering coefficient uncertainties for average Py230 tumor optical properties (μ_a = 0.046 mm^{-1}, μ'_s = 0.71 mm^{-1}). CRBs expressed as percentage of true optical properties.

Chapter 4: Multiscale imaging of in vivo tumor vascular structure and function over space and time with diffuse and nonlinear imaging in preclinical cancer models

Diffuse optical imaging (DOI) techniques have received significant interest as emerging non-invasive functional imaging tools for longitudinal monitoring of patient response to cancer therapies in the clinic. Moreover, DOI has been shown to capture important hemodynamic and metabolic markers of treatment response in cancer patients. Yet, the potential impact, and ultimately adoption of DOI for cancer therapy monitoring in the clinic is limited in part by the lack of knowledge of the cellular, molecular, and biological origins of these clinical observations. We recently developed a new multiscale preclinical imaging method called diffuse and nonlinear imaging (DNI) that combines the DOI technique spatial frequency domain imaging (SFDI) with intravital multiphoton microscopy (MPM) to investigate how DOI signatures relate to the biological underpinnings at the micro scale. However, the proof-of-concept demonstration of DNI was done with two independent devices with limited coregistration and longitudinal measurement capabilities, ultimately limiting the method's throughput and ability to monitor treatment response over time. To address this, we developed the first integrated DNI system with an intrinsically shared imaging coordinate system between SFDI and MPM measurements in preclinical tumors. The DNI system combines a custom SFDI device built into a multiphoton microscope to provide inherent spatial coregistration between multiscale datasets of tumor structure and function. After developing the DNI system, we first characterized its performance characteristics. We then performed longitudinal multiscale measurements of tumor vascular structure and function in breast

cancer xenograft models, and demonstrated that the DNI system can indeed provide inherently coregistered measurements of tumor vascular structure and function over a wide-field, all within a single tumor. We then examined multiscale relationships from the DNI measurements over space and time. Finally, we provide preliminary results demonstrating differences in DNI measurements and multiscale analyses between different treatment regimens and tumor types.

The work in Chapter 4 is to be submitted to a scientific journal with the following contributing authors:

Kavon Karrobi,[a] Anup Tank,[a] Matthew Applegate,[a] Cameron Vergato,[b] David J. Waxman,[b] and Darren Roblyer[a]

[a] Department of Biomedical Engineering, Boston University, Boston, Massachusetts, United States

[b] Department of Biology, Boston University, Boston, Massachusetts, United States

4.1 Introduction

Diffuse optical imaging (DOI) techniques have received significant interest as emerging non-invasive functional imaging tools for longitudinal monitoring of patient response to cancer therapies in the clinic. This is in part due to their ability to provide important label-free metabolic and hemodynamic information related to the in vivo tumor state in a safe, non-invasive, and inexpensive manner[1,2]. A growing number of reports have

successfully used DOI to monitor treatment response in cancer patients, with early hemodynamic and metabolic response markers reported within hours to weeks from the start of treatment[3–5]. For example, several reports have shown that decreases in hemoglobin content, decreases in water, and/or increases in lipid correlate with pathologic complete response in breast cancer patients receiving chemotherapy before surgery (i.e., neoadjuvant chemotherapy, NAC)[6–9]. Similarly, it has been reported that rapid increases in oxygenated hemoglobin within the first day of therapy is predictive of NAC outcomes[10]. While these results are encouraging, the potential impact, and ultimately adoption of DOI for cancer therapy monitoring in the clinic is limited in part by the lack of knowledge of the cellular, molecular, and biological origins of these clinical observations. Knowing how these macro DOI signatures relate to the biological underpinnings at the micro scale is key to providing clinically relevant insights that can be used to manage a cancer patient's treatment strategy with DOI feedback.

To investigate potential multiscale relationships between DOI metrics and the underlying tumor biology in a reliable manner, the following requirements would need to be accomplished: (i) superior interrogation of the same intact and sampled in vivo tissue volumes between DOI and biological metrics, and (ii) capture relevant in vivo biological markers in a noninvasive manner for correlative analysis with DOI measurements taken at the same time and over multiple time-points within a single tumor. The preclinical setting is ideal for testing these ideas as this will require careful control over treatments and imaging, with regular access to tumors. Notably, it will be important to measure the same parameters as clinical DOI techniques to translate potential findings to the clinic and

provide a pathway for adaptive therapy strategies based on diffuse optical monitoring of treatment response.

To address this challenge, we recently developed and validated a new multiscale preclinical imaging method called Diffuse and Nonlinear Imaging (DNI) for the coregistration of tissue-level tumor hemodynamics captured with the wide-field and noncontact DOI technique spatial frequency domain imaging (SFDI), and tumor microvascular architecture imaged with intravital multiphoton microscopy (MPM)[73]. We demonstrated high accuracy and precision in spatial coregistration between SFDI and MPM. Additionally, we showed that the appropriate selection of SFDI spatial frequency pair aided in matching MPM imaging depth, which proved to be useful in elucidating multiscale vascular structure-function relationships in a proof-of-concept study in which we performed DNI measurements in untreated murine mammary tumors through mammary imaging windows (MIWs).

However, there were several limitations in our previous work with respect to the outlined requirements above. A major limitation was having to image with two physically separate devices. This meant that spatial coregistration between the independent SFDI and MPM devices needed to be done in a manual manner with the use of a fiducial maker, which can be prone to day-to-day variability and therefore not a robust spatial coregistration approach for repeated longitudinal DNI measurements in a single tumor. Secondly, two separate devices and manual coregistration limit measurement throughput, and therefore would make it difficult to image multiple tumors with DNI over multiple imaging sessions. This resulted in us being able to only identify multiscale relationships at

a single measurement time point in our previous work. Finally, we conducted DNI measurements in a single tumor model, and thus performing DNI measurements in other tumor models would help to further validate the method.

In this work, we address those issues by developing a fully integrated DNI system, with SFDI and MPM measurements acquired through the same optical detection path. This ensures that both forms of imaging can be performed through an intrinsically shared coordinate system on a single sample stage, providing inherent spatial coregistration between SFDI and MPM datasets. The integrated DNI system also enables improved measurement throughput for longitudinal measurements of tumors. Overall, this DNI system provides the opportunity to explore multiscale relationships between DOI metrics and the underlying tumor biology over space and time in preclinical cancer models.

In the following sections, we first describe how we designed and built the integrated DNI system. We then characterize the performance of the system. We then describe longitudinal imaging with the DNI system in breast cancer xenograft models in mice. We then present methods for analyzing multiscale relationships over space and time from longitudinal DNI measurements. Finally, we explore differences in DNI measurements of different treatments and tumor models.

4.2 Methods

4.2.1 An integrated Diffuse and Nonlinear Imaging (DNI) system

An integrated Diffuse and Nonlinear Imaging (DNI) system was developed by building a spatial frequency domain imaging (SFDI) device into an existing multiphoton

microscopy (MPM) system to perform both forms of imaging on a single sample stage. The SFDI device is a modified version of the openSFDI platform (www.openSFDI.org). The four main components of the SFDI system include: (i) light emitting diode (LED) illumination sources, (ii) a digital micro-mirror device (DMD) used to spatially modulate the illumination field, (iii) an imaging lens to collect reflectance measurements, and (iv) a camera for detection. The SFDI illumination arm, which utilizes the LEDs and DMD, was constructed to one side of the shared sample stage. The SFDI detection arm, which utilizes the imaging lens and camera, was constructed such that it shares the same optical detection path and therefore an intrinsically shared imaging coordinate system with the MPM system. A diagram of the DNI system with SFDI and MPM components labeled is shown schematically in Figure 4-1A, with a rendered layout of the SFDI illumination arm shown in Figure 4-1B.

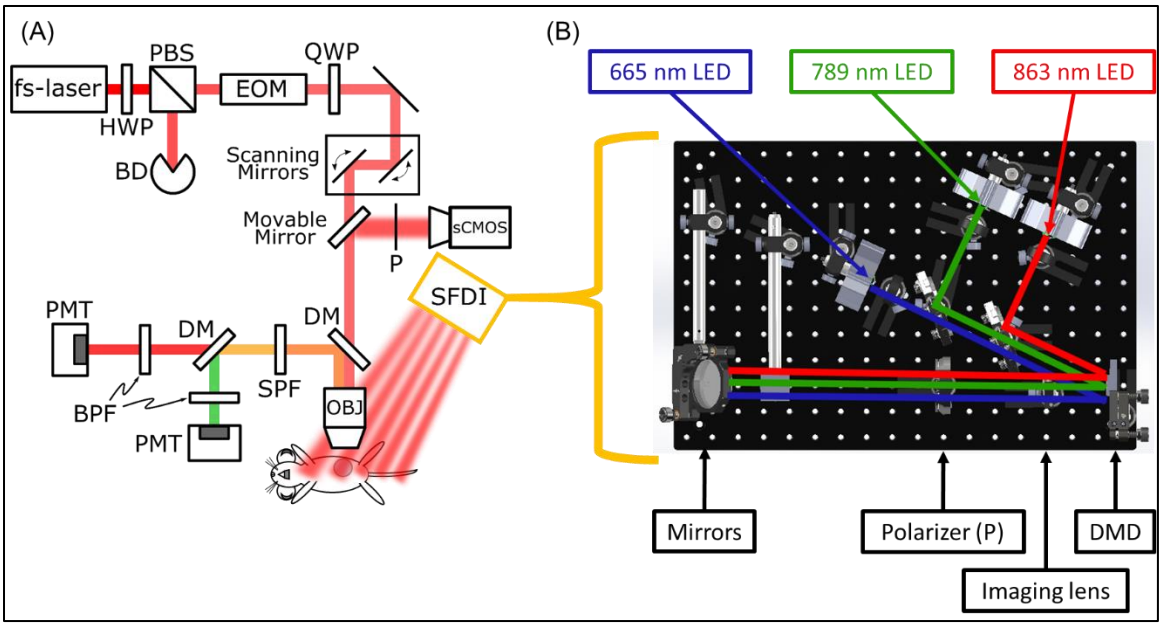

Figure 4-1: The integrated Diffuse and Nonlinear Imaging (DNI) system. (A) Schematic of the DNI system. (B) Bird's-eye view CAD rendering of the SFDI illumination arm of the DNI system with the light paths outlined for the 3 LEDs (measured center wavelengths: 665 nm, 789 nm, and 863 nm). fs-laser: femtosecond-laser (tunable from 680-1300 nm), HWP: half-wave plate, PBS: polarizing beamsplitter, BD: beam dump, EOM: electro-optic modulator (Pockels cell), QWP: quarter-wave plate, DM: dichroic mirror (DM right before OBJ: 725 nm long-pass; DM right before PMTs: 495 nm long-pass), OBJ: objective (SFDI: 2×, 56.3 mm WD, 0.1 NA, air immersion; MPM: 16×, 3 mm WD, 0.8 NA, water immersion), SPF: short-pass filter (750 nm SP), BPF: band-pass filter (440/80 nm and 550/100 nm), PMT: photomultiplier tube, P: linear polarizer, sCMOS: scientific CMOS camera, LED: light emitting diode, DMD: digital micro-mirror device.

The specific components for the SFDI portion of the DNI system were chosen to enable highly sensitive measurements of in vivo hemodynamics in preclinical tumors through imaging windows. The SFDI illumination arm of the DNI system uses 3 high-powered near infrared (NIR) LEDs with center wavelengths of 665 nm, 789 nm, and 863 nm. A spectrometer was used to characterize the center wavelength of each LED, and were subsequently used for all data processing of SFDI measurements taken with the DNI system. These wavelengths were chosen to straddle the isosbestic point of oxyhemoglobin (HbO_2) and deoxyhemoglobin (HHb) absorption at 800 nm to enable high sensitivity to changes in their respective concentrations during longitudinal imaging of preclinical tumors. To minimize LED temperature fluctuations that could accompany longitudinal repeated measurements and result in unstable light output, heatsinks were coupled to each LED to stabilize their temperatures.

SFDI typically utilizes spatially modulated one-dimensional sinusoidal illumination patterns (i.e., spatial frequencies) projected onto a sample of interest (e.g., phantom or tumor) to measure the spatial modulation transfer function (s-MTF) of the sample at every spatial frequency (f_x) and wavelength[40]. The s-MTF measurements can then be fit to a computational model of photon transport to determine the optical properties (i.e., absorption $\mu_a(\lambda)$ and reduced scattering $\mu'_s(\lambda)$) of the sample at every wavelength[40]. Measurements of μ_a at each wavelength can then be used to estimate the molar concentrations of tissue chromophores such as HbO_2 and HHb. To generate spatially modulated one-dimensional sinusoidal illumination patterns at each wavelength, a DMD was used with a 0.45-inch WXGA resolution (LC4500 NIR, Keynote Photonics, Allen,

Texas).

We wanted the SFDI detection arm of the DNI system to meet the following design requirements for in vivo imaging of preclinical tumors through imaging windows: (i) a field of view (FOV) large enough to capture the aperture of the imaging windows (~6.5 mm diameter), and therefore the underlying tumor tissue beneath the imaging windows; (ii) a non-contact working distance (WD) long enough to accommodate the projected spatial frequencies onto the tumors beneath the imaging windows; and (iii) sufficient resolution to capture any heterogeneities in tumor optical properties and/or hemodynamics across the entire aperture of the imaging windows. Accordingly, the imaging lens selected for the SFDI portion of the DNI system is 2× air-immersion microscope objective (TL2X-SAP, Thorlabs, Newton, New Jersey), with a ~56 mm WD, a numerical aperture (NA) of 0.1, and a ~ 7.5 mm × 7.5 mm FOV. A microscope objective was used as the SFDI imaging lens to make use of the MPM system's objective port and enable SFDI and MPM measurements to share the same optical detection path for inherent spatial coregistration between their respective collected datasets. The camera selected for the SFDI portion of the DNI system is a 2048 × 2048, 16-bit, monochromatic Andor scientific CMOS (sCMOS) camera (Zyla 4.2, Oxford Instruments, Oxford, Great Britain), which was mounted at the camera port of the MPM system's microscope body. The camera also has the added benefit of cooling the detector chip, and therefore provides another source of temperature control to maintain stable longitudinal repeated measurements with the SFDI portion of the DNI system.

To minimize the effects of specular reflection from measured samples, the spatial

patterns were projected at an angle with respect to the surface normal, and crossed linear polarizers were used in the SFDI device: (i) one linear polarizer between DMD and the sample stage in the SFDI illumination path, and (ii) another between the microscope objective and camera ports in the SFDI detection path. A modified version of the openSFDI LabVIEW acquisition code was used to operate and acquire images with the SFDI device within the DNI system. The procedures used here for acquiring and processing SFDI measurements to estimate optical properties and hemoglobin concentrations on a pixel-by-pixel basis have been previously described[73].

The MPM portion of the DNI system has been described in detail elsewhere[73]. Briefly, two-photon excited fluorescence (TPEF) was performed with an upright MPM system (Ultima Investigator, Bruker, Billerica, Massachusetts) with a femtosecond laser source tunable from 680 to 1300 nm (Insight DS+, Spectra Physics, Santa Clara, California). The excitation and emission paths were coupled through a 16× long working distance (3 mm) water immersion objective (0.8 NA) (CFl75 LWD 16X W, Nikon, Tokyo, Japan), and separated by a dichroic mirror (725 nm long-pass, Chroma, Bellows Falls, Vermont). The collected emission was split with a dichroic mirror (495 nm long-pass, Chroma) into two detection channels, one with a 480/80 nm bandpass filter (Chroma) and the other with a 550/100 nm bandpass filter (Omega Optical, Inc., Brattleboro, Vermont). Multi-alkali PMTs (R6357, Hamamatsu Photonics, Hamamatsu City, Japan) were used for detection in both channels. Prairie View software (supplied by Bruker) was used to operate and acquire images with the MPM portion of the DNI system. The MPM FOV was 825 × 825 μm^2, with a sampling resolution of 805 nm/pixel.

Finally, the DNI system uses a calibrated linear translation stage driven with a stepper motor (LTS300/M, Thorlabs) to translate samples on the shared sample stage vertically between SFDI and MPM measurements.

4.2.2 Stability of the SFDI device within the DNI system

To ensure that any longitudinal changes in measured optical properties (and therefore hemodynamics) would be due to biological/physiological changes within the measured tumors and not due to system drift, the precision of the SFDI device within the DNI system was evaluated. Repeated measurements of the same optical phantom were conducted over 7 days. On each day: (i) SFDI measurements were repeated approximately every five minutes for one hour; (ii) the measurements were then processed for optical properties; (iii) for each wavelength, the mean optical properties were calculated over the entire FOV (~ 7.5 mm × 7.5 mm) at each measurement time point; (iv) the overall mean and standard deviation of those mean optical properties over the one hour period were calculated for each wavelength; (v) the coefficient variation (c_v) in optical properties for each wavelength was calculated by taking the ratio of the standard deviation to the overall mean. Finally, the c_v in optical properties for each wavelength was calculated across all 7 days. Any percent changes in longitudinal SFDI tumor measurements greater than the c_v (× 100%) can be attributed to biological/physiological changes within the measured tumors.

4.2.3 Accuracy of the SFDI device within the DNI system

The accuracy of the SFDI device within the DNI system was evaluated by comparing it with a commercial SFDI device (OxImager RS SFDI, Modulim, Irvine, California). Tissue-mimicking homogenous optical phantoms (n = 9) were measured with both SFDI devices. The block-shaped phantoms were made of silicone and contained different amounts of nigrosin and titanium dioxide, which are used to tune absorption and scattering, respectively[111]. The optical properties of the measured phantoms were within the following ranges: $0.004 < \mu_a < 0.07$ mm^{-1} and $0.5 < \mu'_s < 2.1$ mm^{-1}. Each phantom was measured three times with each SFDI device, and all the raw data were processed identically. Both devices used measurements of a reference phantom with known optical properties for instrument response calibration. Optical properties were estimated from diffuse reflectance values using a 2-f_x look-up table (LUT) generated from Monte Carlo simulations[45].

Interpolation of μ_a and μ'_s values from the commercial SFDI device was performed to account for differences in wavelengths used between the commercial instrument ([621, 691, 731, 811, 851] nm) and the SFDI device within the DNI system ([665, 789, 863] nm). For μ_a, a cubic spline was used to fit the μ_a spectrum of each phantom measured by the commercial system. Then to estimate μ_a measured by the commercial SFDI device at the DNI SFDI device wavelengths, interpolation was performed using the fit to the commercial system's measured μ_a spectrum of each phantom at the wavelengths used in the SFDI device within the DNI system. For μ'_s, the scattering spectrum of each phantom measured by the commercial SFDI system was fit to the equation

$$\mu_s'(\lambda) = a\left(\frac{\lambda}{\lambda_0}\right)^{-b}, \tag{3.1}$$

where λ represents wavelength, λ_0 was set to 800 nm, *a* is the scattering amplitude, and *b* is the scattering power. Different *a* and *b* values were found for each phantom. To estimate μ'_s measured by the commercial SFDI device at the wavelengths used in the SFDI device within the DNI system, λ_{DNI} was substituted into Equation 3.2 for each wavelength on each phantom.

Comparisons between the devices were made by averaging the pixels within a square (1000 pixels × 1000 pixels) region of interest (ROI) from each optical property map of each phantom measurement. For a given SFDI device, the estimated optical properties of each phantom was calculated by averaging across the three measurements. Likewise, the associated standard deviation was determined by calculating the standard deviation across the three measurements taken on each phantom with each SFDI device.

4.2.4 Breast cancer xenograft models

The HR6 and BT474 breast cancer xenograft models were used for all DNI longitudinal measurements. BT474 breast cancer cells are characterized by the overexpression of the HER2 gene, and were purchased from the American Type Culture Center (ATCC® HTB-20™, Manassas, Virginia). The HR6 cell line is a Herceptin® (trastuzumab) resistant human breast cancer cell line derived in vivo from BT474 xenografts continuously treated with trastuzumab[112], and was generously supplied from the Laboratory of Dr. Carlos Arteaga (Vanderbilt University, Nashville, Tennessee). Both cell lines were grown and expanded at 37°C in a humidified 5% CO_2 atmosphere in MEM

(Richter's modification) media (Catalog No. 10373017, Thermo Fisher Scientific, Waltham, Massachusetts) supplemented with 10% fetal bovine serum and 0.2% phenol red. The HR6 culture conditions were also supplemented with 10 μg/mL trastuzumab to maintain the resistant phenotype in culture. Trastuzumab was a generously supplied from Genentech (South San Francisco, California). Homozygous female J:NU outbred athymic nude mice, approximately 6 weeks old (17-22 g), were purchased from The Jackson Laboratory (Stock No. 007850, Ellsworth, Maine) and were housed in the Boston University Laboratory Animal Care Facility. The female nude mice were implanted subcutaneously with 0.17 mg, 14-day release, 17β-estradiol pellets (Innovative Research of America, Sarasota, Florida) in the mid-scapular region. The next day, nude mice were injected with ~1×10^7 cancer cells (either BT474 or HR6) orthotopically into the inguinal 4th mammary fat pad suspended in a 1:1 (300 μL) mixture of PBS and Matrigel (CB-40234C, Fisher Scientific, Pittsburgh, Pennsylvania) using 1 mL syringes with 26 gauge 5/8 inch needles (BD, Franklin Lakes, New Jersey). Both mouse body weights and tumor volumes were measured every 3 days. Tumor length (L) and width (W) were measured using digital calipers (VWR International, Radnor, Pennsylvania), and tumor volume was calculated as $V_t = (W^2 \times L) / 2$ [112]. During window chamber surgeries and DNI measurements, mice were anesthetized using isoflurane by inhalation (≤ 5% induction, ≤ 2% inhalation, both 1 L/min medical-grade oxygen flow rate) and kept on a heating pad (S-14298B, ULINE, Pleasant Prairie, Wisconsin) to maintain physiological temperature. Ophthalmic ointment was applied to the eyes of the mice to prevent dryness of the eyes during surgeries and imaging sessions. All animal work was reviewed and approved by the

Boston University Institutional Animal Care and Use Committee.

4.2.5 Longitudinal diffuse and nonlinear imaging of HR6 and BT474 tumors through mammary imaging windows

When tumor volumes reached $\geq$150 mm^3, a mammary imaging window (MIW) was surgically implanted over the tumor area by removing the skin covering the tumor and using tissue adhesive to glue the surrounding skin onto the base of the MIW. Figure 4-2A shows an example of an implanted MIW.

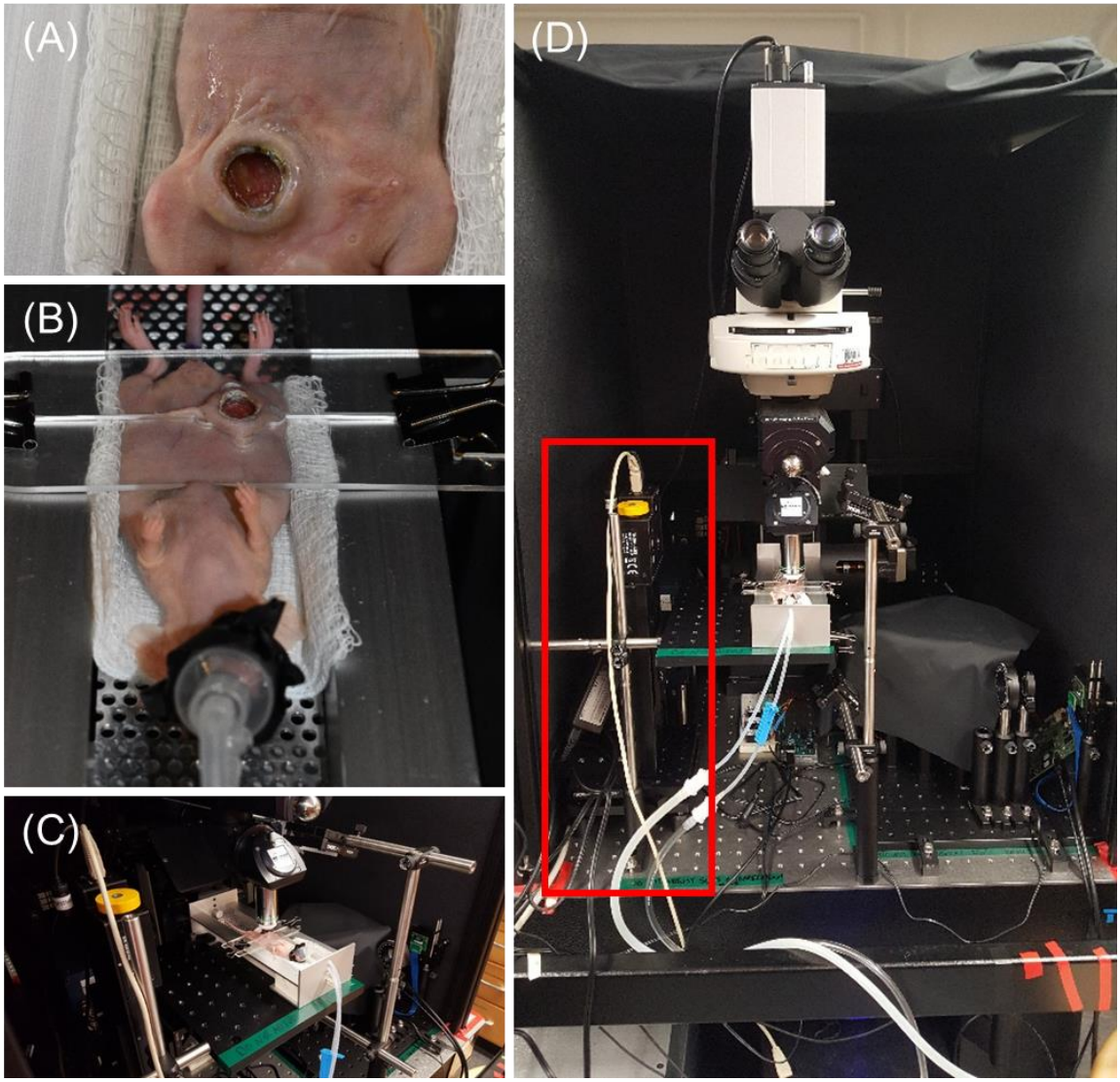

Figure 4-2: (A) Example of an implanted MIW over an exposed mammary tumor. (B) Example of an anesthetized mouse in a supine position within the custom-made holder, immobilized by the stabilizing bars with the round openings securely fitted around the MIW. (C) DNI sample stage supporting the custom-made holder with a mouse's MIW underneath the 16× MPM objective. (D) The calibrated linear translation stage, outlined by the solid red rectangle within the overall image of the DNI system, is vertically aligned and orthogonal to the DNI sample stage.

Each MIW was fabricated from a 12 mm outer diameter, 6.4 mm inner hole diameter stainless steel washer (90965A170, McMaster-Carr, Robbinsville, New Jersey) and an 8 mm diameter circular glass coverslip (64-0701, Warner Instruments, Hamden, Connecticut) under sterile conditions in a biosafety cabinet. The washers and coverslips were autoclaved before using superglue to adhere the 8 mm circular glass coverslips over the 6.4 mm inner hole of the stainless steel washers. After allowing the glue to dry for 15 to 20 minutes, the fabricated MIWs were further sterilized overnight under UV. MIWs were implanted over the exposed tumors such that the side with the glass adhered to the washer faced the tumors. This allowed the other side with the gap between the surface of the washer and the surface of the glass to face outward from the tumor, and therefore provided enough space between the MPM objective and the surface of the glass to achieve a proper working distance for MPM imaging and space for the immersion medium (ultrasound gel, similar refractive index to water, but evaporates slower). Yuk-2e was applied regularly on surrounding skin of the MIWs to discourage chewing. After implanting the MIWs, the mice had at least 2 days of rest after surgery before their first DNI measurement. DNI measurements of the mammary tumors were taken through the MIWs in live anesthetized mice on days -1 (baseline), 2, 5, 8, and 11. For a given breast cancer xenograft model, mice were randomized to receive treatment with either an antiangiogenic agent (DC101) or a control antibody (non-specific mouse IgG, mIgG) at a dose of 40 mg/kg i.p. on days 0, 3, 6, and 9.

During DNI measurements, anesthetized mice were placed in a supine position in a custom-made holder[62,90,113,114] with two stabilizing bars to immobilize the mice for

imaging and reduce motion artifacts due to respiration. The round openings of the stabilizing bars were securely fitted around the MIWs to restrict respiratory motion of the tumors under the MIWs. Care was taken to prevent excessive pressure on the mice to not interfere with breathing. For every DNI measurement, the custom-made holder was positioned on the DNI sample stage such that the heads and tails of the mice were always positioned in the same orientation to maintain rotational consistency between imaging sessions. Figure 4-2B shows an example of an anesthetized mouse in a supine position within the custom-made holder, immobilized by the stabilizing bars with the round openings securely fitted around the MIW.

All experimental and calibration SFDI measurements with the DNI system were performed at the same height/image plane to avoid the need for height correction during SFDI processing. The following wavelengths and spatial frequencies were used for every calibration and experimental SFDI measurement: λ = [665, 789, 863] nm, and f_x = [0, 0.05, 0.1] mm^{-1}. To account for the linear perturbation imposed on the native diffuse reflectances of measured tumors due to the presence of the MIW glass[73], calibration measurements were taken with and without the MIW glass on calibration phantom with known optical properties to treat the effect of the glass as part of the instrument response function, and therefore could be removed with the instrument response function from experimental measurements in processing. Following each experimental SFDI measurement taken through the MIWs, a small fluorescent non-permanent fiducial mark (~1 mm in diameter) was applied to the MIWs, and a planar illumination SFDI measurement at 665 nm was taken. Between SFDI and MPM measurements taken with the DNI system, the objective

lenses were swapped (16× MPM for 2× SFDI), and the calibrated linear translation stage was used to raise the DNI sample stage to meet the smaller working distance requirement of the 16× MPM objective lens. Figure 4-2C shows a picture of the DNI sample stage supporting the custom-made holder with a mouse's MIW underneath the 16× MPM objective. The DNI sample stage is attached in an orthogonal manner to the vertically aligned translation stage, which is outlined by the solid red rectangle in Figure 4-2D.

Before taking MPM scans through the MIWs, the x-y spatial location of the MPM objective lens (which was the same x-y spatial location as the SFDI objective lens) was established as the frame of reference using the MPM system's translation stage. The MPM portion of the DNI system was then used to scan for the location of the fluorescent fiducial mark within the MIWs, and its x-y spatial location relative to the established frame of references was recorded. The recorded x-y spatial locations of the fiducial mark from each DNI measurement day were used to assess any lateral shifts in x and y of the established frame of reference from day to day relative to baseline (day -1). After removing the fiducial mark from the MIWs, 30-50 μL sterile solutions of 5% w/v FITC-Dextran (2 MDa MW, FD2000S, MilliporeSigma, St. Louis, Missouri) in 1× PBS were administered intravenously via retro-orbital injections[115] to fluorescently label the tumor microvasculature. After waiting for ~1 minute for the dye to completely circulate, a UV light source was used to check that the dye reached the tumors beneath the MIWs via fluorescence emission from superficial tumor tissue. Two-photon (2p-ex/em 800/520 nm) scanned 3D stacks of tumor microvascular architecture were then acquired through the MIWs while recording the x-y spatial location of each scan relative to the established frame

of reference. To check that no residual dye was left from previous DNI measurement days, two-photon scans before dye injection were taken on few measurement days and evidence of residual fluorescence (and therefore dye) was not found in either the vascular or interstitial space (data not shown), indicating the dye from the previous measurement days were no longer present in the tumors 3 days later. This gave us confidence that longitudinal DNI (in particular SFDI) measurements would not be affected by the presence of residual dye.

4.2.6 Extraction of tumor microvasculature metrics from vascular images

The vascular image processing methods used to extract structural metrics from MPM images of tumor microvascular architecture (i.e., vessel density, diameter, length, tortuosity) have been described in detail elsewhere[73,116]. Briefly, if any artifacts were present, images were manually masked to exclude identified artifacts and quantification of microvascular metrics was only done within the unmasked regions. Non-uniform background levels were corrected for by removing vessels (diameters ≤ 200 μm) from the background through morphological erosions and dilations with a disk-shaped kernel, followed by the subtraction of the isolated background from the original images. After normalizing the background-corrected images between 0 and 1, vessel intensities were made more uniform through a contrast limited adaptive histogram equalization (CLAHE) process to increase local contrast in the images.

To suppress noise and enhance microvessel edges, an anisotropic diffusion filter was applied to the resultant CLAHE-processed images. Another background correction process was then performed on the diffusion filtered images, followed by multiscale

Hessian filtering to accentuate vessel-like features. To isolate microvessels, local adaptive segmentation was applied to the Hessian-filtered images. The resultant images were then binarized and fed into a Geodesic Active Contour segmentation algorithm, along with their Hessian-filtered counterparts, to produce final processed images with more refined segmentation and binarization of vessels in the foreground.

Using the final processed images, vessel density was calculated by taking the total number of vessel pixels and dividing by the total number of pixels in the original images, which was the same for all original images (1024 × 1024 pixels). To calculate the average vessel dimeter, length, and tortuosity values for each image, the final processed images were skeletonized with identified branch points, where a single vessel was defined as being between two branch points. The diameter of each vessel was determined by multiplying the distance transform of the final processed images by their skeletonized versions to get radius estimates of each vessel in pixels, which were then multiplied by the MPM sampling resolution (0.805 μm/pixel) and a factor of 2 to get diameter estimates of each vessel in microns. The length of each vessel was calculated taking the total number of pixels between the two branch points along the vessel path and multiplying by the MPM sampling resolution. The tortuosity of each vessel was calculated as vessel length divided by the Euclidean distance between the two branch points.

4.2.7 Calculation of spatial and temporal multiscale relationships between tumor vascular structure and function

The established frame of reference from each mouse and each imaging day was used for coregistration between the SFDI and MPM datasets collected with the DNI for

that mouse and imaging day. Each established frame of reference was defined as the DNI origin (0, 0 μm), and the recorded x-y coordinates from the MPM scans were used to find the equivalent locations within the wide-field SFDI hemodynamic maps (HbO_2, HHb, THb and StO_2). At each location, average hemodynamic metrics were determined within a square ROI with the same physical size as an MPM FOV (~ 825 × 825 μm). After pairing hemodynamic metrics with their corresponding microvascular metrics (i.e., vessel density, diameter, length, and tortuosity) for each location within the MIW across either space or time, the multiscale datasets underwent an exploratory data analysis step to identify correlations between tumor microvascular architecture metrics and tissue-level hemodynamics. Correlation matrices were computed for all microvascular and hemodynamic metrics to identify spatial and temporal multiscale pairwise correlations. Correlation analyses were performed with the spatial frequency (f_x) pairs [0, 0.1] mm^{-1} and [0.05, 0.1] mm^{-1}, given that the former has been identified as a f_x pair that minimizes optical property extraction errors[21,88], and the latter has been shown to provide good agreement in depth sensitivity between SFDI and MPM[73].

4.2.8 Statistical analysis

Both the Pearson correlation coefficient (ρ_P) and the Spearman's rank correlation coefficient (ρ_S) were used to evaluate spatial and temporal multiscale correlations between each hemodynamic metric (HbO_2, HHb, THb and StO_2) with each microvascular metric (vessel density, diameter, length, and tortuosity). P values for positive correlations ($\rho > 0$) were determined by testing the alternative hypothesis that the correlations are greater than 0, the null hypothesis being that the correlations are less than or equal to 0. Conversely, P

values for negative correlations ($\rho < 0$) were determined by testing the alternative hypothesis that the correlations are less than 0, the null hypothesis being that the correlations are greater than or equal to 0. P values were adjusted using the Bonferroni (BF, conservative) and the Tukey-Ciminera-Heyse (TCH, less conservative) procedures to control for the type I error rate[107]. Unadjusted (*), TCH-adjusted (†), and BF-adjusted (‡) P values less than 0.05 were deemed significant.

4.3 Results

Sections 4.3.1-4.3.3 describe the integrated DNI system and present results related to its system properties. Sections 4.3.4–4.3.8 then present results to demonstrate the potential for DNI to explore in vivo multiscale relationships between tumor vascular structure and function over space and time in different tumor models and treatment regimens. Because the presented in vivo vascular results come from n = 1 mouse for each tumor type and treatment regimen measured with DNI, the reader is cautioned against drawing any biological conclusions from the presented in vivo vascular results as they merely serve to demonstrate what is possible with DNI.

4.3.1 The integrated DNI system

Figure 4-3 shows a panel of images highlighting the various features of the integrated DNI system. Figure 4-3A is an image of the overall DNI system. In the bottom right of that image is the constructed illumination arm for the SFDI portion of the DNI system, which is displayed from different perspectives in Figures 4-3B and 4-3C. In Figure 4-3B, the illumination paths of each LED are artificially highlighted to show how the

illumination from each LED impinges on the DMD. The 665 nm LED illumination (blue path) transmits through two dichroic mirrors (1st dichroic mirror: 700 nm short-pass; 2nd dichroic mirror: 800 nm short-pass) before illuminating the DMD, while the 789 nm LED illumination (green path) is reflected by the 1st dichroic mirror before transmitting through the 2nd dichroic mirror and illuminating the DMD. The 863 nm LED illumination (red path) is reflected by the 2nd dichroic mirror directly towards the DMD without passing through any additional optics, which may contribute to its higher illumination power (~113 μW) at the DNI sample illumination plane compared to the 789 nm (~41 μW) and 665 nm (~38 μW) LEDs. However, the sCMOS camera attached to the camera port at the head of the microscope body as shown in Figures 4-3A and 4-3D, which serves as the detector for the detection arm of the DNI SFDI device, has a peak quantum efficiency (QE) of ~72% around 600 nm and decreases with increasing wavelength (~20% at 900 nm). Accordingly, the increasing illumination power at the DNI sample plane with increasing wavelength is balanced by the decreasing quantum efficiency with increasing wavelength of the sCMOS camera in the SFDI detection arm of the DNI system.

(E)
(D)
(B)
(C)
(A)

Figure 4-3: (A) An image of the overall DNI system with mirrors outlined that relay the SFDI spatially modulated one-dimensional sinusoidal illumination patterns onto the DNI sample stage. (B) Bird's-eye view of the SFDI illumination arm, with light paths outlined from the 3 LEDs impinging onto the DMD before they are reflected to the first relay mirror. (C) Side view of the SFDI illumination arm with first relay mirror outlined. (D) An image of the SFDI detection arm with the 2× objective located at the microscope objective port to collect sample reflectance measurements, which are relayed by the internal microscope optics to the sCMOS camera attached to the microscope's camera port at the top. The second relay mirror is outlined. (E) A demonstration of how the relay mirrors guide the light to the DNI sample stage.

After the illumination from each LED illuminates the DMD, the spatially modulated one-dimensional sinusoidal illumination patterns imparted by the DMD at each wavelength are then reflected towards the first relay mirror, which is outlined by the orange box in Figures 4-3A and 4-3C. In that same image, the imaging lens (50 mm focal length) that helps to create an image of the patterns onto the DNI sample plane can be seen positioned immediately after the DMD, followed by the first linear polarizer within a rotating mount as the illumination paths head toward the first relay mirror (see Figure 4-1 for reference). The collimating lenses (16 mm focal lengths) in front of each LED illumination source can also be seen in Figure 4-3C.

After the spatially modulated illumination patterns intersect with the first relay mirror, they are then reflected upwards towards the second relay mirror, which is outlined by the yellow box in Figures 4-3A and 4-3D. This second relay mirror is angled to reflect the SFDI illumination patterns onto the DNI sample plane below where a 3D-printed white "mouse" with a 3D-printed red "tumor mass" can be seen lying on a flat phantom positioned on the DNI sample stage below a long working distance (WD ~ 56 mm) air-immersion objective attached at the microscope objective port. This wide-field 2×

objective is used to collect SFDI reflectance measurements from samples positioned below it on the DNI sample stage. These reflectance measurements are then sent to the camera positioned at the camera detection port of the microscope head via the internal relay optics within the microscope body. Positioned between the camera and the objective within the microscope body is a removable second linear polarizer. The first linear polarizer within the rotating mount from the DNI SFDI illumination arm is rotated such that it is cross-polarized with the second linear polarizer that has a fixed orientation within the DNI SFDI detection arm. These crossed linear polarizers help to further minimize the effect of specular reflection from measured samples, in addition to the spatial illumination patterns being projected onto samples on the DNI sample stage at an angle with respect to the surface normal. Figure 4-3E shows how the two relay mirrors work together to guide the illumination (in this case collimated light from a green laser pointer aligned within the optical path of the DNI SFDI illumination arm) onto the 3D-printed sample sitting on the DNI sample stage below the DNI SFDI objective.

To conduct MPM measurements with the DNI system, the 2× SFDI objective lens is swapped with a 16× water-immersion objective lens (3 mm WD), and the calibrated linear translation stage is used to raise the DNI sample stage to meet the smaller WD requirement of the 16× MPM objective lens. Finally, because both the SFDI and MPM portions of the DNI system use the same objective port for their respective objective lenses, this ensures that SFDI and MPM measurements with the DNI system share the same optical detection path for inherent spatial coregistration between their respective collected datasets. This key enabling feature is further highlighted in the following paragraphs and

remaining Results sections through various samples measured with the DNI system.

Figure 4-4 shows images of a fluorescent 1951 USAF resolution test chart (57-894, Edmund Optics, Barrington, New Jersey) captured with the DNI system. The left image was captured with the SFDI portion of the DNI system with the 2× objective and planar (DC or 0 mm^{-1}) illumination at 665 nm. The right image was captured immediately afterwards with the MPM portion of the DNI system after swapping out for the 16× objective and using two-photon excitation at 810 nm to generate fluorescence (peak emission 550 nm) from the resolution test chart (a thin glass slide was placed between the chart and MPM objective to place a water droplet on the glass slide and enable water-immersion imaging). These DNI images of the resolution test chart not only demonstrate how the image of the chart with MPM is spatially coregistered within a wide-field image of the same chart taken with SFDI, but also the relative spatial extent of a single high resolution MPM scanning field within the larger lower resolution SFDI image.

From these images, the line spacing (and therefore the lateral resolution limit) was determined for the SFDI and MPM portions of the DNI system based on the largest group and element numbers observed without distinct contrast in each image, and resulted in 10 μm line spacing (Group 5, Element 5) for SFDI (~4 μm sampling resolution) and 2 μm line spacing (Group 7, Element 6) for MPM (~0.8 μm sampling resolution).

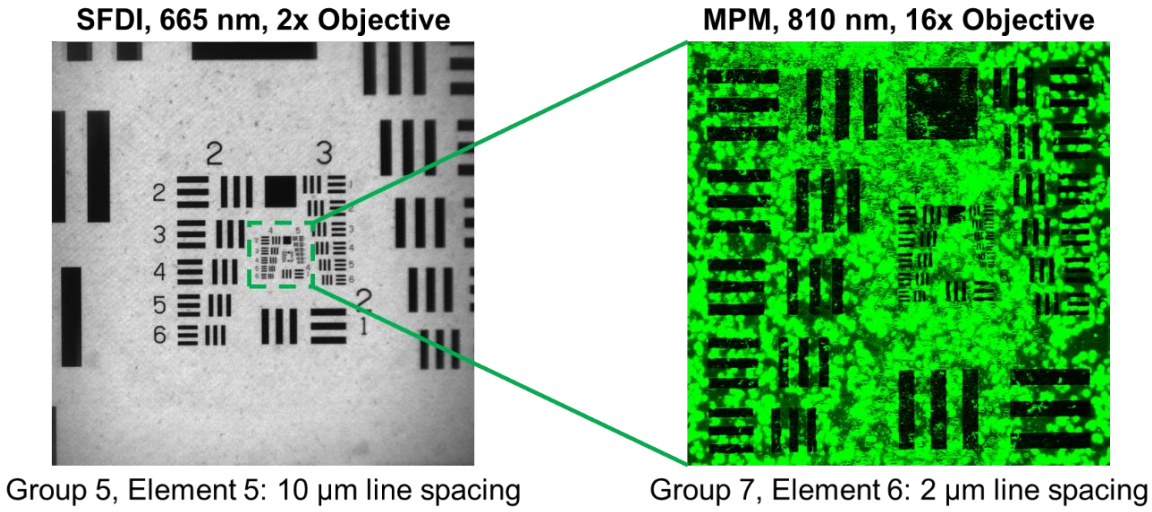

Figure 4-4: DNI imaging length scales. Images of a fluorescent 1951 USAF resolution test chart taken with both the SFDI and MPM portions of the DNI system after switching objectives between the two imaging modes (SFDI: 2× objective; MPM: 16× objective) to demonstrate the relative spatial extents of SFDI and MPM. Wavelengths refer to illumination/excitation wavelength for a given modality. Line spacing was determined by inspecting each modalities image of the resolution test chart, with the approximate resolution limit based on the largest group and element numbers observed without distinct image contrast.

To further highlight the inherent spatial coregistration between SFDI and MPM measurements as a result of the shared detection path within the integrated DNI system, the DNI system was used to image a fabricated sample with properties that could be measured with both SFDI and MPM. Specifically, a 10 mm × 10 mm × 15 mm cube was 3D printed with the letters "BU" etched onto one surface of the cube and filled with a solution of 20% Intralipid® and 0.1 mg/mL Evans Blue dye (E2129, MilliporeSigma, St. Louis, Missouri). The dye has absorption/excitation peaks at 470 nm, 540 nm, and 620 nm, and has a peak fluorescence emission around 680 nm[117,118]. As a result, the solution was a fluorescent diffusive medium, with scattering imparted by the presence of Intralipid®, and absorption and fluorescence imparted by the presence of the dye. Therefore, the sample could be imaged with SFDI and MPM modes of contrast that would also be used to measure in vivo tumor vascular structure and function with the DNI system in preclinical tumor models: namely, absorption (μ_a) with SFDI, and two-photon excited fluorescence (TPEF) with MPM. Figure 4-5 visually shows the results from imaging the fabricated fluorescent and diffuse sample with the DNI system.

As expected the "BU" letters exhibited both strong fluorescence and absorption properties. Also as expected, the μ_a values of the sample are higher at 665 nm than at 863 nm since the dye has little to no absorption past 670 nm[117]. Importantly, the results demonstrate the inherent spatial coregistration between the SFDI and MPM modes of contrast with the DNI system.

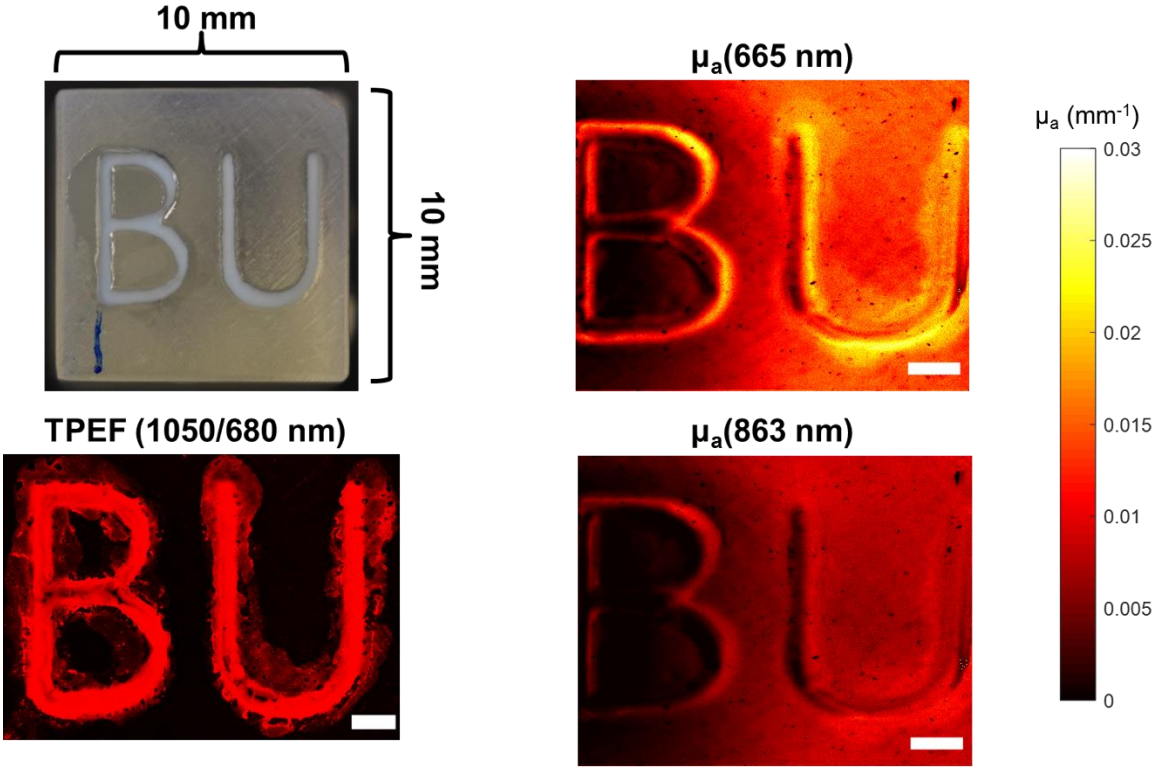

Figure 4-5: Examples of the coregistered modes of contrast with DNI. (Top left) A 3D-printed cube with the letters "BU" etched onto one surface of the cube and filled with a solution of 20% Intralipid® and 0.1 mg/mL Evans Blue dye. The dye has absorption/excitation peaks 470 nm, 540 nm, and 620 nm, and has a peak fluorescence emission at 680 nm[117,118]. (Bottom left) A MPM image of the "BU" letters with two-photon excited fluorescence (TPEF) contrast (2p-ex/em 1050/680 nm). (Top right) A SFDI absorption (μ_a) map of the "BU" letters at 665 nm. (Bottom right) A SFDI μ_a map of the "BU" letters at 863 nm. Given that the dye has minimal absorption efficiency past 670 nm[117], it was expected that the μ_a values at 863 nm would be less than the μ_a values at 665 nm. All scale bars are 1 mm.

Table 4-1 summarizes the overall performance characteristics of the DNI system. The "Biology" column places the listed technical parameters within the context of relevant biological parameters. For example, the modes of contrast that are relevant to the in vivo work described herein are μ_a from SFDI and TPEF from MPM with the DNI system, which are used to assess in vivo tumor vascular structure and function in concert over space and time. However, when taking into account these two modes of contrast with the other modes of contrast afforded by the DNI system (i.e., reduced scattering μ'_s with SFDI, and second harmonic generation with MPM), there are a multitude of multiscale biological parameters that can be monitored with the DNI system in addition to vascular parameters, including tumor metabolism from NADH/FAD autofluorescence via TPEF, and other tumor microenvironment architectural parameters such as collagen via second harmonic generation (SHG) and SFDI scattering parameters.

It is worth making a couple comments related to "Resolution," which in this case refers only to lateral or transverse resolution. With respect to MPM resolution, the resolution test chart results (Figure 4-4) indicated a resolution limit of 2 μm. However, when measuring fluorescent 0.1 μm diameter beads, the practical MPM resolution was found to be approximately 3 μm. Secondly, Table 4-1 lists the measured SFDI resolution as 10 μm, which was the resolution limit measured from the resolution test chart. However, it should be noted that the resolution of any diffuse optical imaging device like SFDI in a highly scattering medium like biological tissue is realistically dictated by the transport mean-free path (l^*) within a sample, which is dictated by the sample's optical properties ($l^* = 1 / [\mu_a + \mu'_s]$). For biological tissue, a typical value of l^* is on the order of 1 mm.

PARAMETERS	SFDI	MPM	BIOLOGY
Modes of Contrast	μ_a , μ'_s	TPEF , SHG	Hemoglobin concentrations Tissue oxygen saturation Vascular architecture NADH/FAD autofluorescence Collagen architecture Scattering parameters (amplitude, slope, γ)
Detection	High QE 16-bit sCMOS camera	Multi-akali PMTs	
FOV	7.5 x 7.5 mm 2048 x 2048 pixels	825 x 825 µm 1024 x 1024 pixels	~ 7 mm diameter window
NA	0.1	0.8	
Resolution: *Theoretical* *Measured*	 4 µm 10 µm	 0.5 µm 3 µm	 Cell diameters ~ 10 µm Vessel diameters > 3 µm
System Magnification	2x	16x	
Illumination Power	64 µW	< 100 mW	
Exposure Times	~ 1 s / λ / f_x / phase	~ 4 s / frame	Mouse repsiratory rate ~ 3 breaths / s
Acquisition Times	~ 30 s 3λ , 3f_x , 3φ	~ 400 s / z-stack	Intravascular half-life 2 MDa dextran: 32-58 mins 10 kDa dextran: 14-16 mins

Table 4-1: Table outlining overall DNI performance characteristics. Resolution refers to transverse/lateral resolution. The measured resolution for MPM was determined by measuring fluorescent beads (0.1 µm diameter). The measured resolution for SFDI was based on SFDI images of a 1951 USAF resolution test chart. However, it should be noted that the resolution of any diffuse optical imaging system like SFDI in a highly scattering medium like biological tissue is realistically dictated by the transport mean-free path (l^*) within a sample, which is dictated by the sample's optical properties. For biological tissue, l^* is typically on the order of 1 mm. μ_a: absorption, μ'_s: reduced scattering, TPEF: two-photon excited fluorescence, SHG: second harmonic generation, NADH/FAD: metabolic co-factors, γ: backscatter, QE: quantum efficiency, sCMOS: scientific CMOS, PMTs: photomultiplier tubes, FOV: field of view, NA: numerical aperture, λ: wavelength, f_x: spatial frequency, φ: spatial phase.

4.3.2 Stability of the SFDI device within the DNI system

Figure 4-6 demonstrates that there is no trend in either μ_a or μ'_s that would indicate drift over time with the DNI SFDI device. For the results shown in Figure 4-6, the average c_v of the μ_a measurements across all wavelengths was 0.003. For μ'_s measurements, the average c_v across all wavelengths was 0.001. The results shown in Figure 4-6 are from a representative 60 minute drift measurement, and similar results were achieved across all 7 days of repeated 60 minute drift measurements. The average c_v values of the μ_a measurements at 665 nm, 789 nm, and 863 nm across all 7 days were 0.003, 0.020, and 0.005, respectively, with overall average c_v of the μ_a measurements across all wavelengths and all 7 days being 0.010. The average c_v values of the μ'_s measurements at 665 nm, 789 nm, and 863 nm across all 7 days were 0.001, 0.003, and 0.001, respectively, with overall average c_v of the μ'_s measurements across all wavelengths and all 7 days being 0.001.

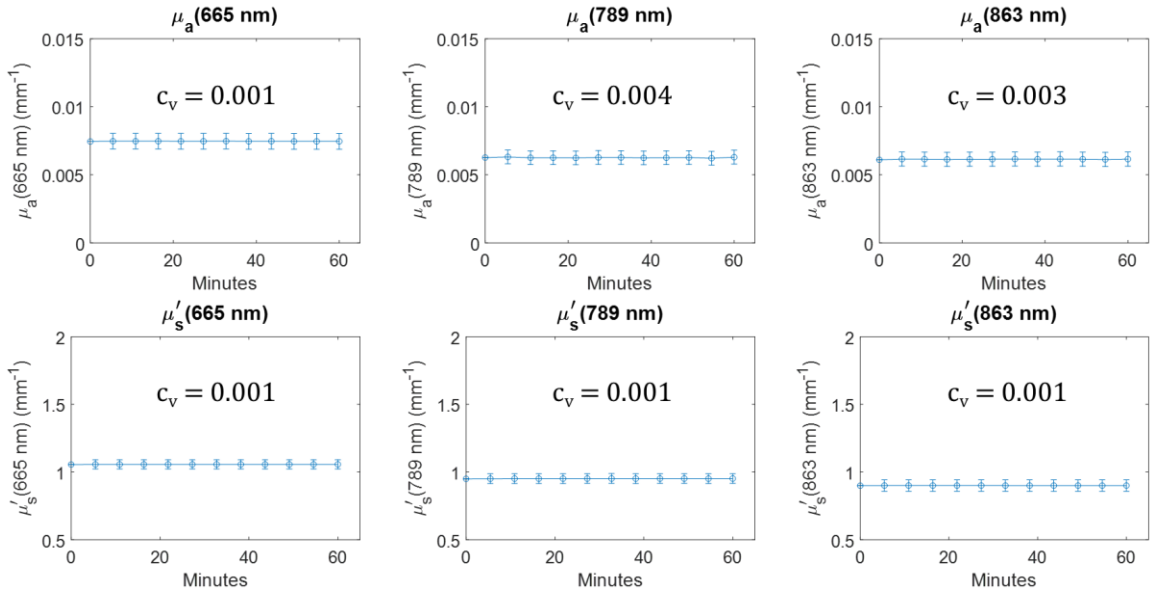

Figure 4-6: Results from a representative 60 minute drift measurement showing the stability of μ_a (top row) and μ'_s (bottom row) measurements, with the coefficient of variation (c_v: ratio of the standard deviation over the mean for the entire drift measurement) in estimated optical properties calculated for each wavelength.

4.3.3 Accuracy of the SFDI device within the DNI system

Figure 4-7 shows the results from comparing estimated optical properties in nine tissue mimicking optical phantoms between the DNI SFDI device and a commercial SFDI device ("Gold standard"). The average difference in μ_a measurements between the DNI SFDI device and the commercial SFDI system was 4% (± 6%). The average difference in μ'_s measurements between the DNI SFDI device and the commercial SFDI system was -1% (± 4%). As evidenced by the error bars being smaller than the makers in the plots shown in Figure 4-7, the DNI SFDI device had little to no variation in optical property measurements. This was also evidenced in Figure 4-6, and is likely due to temperature control achieved at both the illumination (i.e., heat sinks coupled to LEDs) and detection (i.e., camera sensor cooling) arms of the SFDI device within the DNI system.

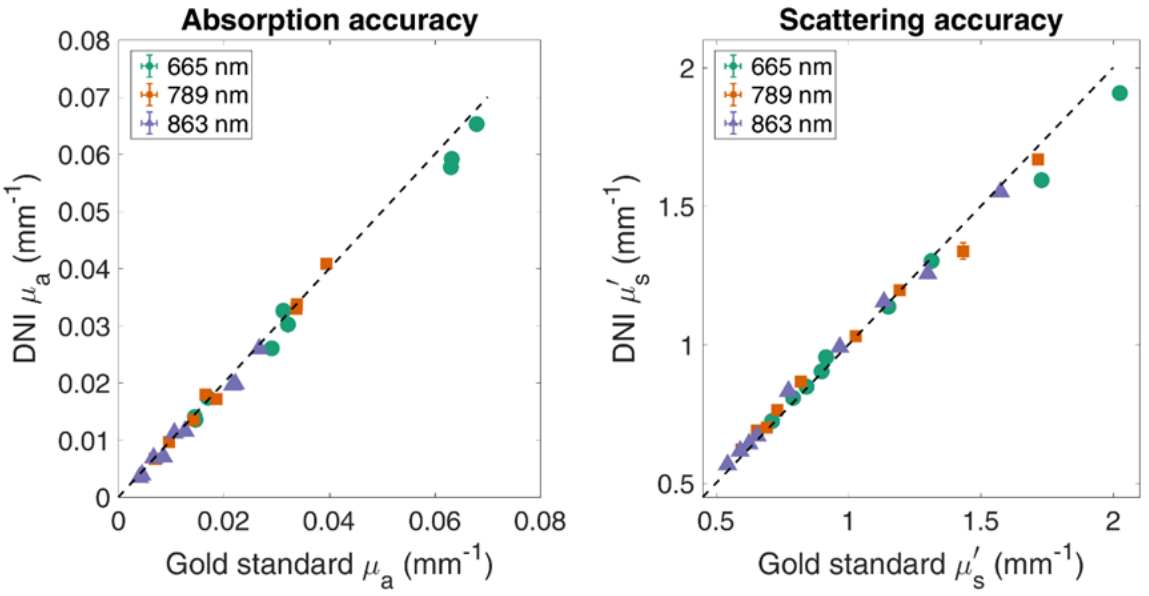

Figure 4-7: Accuracy of the SFDI device within the DNI system compared with a commercial SFDI device ("Gold standard"). Each data points represents the average optical property of a phantom measured three times, with error bars representing the standard deviation across all three measurements (n = 9 phantoms). The error bars are smaller than the markers due to the low measurement variability of the SFDI device within the DNI system, as evidenced in Figure 4-5. The average ± standard deviation difference between the DNI SFDI device and the commercial SFDI system was 4 ± 6% for μ_a, and -1 ± 4% for μ'_s.

4.3.4 DNI enables longitudinal coregistered multiscale measurements of tumor vascular structure and function over a wide-field

Figure 4-8 shows DNI measurements in a single DC101 treated HR6 tumor over multiple days, with tumor vascular structure and function coregistered over a wide-field within the MIW. The top row shows white light images of the tumor underneath the MIW. The second row from the top shows the corresponding tumor oxygen saturation (StO_2) maps derived from 0.05 and 0.1 mm^{-1} SFDI measurements of the tumor acquired through the MIW. The regions outlined by the red dashed boxes (~ 3.5 mm × 3.5 mm) on the StO_2 maps indicate where tiled images of the underlying tumor microvascular architecture were acquired with MPM, which are shown in the third row from the top of Figure 4-8. The bottom row shows spatially coregistered tumor oxygenation and microvascular architecture from the boxed regions overlaid over one another. Because the sampling resolution of the SFDI portion of the DNI device is lower than the sampling resolution of the MPM counterpart, tumor oxygenation measurements from SFDI were interpolated by upsampling in the Fourier domain via zero padding to match the higher resolution microvascular images from MPM before overlaying the two.

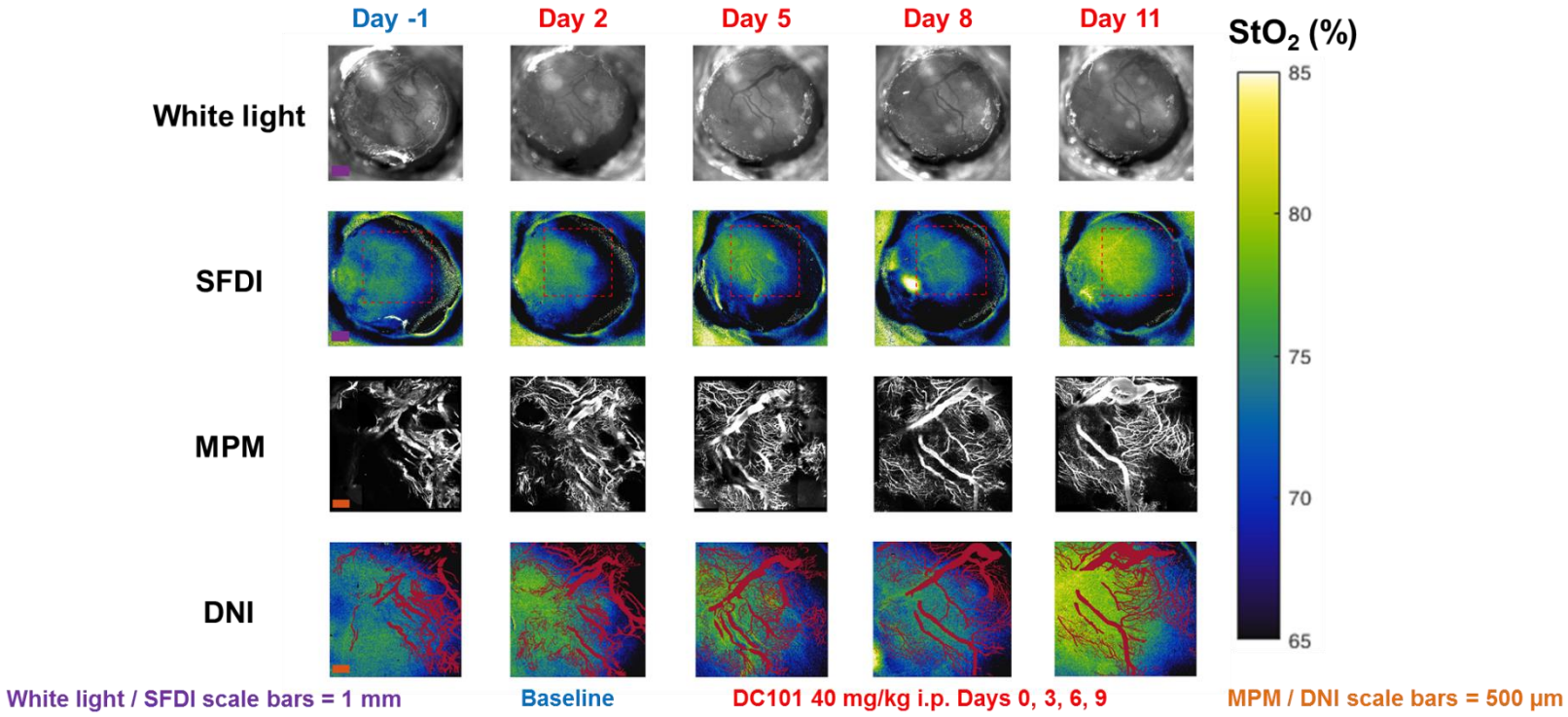
Day -1
Day 2
Day 5
Day 8
Day 11
White light
SFDI
MPM
DNI
StO2 (%)
85
80
75
70
65
White light / SFDI scale bars = 1 mm
Baseline
DC101 40 mg/kg i.p. Days 0, 3, 6, 9
MPM / DNI scale bars = 500 µm

Figure 4-8: An example of heterogeneity in tumor vascular structure and function captured with the DNI system over multiple days within a single HR6 tumor treated with DC101. Order of rows goes downward from "Day" labels. (Row 1) White light images of HR6 tumor acquired through a MIW. Scale bar 1 mm applicable to entire row. (Row 2) Corresponding tumor oxygen saturation (StO_2) maps from SFDI measurements of the HR6 tumor underneath the MIW using 0.05 and 0.1 mm^{-1}. The regions outlined by the red dashed boxes (~ 3.5 × 3.5 mm^2) indicate the locations where vascular images were acquired for Rows 3 and 4. Scale bar 1 mm applicable to entire row. StO_2 (%) color bar scale applies to entire row. (Row 3) Corresponding tumor microvasculature images from MPM scans taken within the regions indicated in Row 2. Scale bar 500 μm applicable to entire row. (Row 4) Wide-field, multiscale views of spatially coregistered tumor oxygenation (function) and microvascular architecture (structure) from regions indicated in Row 2. Scale bar 500 μm applicable to entire row. StO_2 (%) color bar scale applies to entire row.

On any given day, visually there appears to be heterogeneity in tumor oxygenation and vascular architecture over the MIW. For example, on day 11 there appears to be a gradient (higher to lower) in oxygenation going from left to right within the boxed region outlined in the MIW (Day 11 column, DNI row image in Figure 4-8). In that same region on day 11, areas with larger but fewer vessels appear to overlap with high oxygenation areas. Moreover, denser vascular areas with smaller vessels appear to occupy areas where oxygenation transitions from higher to lower values, with avascular areas appearing to overlap with lower oxygenation areas.

Differences in tumor oxygenation and microvascular architecture over the MIW were also observed across the different imaging days. In particular, when looking at the bottom row of overlaid images in Figure 4-8, on day -1 (baseline, i.e., before the start of DC101 treatment) the avascular area on the left half overlaps with higher oxygenation levels compared to the vascularized area on the right half overlapping with lower oxygenation levels. Then on day 2 vasculature begins to grow into the areas of higher oxygenation, with those areas being completely filled with vasculature on day 5 with

similar oxygenation levels as day 2. However, decreases in oxygenation in those areas were observed on day 8. The vasculature in those areas on day 8 began to also show signs of decreased density, which became more pronounced on day 11 when those areas rebounded to higher oxygenation levels.

4.3.5 Spatial multiscale correlations between tumor vascular structure and function

Figure 4-9 demonstrates a method to analyze for any possible spatial multiscale correlations between the tumor microvascular architecture and the corresponding oxygenation measurement over the same vascular field, using DNI measurements from a single mouse and imaging day as an example. The method starts by dividing the wide-field DNI image (vascular structure and function) into equal sized tiles (e.g., 4x4, 8x8, 16x6), as shown in the top row of Figure 4-9. Microvascular metrics can then be extracted from each tile. In this example, vessel density is calculated for each tile. These values can be represented as a heat map of vessel density values for each tile over the entire DNI field, as shown in the second row from the top in Figure 4-9. In a similar manner, the corresponding tumor oxygen saturation measurement over the same DNI filed can be divided up into the same sized tiles and an average StO_2 value can be calculated for each tile, shown as heat maps in the third row from the top in Figure 4-9. When comparing the second (vessel density heat maps) and third (StO_2 heat maps) rows from the top in Figure 4-9, we begin to visually observe a possible inverse spatial relationship between vessel density and tumor oxygen saturation over a wide-field for this particular tumor (DC101 treated HR6 tumor) and imaging day (day 8). This observation is further confirmed when plotting tumor oxygen saturation versus vessel density for each tile (bottom row in Figure

4-9), and finding that indeed there is a negative spatial correlation between StO_2 and vessel density across the wide-field. It is of note that spatial heterogeneity captured with DNI at two different imaging length scales (SFDI macro vs MPM micro) can be correlated with one another. Likewise, this suggests that spatial heterogeneity in one domain (structure or function) may be reflected in the other domain, and vice-versa. Finally, it is worth noting that as the spatial divisions became finer, the negative spatial correlation between StO_2 and vessel density became weaker (slope became less negative) for this particular tumor and imaging day.

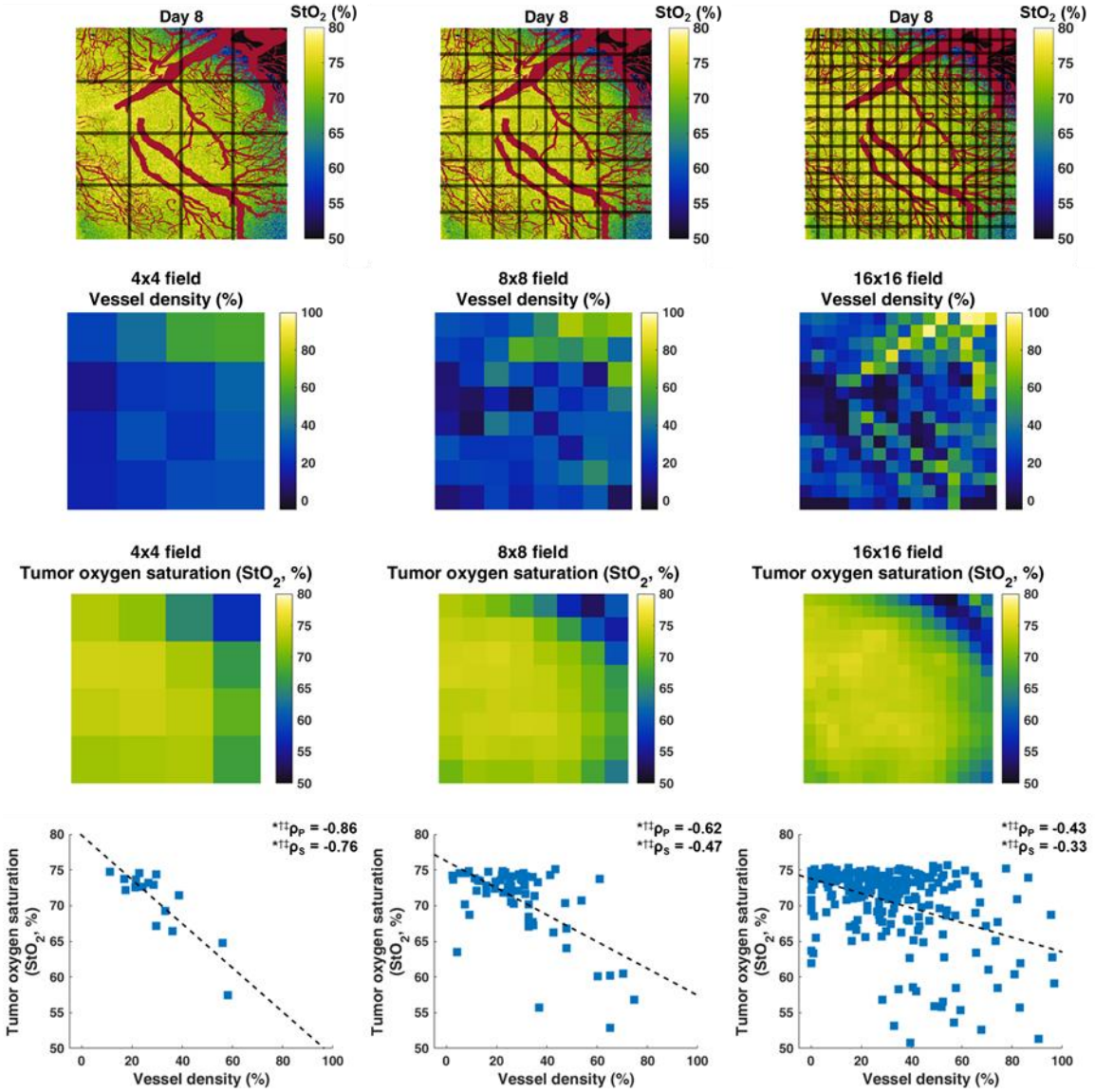

Figure 4-9: An analysis of spatial multiscale relationships between tumor vasculature structure and function in a HR6 tumor treated with DC101 from a single measurement day. (Top row) A wide-field DNI measurement of tumor vascular structure and function divided into various tiles/spatial divisions (4x4, 8x8, and 16x16). (2nd row from the top) Vessel density (%) heat map representations of the various spatial divisions, where each tile is represented by its calculated vessel density value. (3rd row from the top) Tumor oxygen saturation (StO_2, %) heat map representations of the same various spatial divisions, where each tile is represented by its average StO_2 value. (Bottom row) Spatial correlation plots of StO_2 versus vessel density, where each point represents a different tile within the wide-field DNI measurement.

4.3.6 Intratumor heterogeneity

In addition to observing heterogeneity in tumor vascular structure and function with DNI over space, we also observed that trends in tumor vascular structure and function over time can differ from one localized area to another across the wide-field. An example of this is shown in Figure 4-10 with two separate locations within a single tumor (DC101 treated HR6 tumor) over the wide-field DNI measurements. Representative DNI vascular structure-function images from each imaging day are shown for each location, along with tumor oxygen saturation (StO_2, %) distributions for each location across the different imaging days.

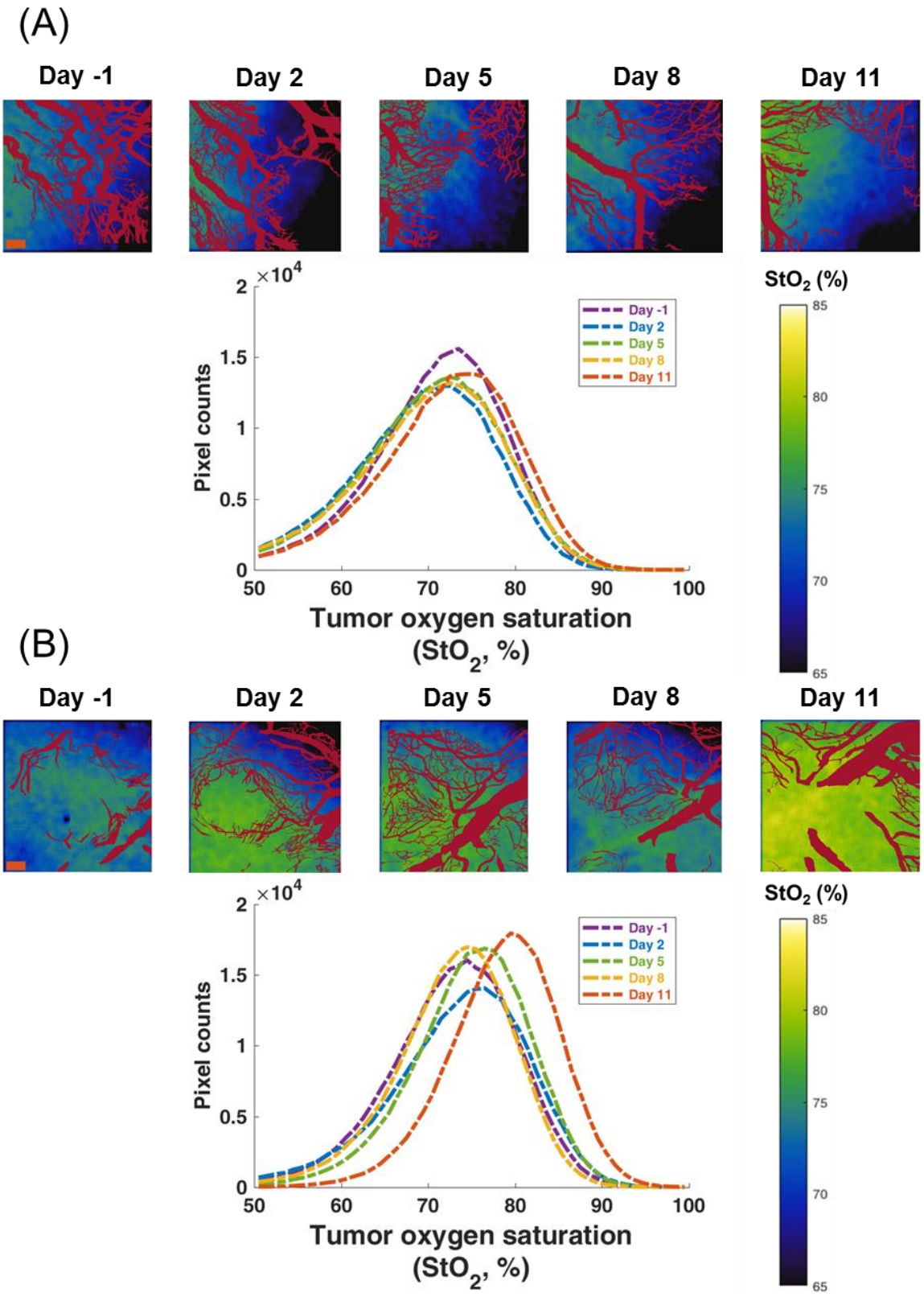
(A)
Day -1
Day 2
Day 5
Day 8
Day 11
$\times 10^4$
Pixel counts
Tumor oxygen saturation
(StO_2, %)
StO_2 (%)
(B)
Day -1
Day 2
Day 5
Day 8
Day 11
$\times 10^4$
Pixel counts
Tumor oxygen saturation
(StO_2, %)
StO_2 (%)

Figure 4-10: Changes in tumor vascular structure and function over time differ across the MIW. (A) and (B) are examples of different locations from a DC101 treated HR6 tumor with differing structural and functional dynamics over time. Scale bars are 250 μm.

Differences in microvascular architectural changes over time were observed between the two locations. Likewise, changes in StO_2 over time were observed to also be different between the two locations. However, irrespective of these temporal differences between different locations, the question is whether any temporal relationships exist between their respective tumor vascular structural and functional changes. For example, the location in Figure 4-10A appears to experience changes in the number and sizes of tumor vessels over time, which is possibly related to shifts in StO_2 in that same area. The location in figure 4-10B appears to experience greater changes in vascular content over time compared to the other location, which is possibly reflected in the larger StO_2 shifts in this location compared to the other location. We investigate the possibility of temporal multiscale relationships in the next section. Specifically, we explore whether changes from baseline (day -1) in these metrics correlate with one another as a surrogate for temporal relationships between tumor vascular structure and function. It has been reported that hemodynamic changes from baseline can be predictive of treatment outcomes[10].

4.3.7 Temporal multiscale correlations between tumor vascular structure and function

Tumor vascular structure and function were tracked in 4 different MPM regions-of-interests (ROIs) in a DC101 treated HR6 tumor across the 5 days of imaging (day -1, 2, 5, 8, and 11). For each ROI, mean hemodynamic metrics (HbO_2, HHb, THb, and StO_2) and mean microvascular metrics (vessel density, diameter, length, and tortuosity) were

calculated for each day. For each MPM ROI, the mean baseline (day -1) value was subtracted from the mean values of all imaging days to calculate absolute changes (Δ) from baseline for each metric. These Δ metrics were used to evaluate multiscale correlations using both the Pearson correlation coefficient (ρ_P) and Spearman's rank correlation coefficient (ρ_S) between each Δ hemodynamic metric (ΔHbO_2, ΔHHb, ΔTHb and ΔStO_2) with each Δ microvascular metric (Δ[vessel density], Δ[diameter], Δ[length], and Δ[tortuosity]). This resulted in 16 multiscale correlations being evaluated simultaneously for a given correlation test. Table S4-1 summarizes our overall findings. There were 8 identified Pearson correlations with unadjusted P values less than 0.05. 7 out of the 8 Pearson correlations were also identified with Spearman with unadjusted P values less than 0.05. 4 out of the 8 Pearson correlations had TCH adjusted P values less than 0.05. 3 out of the 7 Spearman correlations had TCH adjusted P values less than 0.05. No Pearson correlations were deemed significant at a significance level of 0.05 when adjusting P values with the Bonferroni (BF) procedure. However, 2 out of the 7 Spearman correlations had BF adjusted P values less than 0.05.

Figures 4-11A and 4-11B demonstrate correlations between changes in tumor oxygen saturation (ΔStO_2) versus changes in vessel diameter and length, respectively (4 ROIs over 5 days = 20 data points per correlation). A strong negative correlation was observed between ΔStO_2 and Δ[vessel diameter] ($\rho_P = -0.43$, *P = 0.029 | $\rho_S = -0.60$, *†‡P = 0.002). Conversely, a strong positive correlation was observed between ΔStO_2 and Δ[vessel length] ($\rho_P = 0.54$, *†P = 0.007 | $\rho_S = 0.57$, *†P = 0.004).

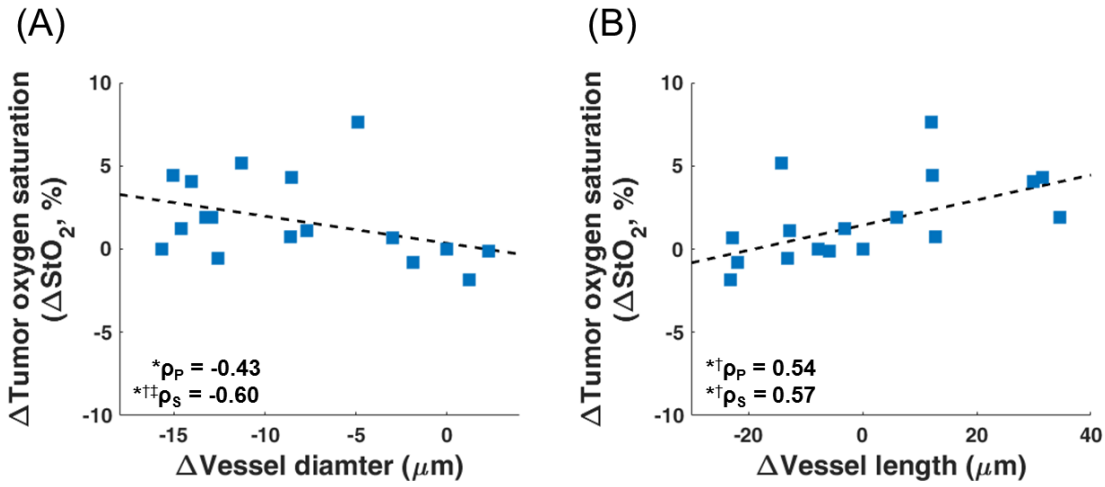

Figure 4-11: Temporal multiscale relationships between changes in tumor vasculature structure and function from baseline (Day -1) in a HR6 tumor treated with DC101. Each point in the plots represents multiscale data from a tumor region in the MIW equivalent in size to a MPM FOV (~825 × 825 µm). Each axis, and thus each data point, represents changes from baseline within a given region extracted from their respective imaging modality and over the same region (SFDI: ΔStO2; MPM: Δ[Vessel diameter] and Δ[Vessel length]). The data comes from 4 different MPM ROIs tracked over 5 days within a single tumor (n = 20 data points per correlation plot). The lines represent the lines of best fit to the data in each plot. The Pearson's ρ (ρ_P) and Spearman's ρ (ρ_S) are reported for each plot. *Denotes unadjusted P < 0.05, †denotes Tukey-Ciminera-Heyse (TCH) adjusted P < 0.05, and ‡denotes Bonferroni (BF) adjusted P < 0.05.

4.3.8 Treatment and model differences

We looked to see if the correlations shown in Figure 4-11 for a HR6 tumor treated with DC101 would be the same in a HR6 tumor treated with a control antibody (mIgG). Figures 4-12A and 4-12B demonstrate a lack of significant correlations between changes in tumor oxygen saturation (ΔStO_2) versus changes in vessel diameter and length, respectively (4 ROIs over 5 days = 20 data points per correlation). A weak positive correlation was observed between ΔStO_2 and Δ[vessel diameter] ($\rho_P = 0.05$, $P = 0.409$ | $\rho_S = 0.14$, $P = 0.279$). Conversely, a weak negative correlation was observed between ΔStO_2 and Δ[vessel length] ($\rho_P = -0.18$, $P = 0.227$ | $\rho_S = -0.09$, $P = 0.359$).

We also looked to see if the correlations shown in Figure 4-11 could be found in a BT474 tumor treated with DC101 (4 ROIs over 5 days = 20 data points per correlation). A weak positive correlation was observed between ΔStO_2 and Δ[vessel diameter] ($\rho_P = 0.11$, $P = 0.321$ | $\rho_S = 0.08$, $P = 0.373$), as shown in Figure 4-12C. However, a strong negative correlation was observed between ΔStO_2 and Δ[vessel length] ($\rho_P = -0.51$, $*^{\dagger}P = 0.011$ | $\rho_S = -0.39$, $*P = 0.044$), as shown in Figure 4-12D.

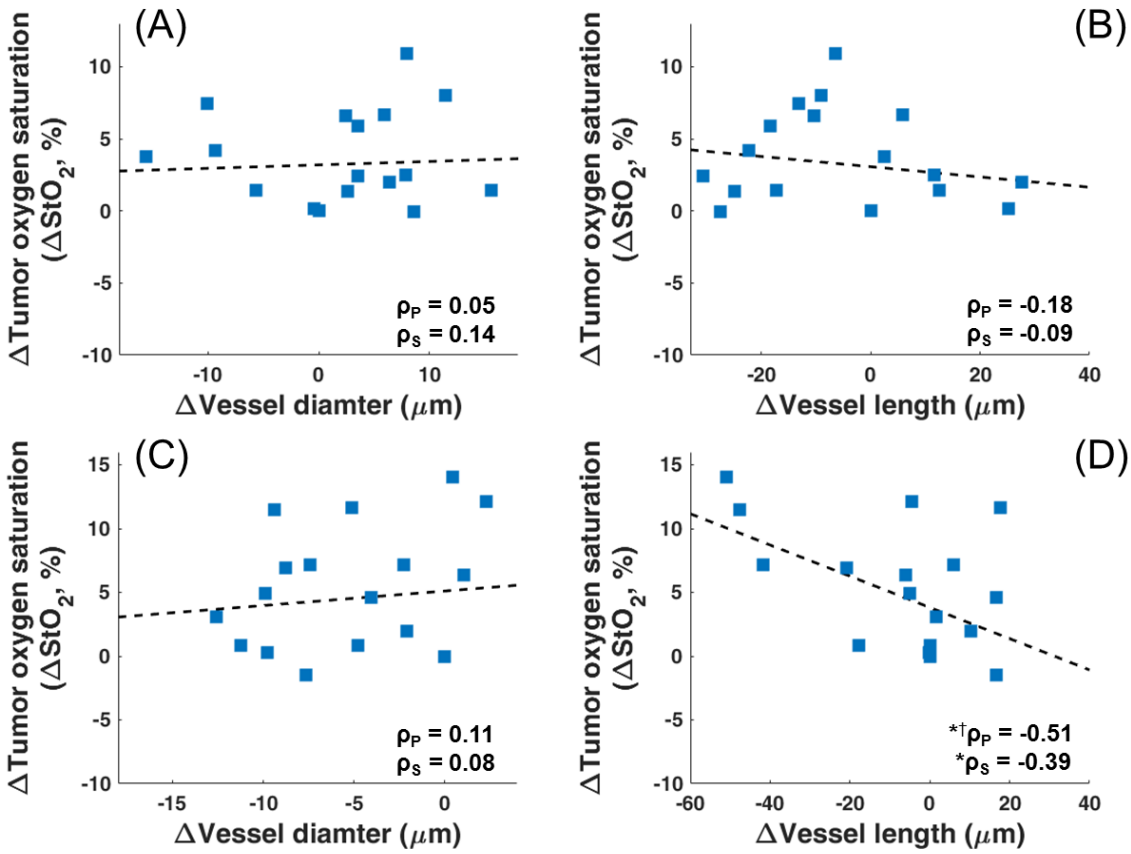

Figure 4-12: Temporal multiscale relationships between changes in tumor vasculature structure and function from baseline (Day -1) in a HR6 tumor treated with mIgG (A and B), and in a BT474 tumor treated with DC101 (C and D). Each point in the plots represents multiscale data from a tumor region in the MIW equivalent in size to a MPM FOV (~825 × 825 μm). Each axis, and thus each data point, represents changes from baseline within a given region extracted from their respective imaging modality and over the same region (SFDI: ΔStO2; MPM: Δ[Vessel diameter] and Δ[Vessel length]). The data comes from 4 different MPM ROIs tracked over 5 days within each tumor (n = 20 data points per correlation plot). The lines represent the lines of best fit to the data in each plot. The Pearson's ρ (ρ_P) and Spearman's ρ (ρ_S) are reported for each plot. *Denotes unadjusted P < 0.05, and †denotes Tukey-Ciminera-Heyse (TCH) adjusted P < 0.05.

These differences may be explained by differences in either treatment (DC101 vs mIgG) or model (HR6 vs BT474). The top row of plots in Figure S4-13 show average changes in mean StO_2 (ΔStO_2) from the 4 MPM ROIs tracked over time in each mouse type (DC101 treated HR6 tumor, mIgG treated HR6 tumor, and DC101 treated BT474 tumor). The plots in the second row from the top show average changes in mean vessel density (Δ[vessel density]) over time from the same 4 MPM ROIs tracked in each mouse type. The plots in the third row from the top show average changes in mean vessel diameter (Δ[vessel diameter]) over time from the same 4 MPM ROIs tracked in each mouse type. Finally, the bottom row of plots show average changes in mean vessel length (Δ[vessel length]) over time from the same 4 MPM ROIs tracked in each mouse type. The plots in Figure S4-13 demonstrate the potential for DNI to track longitudinal changes in vascular structure and function in different tumor models and treatment types, and may provide some insight for exploring differences between tumor models and treatment types in future follow-up DNI studies with a larger number of mice for each model and treatment type.

4.4 Discussion

In this work, we designed and built the first integrated SFDI and MPM, or DNI system for inherently coregistered and comprehensive multiscale measurements of in vivo tumor vascular structure and function over space and time in preclinical tumors. We demonstrated high measurement precision and accuracy with the custom SFDI device portion of the DNI system. In addition, we showed that the DNI system enables longitudinal coregistered measurements of tumor vascular structure and function over a

wide-field, all within a single tumor. Importantly, this proved useful in elucidating multiscale vascular structure-function relationships both over space and time.

One of the enabling features of this work was the ability to make multiscale measurements of tumor vascular structure and function in an inherently coregistered fashion. This was made possible by having SFDI and MPM performed through a shared optical detection path, therefore providing inherent spatial coregistration between tumor oxygenation (function) and tumor microvascular architecture (structure) with the DNI system. Needless to say, this design offered significant advantages over our previous work which acquired SFDI and MPM measurements of tumors on different systems with manual coregistration in post-processing guided by a fiducial mark. Additionally, the smaller field of view and therefore increased sampling resolution for functional measurements of tumors provided a better opportunity to explore spatial heterogeneity relationships between structure and function in tumors. We believe these innovations largely contributed to identifying a negative correlation between StO_2 and vessel density over space at a given measurement time point.

We also found multiscale correlations over time when analyzing for the absolute difference between measurements at all time points and baseline line measurements. We found that changes in StO_2 from baseline were anticorrelated with changes in vessel diameter from baseline in a DC101 treated HR6 tumor measured longitudinally with DNI. In our previous work, we had also found a strong negative correlation between wide-field StO_2 and vessel diameter in a different tumor model that was untreated[73], and noted its relevance to prior reports having also observed this inverse relationship between

oxygenation and vessel size in tumors[80,81]. The DNI system is poised to monitor this potentially important multiscale vascular structure-function relationship during treatment response over space and time. We also found that changes in StO_2 from baseline were correlated with changes in vessel length from baseline. In our previous work we had found a strong negative correlation between wide-field StO_2 and vessel length[73]. Taken all together, this possibly suggests that multiscale relationships could either be conserved or not conserved between: (i) space and time, (ii) different tumors, and/or (iii) different treatment regimens. This is possibly further suggested by our results showing that different tumors receiving the same treatment, or the same tumor undergoing different treatments can present with different multiscale relationships, which could potentially be used to identify differences in treatment response. Additional studies are needed to further explore these ideas.

The work presented here has limitations that can be improved upon going forward. One limitation is that the in vivo vascular results come from n = 1 mouse for each tumor type and treatment regimen measured with DNI, and therefore the reader is cautioned against drawing any biological conclusions from the presented in vivo vascular results as they merely serve to demonstrate what is possible with DNI. A control for the DC101 treated BT474 tumor was also lacking (i.e., a mIgG treated BT474 tumor). Nevertheless, the vascular results from the few mice shown here may potentially be used to inform a future DNI study with proper and larger control and experimental groups. The analysis of spatial relationships between tumor vascular structure and function can also be improved, including an investigation of how the transport mean-free path from diffuse measurements

of vascular function may dictate the length scales over which DNI can be used to explore relationships between tumor vascular structure and function. The results in Figure 4-9 may provide some insight on this: as the spatial divisions became finer, the negative correlation between tumor oxygen saturation and vessel density became weaker (slope became less negative). The diffuse transport mean-free path in tissue is typically on the order of 1 mm[87], and the length of one tile in the 4 x 4 spatial division is closer to 1 mm than the length of a tile from finer spatial divisions. Additionally, spatial analysis methods of DNI measurements could potentially benefit from analyzing the fractal properties of vasculature (e.g. number of branch points) and/or the use of nonlinear spatial divisions such as concentric circles given the fractal-like and nonlinear nature of vascular branching. Finally, future longitudinal DNI studies of in vivo tumor vascular structure and function will likely benefit from active tracking of the same vascular landmarks over time for an enhanced analysis of temporal relationships between tumor vascular structure and function measured with DNI. Overall, the small longitudinal pilot DNI study here was used to demonstrate the potential for DNI to explore in vivo multiscale relationships between tumor vascular structure and function over space and time in different tumor models and treatment regimens.

4.5 Conclusion

In conclusion, we developed a diffuse and nonlinear imaging system to quantify inherently coregistered multiscale structure-function relationships in vivo over space and time, and to demonstrate that DNI has the potential to track these parameters in different treatment and tumor types. Going forward, a larger study will enable comprehensive

investigations into treatment response with DNI in the preclinical setting to identify the biological origins of DOI measurements. Importantly, DNI can help to establish a clear understanding of the relationships between DOI and the underlying tumor biology and create a path towards DOI for personalized and precision medicine to significantly impact and inform adaptive therapy strategies tailored to the in vivo state of each patient's tumor. Ultimately, DNI provides an opportunity to deepen our understanding of the biological underpinnings of DOI feedback on response to cancer therapies in the preclinical setting, allowing for careful control over treatments and imaging to translate potential findings to the clinic.

4.6 Acknowledgements

The authors gratefully acknowledge funding from the U.S. Department of Defense (DoD) (Award No. W81XWH-15-1-0070), as well as funding from the National Cancer Institute of the National Institutes of Health (NIH) (Award No. F99CA223014). The content is solely the responsibility of the authors and does not necessarily represent the official views of the NIH.

4.7 Supplementary Materials

4.7.1 Supporting information

Δwide-field (SFDI)	Δμ-vascular (MPM)	0.05 and 0.1 mm^{-1}								
		Pearson's ρ	Unadjusted p-value	TCH adjusted p-value	BF adjusted p-value	Spearman's ρ	Unadjusted p-value	TCH adjusted p-value	BF adjusted p-value	|Fisher's z|
StO_2 (%)	length (μm)	0.542	0.007	0.027	0.108	0.573	0.004	0.017	0.066	0.608
HbO_2 (μM)	density (%)	0.528	0.008	0.033	0.134	0.438	0.027	0.103	0.428	0.587
THb (μM)	density (%)	0.519	0.010	0.038	0.152	0.385	0.047	0.175	0.751	0.575
HHb (μM)	tortuosity	0.503	0.012	0.047	0.190	0.432	0.029	0.110	0.458	0.554
StO_2 (%)	tortuosity	-0.449	0.024	0.091	0.377	-0.621	0.002	0.007	0.028	0.483
StO_2 (%)	diameter (μm)	-0.430	0.029	0.111	0.466	-0.603	0.002	0.010	0.038	0.460
HHb (μM)	diameter (μm)	0.409	0.037	0.138	0.585	0.385	0.047	0.175	0.751	0.435
HHb (μM)	length (μm)	-0.383	0.048	0.178	0.765	-0.361	0.059	0.216	0.946	0.403
StO_2 (%)	density (%)	0.316	0.087	0.306	1.000	0.239	0.155	0.489	1.000	0.327
HbO_2 (μM)	length (μm)	0.277	0.118	0.395	1.000	0.300	0.099	0.342	1.000	0.285
HHb (μM)	density (%)	0.185	0.218	0.625	1.000	0.082	0.366	0.838	1.000	0.187
THb (μM)	length (μm)	0.136	0.283	0.736	1.000	0.058	0.405	0.874	1.000	0.137
HbO_2 (μM)	diameter (μm)	-0.115	0.314	0.779	1.000	-0.041	0.432	0.896	1.000	0.116
THb (μM)	tortuosity	0.088	0.356	0.828	1.000	0.068	0.388	0.859	1.000	0.088
HbO_2 (μM)	tortuosity	-0.062	0.397	0.868	1.000	-0.132	0.290	0.746	1.000	0.062
THb (μM)	diameter (μm)	0.014	0.476	0.925	1.000	0.117	0.312	0.776	1.000	0.014

Table S4-2: Multiscale vascular temporal relationships explored in a HR6 tumor treated with DC101. This table includes all 16 multiscale correlations tested between structural (Δμ-vascular) metrics and functional (Δwide-field) metrics. For each evaluated multiscale correlation, the Pearson correlation coefficient and Spearman's rank correlation coefficient were computed, along with their respective unadjusted p-values. The p-values were adjusted using both the Tukey-Ciminera-Heyse (TCH) and Bonferroni (BF) procedures to control for the type I error rate. The absolute value of the Fisher z-transformation was also computed from the Pearson's ρ, and the multiscale correlations were arranged from largest to smallest (going down the table) based on the absolute value of their computed Fisher's z.

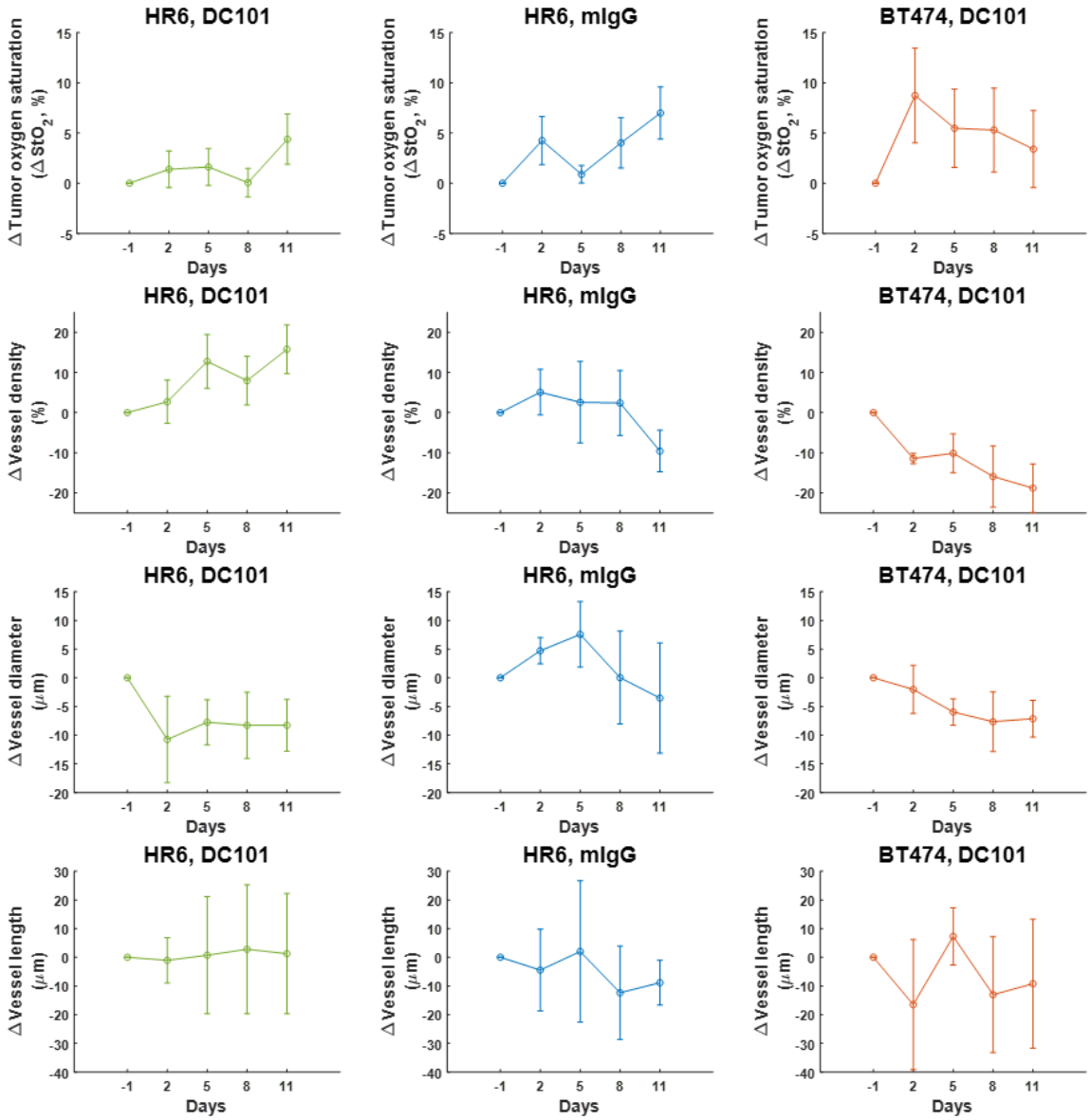

Figure S4-13: Changes in tumor vascular structure and function and their relationships may be treatment and model specific. Changes in tumor vascular structure and function with respect to baseline (day -1) are analyzed for the three mouse types that were measured with DNI longitudinally: DC101 treated HR6 tumor, mIgG treated HR6 tumor, and DC101 treated BT474 tumor. (Top row) Changes in mean StO_2 (ΔStO_2) over time from 4 different MPM ROIs in each mouse type, where the error bars represent the standard deviation of the 4 locations. (2nd row from the top) Changes in mean vessel density (Δ[vessel density]) over time from the same 4 MPM ROIs in each mouse type, where the error bars represent the standard deviation of the 4 locations. (3rd row rom the top) Changes in mean vessel diameter (Δ[vessel diameter]) over time from the same 4 MPM ROIs in each mouse type, where the error bars represent the standard deviation of the 4 locations. (Bottom row) Changes in mean vessel length (Δ[vessel length]) over time from the same 4 MPM ROIs in each mouse type, where the error bars represent the standard deviation of the 4 locations.

BT474 tumors:

- 9 mice inoculated
- Take rate = 5/9
- Mice with tumors past DNI volume threshold (≥150 mm^3) = 1/9
    - Completed longitudinal DNI measurements
    - Passed DNI volume threshold 5 weeks post inoculation

HR6 tumors:

- 6 mice inoculated
- Take rate = 5/6
    - 2 mice completed longitudinal DNI measurements
    - 2 mice unable to make it past two DNI measurement sessions
    - 1 mouse MIW fell out before could do first DNI measurement
- Earliest to pass DNI volume threshold (≥150 mm^3) = 3 weeks post inoculation
- Latest to pass DNI volume threshold (≥150 mm^3) = 7 weeks post inoculation

4.7.2 openSFDI: An open-source guide for constructing a spatial frequency domain imaging system

In building the custom SFDI device for the DNI system, contributions were made to the following which was submitted to the Journal of Biomedical Optics and is currently under review, and includes the following contributing authors:

Matthew B. Applegate,[a] Kavon Karrobi,[a] Joseph Angelo,[b] Wyatt Austin,[c] Syeda Tabassum,[d] Enagnon Agu´enounon,[b] Karissa Tilbury,[c] Rolf Saager,[e] Sylvain Gioux,[b] Darren Roblyer[a]

[a]Department of Biomedical Engineering, Boston University, Boston, Massachusetts, United States

[b]ICube Laboratory, University of Strasbourg, Strasbourg, France

[c]Department of Chemical and Biomedical Engineering, University of Maine, Orono, Maine, United States

[d]Department of Electrical and Computer Engineering, Boston University, Boston, Massachusetts, United States

[e]Department of Biomedical Engineering, Link¨oping University, Link¨oping, Sweden

SFDI is a DOI technique that can quantify volume-averaged tissue optical absorption and scattering on a pixel by pixel basis over a two-dimensional area. Measurements of tissue optical absorption at different wavelengths enables the extraction of molar concentrations of tissue chromophores over a wide-field, providing a non-contact and label-free means to assess tissue viability, oxygenation, micro-architecture, and molecular content. The ability of SFDI to provide quantitative functional and molecular information in tissue, combined with its relative simplicity, safety, and low-cost has led to its use for a variety of biomedical applications. However, although there has been significant advancements made with SFDI over the last decade, it is still in the embryonic

phase of being widely adopted because of a high barrier-to-entry to properly build and use SFDI. Accordingly, an initiative was taken to make SFDI more accessible to those interested in using SFDI to enhance their research applications. An open hardware platform called openSFDI was designed and developed to help other research groups build and use SFDI. OpenSFDI has gained national and international partners helping to further develop and advance the initiative. Multiple phases of the openSFDI project were worked on, including hardware selection and platform validation. Importantly, a modified version of the openSFDI system was incorporated into the DNI system. More details can be found here: www.openSFDI.org.

Chapter 5: Conclusion and future directions

This final chapter summarizes the conclusions from this body of work, and offers directions for related future work.

5.1 Summary of achievements

Chapter 3 presents work that focused on developing a new multiscale preclinical imaging technique called diffuse and nonlinear imaging (DNI) by combining wide-field diffuse optical imaging (DOI) with intravital multiphoton microscopy (MPM). In particular, the first iteration of DNI combines an independent non-contact wide-field DOI system called spatial frequency domain imaging (SFDI) with an independent MPM system. DNI provides structure-function relationships through multiscale datasets of MPM measurements of tumor microvascular architecture (structure) coregistered within wide-field maps of tumor oxygenation (function) from SFDI measurements. The imaging depths of both modalities were compared, and a novel method was developed to match the imaging depths of both modalities by utilizing informed SFDI spatial frequency selection. The tradeoffs between depth matching and the ability to extract optical properties with SFDI was assessed. Procedures to image tumors in a coregistered fashion with DNI were presented, with high x-y spatial coregistration accuracy and precision demonstrated between SFDI and MPM. Methods to extract metrics from each modality were developed, and an in vivo DNI study of murine mammary tumors revealed multiscale relationships between tumor oxygen saturation and microvessel diameter, and tumor oxygen saturation and microvessel length ($|\text{Pearson's } \rho| \geq 0.5$, $P < 0.05$). This was the first study to combine SFDI and MPM for small animal tumor imaging to investigate spatial heterogeneity in

multiscale relationships. In the end, the DNI method was demonstrated to quantify tumor vascular structure– function relationships across length scales. In support of this chapter, contributions were made to the following: (i) modeling and experimental validation to develop a method for determining the optical sampling depth of SFDI for arbitrary samples with arbitrary optical properties, and (ii) a method to estimate optical property uncertainties for SFDI.

Chapter 4 presents a fully integrated DNI system that enables multiscale imaging of in vivo tumor vascular structure and function over space and time in preclinical breast cancer models. The DNI system was designed and constructed by building a custom SFDI device into a MPM system such that SFDI and MPM measurements were acquired through the same optical detection path. This provided inherent spatial coregistration between multiscale tumor vascular structure and function datasets collected with the DNI system from measurements of preclinical tumors through mammary imaging windows (MIWs). Moreover, the smaller SFDI field of view provided greater sampling of spatial functional heterogeneity over the wide-field, which was taken advantage of to explore relationships between multiscale heterogeneity. The performance of the DNI system was characterized before conducting any in vivo measurements. High measurement precision and accuracy with the custom SFDI device portion of the DNI system was demonstrated. Inherently spatially coregistered multiscale measurements of in vivo tumor vascular structure and function over a wide-field were then demonstrated longitudinally, all within a single tumor. Methods of analyzing spatial and temporal multiscale relationships from DNI measurements of in vivo tumor vascular structure and function were presented. A strong

spatial correlation between tumor oxygen saturation (StO_2) and vessel density over the wide-field at a given measurement time point was demonstrated during the course of treatment. Strong temporal correlations between changes in StO_2 from baseline and changes in either vessel diameter or vessel length from baseline were also elucidated. Finally, differences in DNI measurements for different treatment and tumor types were presented. In the end, a DNI system was established as a preclinical tool that can be used to investigate how macro DOI signatures relate to the underlying tumor biology at the micro scale for informed treatment response monitoring. In support of this chapter, contributions were made to the open hardware platform called openSFDI during the construction of custom SFDI device for the DNI system to enable researchers around the world to incorporate SFDI into their research programs.

5.2 Future directions

The work in this thesis provides many potential future directions, some of which are described below.

1. Short-term: Using DNI to investigate whether DOI can identify treatment resistance through demonstrated relationships with micro scale makers of resistance and response. This will involve optimizing the procedure for growing the two tumor models used in Chapter 4 of this thesis: BT474 and HR6. The BT474 breast cancer model overexpresses the HER2 gene, and is therefore susceptible to the drug trastuzumab, clinically used and known as Herceptin® to treat breast cancer patients whose tumors present with overexpression of the HER2 receptor[112]. The HR6 breast cancer model is a resistant version of BT474, able to evade trastuzumab

therapy even though its HER2 expression has been shown to be the same as BT474[112]. A few preclinical reports indicate that differences in the microvascular architecture may exist between the response and resistance during the course of trastuzumab therapy[31,78,119]. This thesis has demonstrated differences in tumor vascular structure and function and their relationships between a HR6 tumor and BT474 tumor both treated with an antiangiogenic. If those microvascular differences in response and resistance to trastuzumab can be linked to DOI measurements via DNI monitoring of trastuzumab treated HR6 and BT474 tumors, this can provide path for demonstrating that DOI is sensitive to treatment resistance.

2. Medium-term: Expand the repertoire of multiscale structure and function metrics that can be measured with DNI. This thesis mainly focused on multiscale metrics related to the tumor vascular structure and function, yet DNI can measure a wide variety of contrasts beyond those related to the vasculature, such as optical scattering, and cellular metabolism/redox and collagen architecture with nonlinear microscopy techniques such as TPEF/fluorescence lifetime imaging microscopy and second harmonic generation (SHG), respectively[34,109]. Accordingly, DNI can be used to exploit these various forms of contrast to explore tumor heterogeneity over multiple imaging spatial scales (macro to the micro), and importantly its role in treatment response. The combination of these various metrics have the potential to provide a complete picture of the in vivo tumor state with DNI.
3. Long-term: Multiscale modeling to link DNI findings back to clinical DOI monitoring of treatment response. Although DNI measures the same functional

metrics as clinical DOI techniques that have been applied to treatment monitoring in cancer patients, it is still unclear how to directly link DNI findings back to clinical DOI monitoring of treatment response. This is in part due to different imaging geometries, depth sensitivities, and measurement domains (time domain, time frequency domain, real spatial domain, and spatial frequency domain). DNI employs a wide-field, non-contact geometry with superficial depth sensitivities and measurements taken in the spatial frequency domain for the DOI portion of the method/system. Modeling to understand how the DOI measurements used in DNI can be related to clinical monitoring with other DOI measurements will be important in the path towards diffuse optical adaptive therapy in the clinic enabled by DNI findings.

4. Technological: Wide-field MPM for DNI. Despite the integrated DNI system providing greater throughput compared to two independent devices, MPM scans are still the rate limiting step in DNI measurements. A wide-field MPM could significantly speed up acquisitions of wide-field microvascular architecture. Wide-field MPM techniques have been explored and developed for preclinical intravital brain imaging[120], and could possibly be adapted for DNI measurements of tumors.
5. Biological: DNI is not specific to tumors, and can be used to assess multiscale biology/physiology in other tissue types/disease contexts. One example would be wound healing/scar formation.

5.3 Conclusion

In the field of biomedical optics and biophotonics, more often than not new imaging tools are developed to provide new ways of measuring biology/physiology that can lead to new biological findings, and/or advance clinical practice to improve patient outcomes. This dissertation has mainly focused on the former with an eye towards supporting the latter. Through this dissertation, a novel preclinical in vivo imaging technique called diffuse and nonlinear imaging (DNI) has been developed which provides the opportunity to: (1) bridge cancer biology with clinical oncology, (2) explore tumor heterogeneity over a range of spatial scales and contrast mechanisms, and (3) monitor tumor structure and function in concert over a wide-field within a single tumor. With DNI, there is the potential to: (i) explore and validate novel drug combinations and scheduling, (ii) identify translational imaging metrics of response and resistance, and (iii) create a path toward diffuse optical image-guided adaptive therapy to improve the efficacy of cancer therapies.

BIBLIOGRAPHY

1. T. D. O'Sullivan, A. E. Cerrusi, D. J. Cuccia, and B. J. Tromberg. Diffuse optical imaging using spatially and temporally modulated light. *Journal of Biomedical Optics* **17**, 071311–1 (2012). PMID22894472.

2. T. Durduran, R. Choe, W. B. Baker, and A. G. Yodh. Diffuse optics for tissue monitoring and tomography. *Reports on Progress in Physics* **73**, 076701 (2010). PMID278930600003.

3. B. E. Schaafsma, M. van de Giessen, a. Charehbili, V. T. H. B. M. Smit, J. R. Kroep, B. P. F. Lelieveldt, G.-J. Liefers, a. Chan, C. W. G. M. Lowik, J. Dijkstra, C. J. H. van de Velde, M. N. J. M. Wasser, and a. L. Vahrmeijer. Optical Mammography Using Diffuse Optical Spectroscopy for Monitoring Tumor Response to Neoadjuvant Chemotherapy in Women with Locally Advanced Breast Cancer. *Clinical Cancer Research* **21**, 577–584 (2015). PMID25473002.

4. S. Jiang, B. W. Pogue, P. A. Kaufman, J. Gui, M. Jermyn, T. E. Frazee, S. P. Poplack, R. DiFlorio-Alexander, W. A. Wells, and K. D. Paulsen. Predicting breast tumor response to neoadjuvant chemotherapy with diffuse optical spectroscopic tomography prior to treatment. *Clinical Cancer Research* **20**, 6006–6015 (2014). PMID25294916.

5. S. Ueda, D. Roblyer, A. Cerussi, A. Durkin, A. Leproux, Y. Santoro, S. Xu, T. D. O 'sullivan, D. Hsiang, R. Mehta, J. Butler, and B. J. Tromberg. Baseline Tumor Oxygen Saturation Correlates with a Pathologic Complete Response in Breast Cancer Patients Undergoing Neoadjuvant Chemotherapy. *Cancer Research* **72**, 4318–4328 (2012).

6. A. Cerussi, D. Hsiang, N. Shah, R. Mehta, A. Durkin, J. Butler, and B. J. Tromberg.

Predicting response to breast cancer neoadjuvant chemotherapy using diffuse optical spectroscopy. *Proceedings of the National Academy of Sciences of the United States of America* **104**, 4014–4019 (2007). PMID17360469.

7. B. W. Pogue, S. P. Poplack, T. O. McBride, W. A. Wells, K. S. Osterman, U. L. Osterberg, and K. D. Paulsen. Quantitative hemoglobin tomography with diffuse near-infrared spectroscopy: Pilot results in the breast. *Radiology* **218**, 261–266 (2001). http://pubs.rsna.org/doi/10.1148/radiology.218.1.r01ja51261.

8. H. Soliman, A. Gunasekara, M. Rycroft, J. Zubovits, R. Dent, J. Spayne, M. J. Yaffe, and G. J. Czarnota. Functional imaging using diffuse optical spectroscopy of neoadjuvant chemotherapy response in women with locally advanced breast cancer. *Clinical Cancer Research* **16**, 2605–2614 (2010). PMID20406836.

9. Q. Zhu, S. Tannenbaum, P. Hegde, M. Kane, C. Xu, and S. H. Kurtzman. Noninvasive monitoring of breast cancer during neoadjuvant chemotherapy using optical tomography with ultrasound localization. *Neoplasia* **10**, 1028–1040 (2008). PMID18813360.

10. D. Roblyer, S. Ueda, A. Cerussi, W. Tanamai, A. Durkin, R. Mehta, D. Hsiang, J. A. Butler, C. McLaren, W.-P. Chen, and B. Tromberg. Optical imaging of breast cancer oxyhemoglobin flare correlates with neoadjuvant chemotherapy response one day after starting treatment. *Proceedings of the National Academy of Sciences of the United States of America* **108**, 14626–14631 (2011).

11. CDC - Cancer Statistics - Women. (n.d.). https://www.cdc.gov/cancer/dcpc/data/women.htm.

12. Cancer of the Breast (Female) - Cancer Stat Facts. (n.d.).

https://seer.cancer.gov/statfacts/html/breast.html.

13. P. R. Pohlmann, I. A. Mayer, and R. Mernaugh. Resistance to trastuzumab in breast cancer. *Clinical Cancer Research* **15**, 7479–7491 (2009). PMID20008848.

14. A. M. Gonzalez-Angulo, F. Morales-Vasquez, and G. N. Hortobagyi. Overview of Resistance to Systemic Therapy in Patients with Breast Cancer. (2013). https://www.ncbi.nlm.nih.gov/books/NBK6306/.

15. E. S. Nakasone, H. A. Askautrud, T. Kees, J.-H. Park, V. Plaks, A. J. Ewald, M. Fein, M. G. Rasch, Y.-X. Tan, J. Qiu, J. Park, P. Sinha, M. J. Bissell, E. Frengen, Z. Werb, and M. Egeblad. Imaging tumor-stroma interactions during chemotherapy reveals contributions of the microenvironment to resistance. *Cancer Cell* **21**, 488–503 (2012). PMID22516258.

16. A. Marusyk, D. P. Tabassum, M. Janiszewska, A. E. Place, A. Trinh, A. I. Rozhok, S. Pyne, J. L. Guerriero, S. Shu, M. Ekram, A. Ishkin, D. P. Cahill, Y. Nikolsky, T. A. Chan, M. F. Rimawi, S. Hilsenbeck, R. Schiff, K. C. Osborne, A. Letai, and K. Polyak. Spatial proximity to fibroblasts impacts molecular features and therapeutic sensitivity of breast cancer cells influencing clinical outcomes. *Cancer Research* **76**, 6495–6506 (2016). PMID27671678.

17. A. S. Clark, E. McDonald, M. C. Lynch, and D. Mankoff. Using nuclear medicine imaging in clinical practice: update on PET to guide treatment of patients with metastatic breast cancer. *Oncology* **28**, 424–30 (2014). PMID25004657.

18. S. Meisamy, P. J. Bolan, E. H. Baker, R. L. Bliss, E. Gulbahce, L. I. Everson, M. T. Nelson, T. H. Emory, T. M. Tuttle, D. Yee, and M. Garwood. Neoadjuvant Chemotherapy

of Locally Advanced Breast Cancer: Predicting Response with in Vivo 1 H MR Spectroscopy—A Pilot Study at 4 T. *Radiology* **233**, 424–431 (2004). PMID15516615.

19. S. L. Jacques and B. W. Pogue. Tutorial on diffuse light transport. *Journal of Biomedical Optics* **13**, 041302 (2008). http://biomedicaloptics.spiedigitallibrary.org/article.aspx?doi=10.1117/1.2967535.

20. A. Torjesen, R. Istfan, and D. Roblyer. Ultrafast wavelength multiplexed broad bandwidth digital diffuse optical spectroscopy for *in vivo* extraction of tissue optical properties. *Journal of Biomedical Optics* **22**, 036009 (2017). http://biomedicaloptics.spiedigitallibrary.org/article.aspx?doi=10.1117/1.JBO.22.3.036009.

21. S. Tabassum, Y. Zhao, R. Istfan, J. Wu, D. J. Waxman, and D. Roblyer. Feasibility of spatial frequency domain imaging (SFDI) for optically characterizing a preclinical oncology model. *Biomedical Optics Express* **7**, 4154 (2016). PMID27867722.

22. M. G. Pakalniskis, W. A. Wells, M. C. Schwab, H. M. Froehlich, S. Jiang, Z. Li, T. D. Tosteson, S. P. Poplack, P. A. Kaufman, B. W. Pogue, and K. D. Paulsen. Tumor angiogenesis change estimated by using diffuse optical spectroscopic tomography: Demonstrated correlation in women undergoing neoadjuvant chemotherapy for invasive breast cancer? *Radiology* **259**, 365–374 (2011). PMID21406632.

23. S. H. Chung, M. D. Feldman, D. Martinez, H. Kim, M. E. Putt, D. R. Busch, J. Tchou, B. J. Czerniecki, M. D. Schnall, M. A. Rosen, A. DeMichele, A. G. Yodh, and R. Choe. Macroscopic optical physiological parameters correlate with microscopic proliferation and vessel area breast cancer signatures. *Breast Cancer Research* **17**, 72

(2015). PMID26013572.

24. Q. Zhu, S. H. Kurtzman, P. Hegde, S. Tannenbaum, M. Kane, M. Huang, N. G. Chen, B. Jagjivan, and K. Zarfos. Utilizing optical tomography with ultrasound localization to image heterogeneous hemoglobin distribution in large breast cancers. *Neoplasia* **7**, 263–270 (2005). PMID15799826.

25. S. Srinivasan, B. W. Pogue, B. Brooksby, S. Jiang, H. Dehghani, C. Kogel, W. A. Wells, S. P. Poplack, and K. D. Paulsen. Near-infrared characterization of breast tumors in vivo using spectrally-constrained reconstruction. *Technology in Cancer Research and Treatment* **4**, 513–526 (2005). PMID16173822.

26. S. P. Poplack, T. D. Tosteson, W. A. Wells, B. W. Pogue, P. M. Meaney, A. Hartov, C. A. Kogel, S. K. Soho, J. J. Gibson, and K. D. Paulsen. Electromagnetic Breast Imaging: Results of a Pilot Study in Women with Abnormal Mammograms. *Radiology* **243**, 350–359 (2007). PMID17400760.

27. A. Ciocalteu, A. Saftoiu, T. Cartana, L. G. Gruionu, D. Pirici, C. C. Georgescu, C.-V. Georgescu, D. I. Gheonea, and G. Gruionu. Evaluation of new morphometric parameters of neoangiogenesis in human colorectal cancer using confocal laser endomicroscopy (CLE) and targeted panendothelial markers. *PLoS ONE* **9**, e91084 (2014). PMID24614504.

28. J. Ehling, T. Lammers, and F. Kiessling. Non-invasive imaging for studying anti-angiogenic therapy effects. *Thrombosis and Haemostasis* **109**, 375–390 (2013). PMID23407722.

29. R. T. Tong, Y. Boucher, S. V. Kozin, F. Winkler, D. J. Hicklin, and R. K. Jain. Vascular normalization by vascular endothelial growth factor receptor 2 blockade induces

a pressure gradient across the vasculature and improves drug penetration in tumors. *Cancer Research* **64**, 3731–3736 (2004). PMID15172975.

30. F. Yuan, H. A. Salehi, Y. Boucher, U. S. Vasthare, R. F. Tuma, and R. K. Jain. Vascular Permeability and Microcirculation of Gliomas and Mammary Carcinomas Transplanted in Rat and Mouse Cranial Windows1. *Cancer Research* **54**, 4564–4568 (1994). http://cancerres.aacrjournals.org/content/canres/54/17/4564.full.pdf.

31. D. R. McCormack, A. J. Walsh, W. Sit, C. L. Arteaga, J. Chen, R. S. Cook, and M. C. Skala. In vivo hyperspectral imaging of microvessel response to trastuzumab treatment in breast cancer xenografts. *Biomedical Optics Express* **5**, 2247 (2014). PMID25071962.

32. R. K. Jain, L. L.Munn, and D. Fukumura. Dissecting tmour pathophysiology using intravital microscopy. *Nature Reviews. Cancer* **2**, 266–276 (2002). http://www.nature.com/nrc/journal/v2/n4/pdf/nrc778.pdf.

33. W. R. Zipfel, R. M. Williams, and W. W. Webb. Nonlinear magic: multiphoton microscopy in the biosciences. *Nature Biotechnology* **21**, 1369–1377 (2003). PMID14595365.

34. P. P. Provenzano, K. W. Eliceiri, and P. J. Keely. Multiphoton microscopy and fluorescence lifetime imaging microscopy (FLIM) to monitor metastasis and the tumor microenvironment. *Clinical & Experimental Metastasis* **26**, 357–370 (2009). http://download.springer.com/static/pdf/706/art%253A10.1007%252Fs10585-008-9204-0.pdf?originUrl=http%3A%2F%2Flink.springer.com%2Farticle%2F10.1007%2Fs10585-008-9204-

0&token2=exp=1488575839~acl=%2Fstatic%2Fpdf%2F706%2Fart%25253A10.1007%

25252Fs10585-008-920.

35. J. Wyckoff, W. Wang, E. Y. Lin, Y. Wang, F. Pixley, E. R. Stanley, T. Graf, J. W. Pollard, J. Segall, and J. Condeelis. A Paracrine Loop between Tumor Cells and Macrophages Is Required for Tumor Cell Migration in Mammary Tumors. *Cancer Research* **64**, 7022–7029 (2004). http://cancerres.aacrjournals.org/content/canres/64/19/7022.full.pdf.

36. J. B. Wyckoff, Y. Wang, E. Y. Lin, J. F. Li, S. Goswami, E. R. Stanley, J. E. Segall, J. W. Pollard, and J. Condeelis. Direct visualization of macrophage-assisted tumor cell intravasation in mammary tumors. *Cancer Research* **67**, 2649–2656 (2007). PMID17363585.

37. J. M. Szulczewski, D. R. Inman, D. Entenberg, S. M. Ponik, J. Aguirre-Ghiso, J. Castracane, J. Condeelis, K. W. Eliceiri, and P. J. Keely. In Vivo Visualization of Stromal Macrophages via label-free FLIM-based metabolite imaging. *Scientific Reports* **6**, 25086 (2016). PMID27220760.

38. A. T. Shah, K. E. Diggins, A. J. Walsh, J. M. Irish, and M. C. Skala. In Vivo Autofluorescence Imaging of Tumor Heterogeneity in Response to Treatment. *Neoplasia* **17**, 862–870 (2015).

39. D. J. Cuccia, F. Bevilacqua, A. J. Durkin, and B. J. Tromberg. Modulated imaging: quantitative analysis and tomography of turbid media in the spatial-frequency domain. *Optics Letters* **30**, 1354 (2005). https://www.osapublishing.org/abstract.cfm?URI=ol-30-11-1354.

40. D. J. Cuccia, F. Bevilacqua, A. J. Durkin, F. R. Ayers, and B. J. Tromberg. Quantitation and mapping of tissue optical properties using modulated imaging. *Journal of Biomedical Optics* **14**, 024012-024012–13 (2009). PMID19405742.

41. J. P. Angelo, S.-J. Chen, M. Ochoa, U. Sunar, S. Gioux, and X. Intes. Review of structured light in diffuse optical imaging. *Journal of Biomedical Optics* **24**, 1 (2018). https://www.spiedigitallibrary.org/journals/journal-of-biomedical-optics/volume-24/issue-07/071602/Review-of-structured-light-in-diffuse-optical-imaging/10.1117/1.JBO.24.7.071602.full.

42. S. Gioux, A. Mazhar, and D. J. Cuccia. Spatial frequency domain imaging in 2019: principles, applications, and perspectives. *Journal of Biomedical Optics* **24**, 1 (2019). https://www.spiedigitallibrary.org/journals/journal-of-biomedical-optics/volume-24/issue-07/071613/Spatial-frequency-domain-imaging-in-2019--principles-applications-and/10.1117/1.JBO.24.7.071613.full.

43. K. P. Nadeau, T. B. Rice, A. J. Durkin, and B. J. Tromberg. Multifrequency synthesis and extraction using square wave projection patterns for quantitative tissue imaging. *Journal of Biomedical Optics* **20**, 116005 (2015). PMID26524682.

44. M. Martinelli, A. Gardner, D. Cuccia, C. Hayakawa, J. Spanier, and V. Venugopalan. Analysis of single Monte Carlo methods for prediction of reflectance from turbid media. *Optics Express* **19**, 19627 (2011). PMID21996904.

45. A. R. Gardner and V. Venugopalan. Accurate and efficient Monte Carlo solutions to the radiative transport equation in the spatial frequency domain. *Optics Letters* **36**, 2269–71 (2011). PMID21685989.

46. W. G. Zijlstra and A. Buursma. Spectrophotometry of hemoglobin: Absorption spectra of bovine oxyhemoglobin, deoxyhemoglobin, carboxyhemoglobin, and methemoglobin. *Comparative Biochemistry and Physiology - B Biochemistry and Molecular Biology* **118**, 743–749 (1997). PMID3119280.

47. A. Yafi, T. S. Vetter, T. Scholz, S. B. Patel Rolf Saager, D. J. Cuccia, G. R. Evans, and A. J. Durkin. Postoperative Quantitative Assessment of Reconstructive Tissue Status in a Cutaneous Flap Model Using Spatial Frequency Domain Imaging. *Plastic and Reconstructive Surgery* **127**, (2011). https://insights.ovid.com/pubmed?pmid=21200206.

48. S. Gioux, A. Mazhar, B. T. Lee, S. J. Lin, A. M. Tobias, D. J. Cuccia, A. Stockdale, R. Oketokoun, Y. Ashitate, E. Kelly, M. Weinmann, N. J. Durr, L. A. Moffitt, A. J. Durkin, B. J. Tromberg, and J. V. Frangioni. First-in-human pilot study of a spatial frequency domain oxygenation imaging system. *Journal of Biomedical Optics* **16**, 086015 (2011). http://biomedicaloptics.spiedigitallibrary.org/article.aspx?doi=10.1117/1.3614566.

49. J. Q. Nguyen, C. Crouzet, T. Mai, K. Riola, D. Uchitel, L.-H. Liaw, N. Bernal, A. Ponticorvo, B. Choi, and A. J. Durkin. Spatial frequency domain imaging of burn wounds in a preclinical model of graded burn severity. *Journal of Biomedical Optics* **18**, 066010 (2013). http://biomedicaloptics.spiedigitallibrary.org/article.aspx?doi=10.1117/1.JBO.18.6.066010.

50. A. Ponticorvo, E. Taydas, A. Mazhar, T. Scholz, H.-S. Kim, J. Rimler, G. R. D. Evans, D. J. Cuccia, and A. J. Durkin. Quantitative assessment of partial vascular occlusions in a swine pedicle flap model using spatial frequency domain imaging.

Biomedical Optics Express **4**, 298–306 (2013). PMID23412357.

51. A. J. Lin, G. Liu, N. A. Castello, J. J. Yeh, R. Rahimian, G. Lee, V. Tsay, A. J. Durkin, B. Choi, F. M. LaFerla, Z. Chen, K. N. Green, and B. J. Tromberg. Optical imaging in an Alzheimer's mouse model reveals amyloid-β-dependent vascular impairment. *Neurophotonics* **1**, 011005 (2014). PMID25133200.

52. R. P. Singh-Moon, D. M. Roblyer, I. J. Bigio, and S. Joshi. Spatial mapping of drug delivery to brain tissue using hyperspectral spatial frequency-domain imaging. *Journal of Biomedical Optics* **19**, 096003 (2014). PMID25199058.

53. R. B. Saager, D. J. Cuccia, S. Saggese, K. M. Kelly, and A. J. Durkin. A Light Emitting Diode (LED) Based Spatial Frequency Domain Imaging System for Optimization of Photodynamic Therapy of Nonmelanoma Skin Cancer: Quantitative Reflectance Imaging. *Lasers in Surgery and Medicine* **45**, 207–215 (2013). http://doi.wiley.com/10.1002/lsm.22139.

54. J. Kress, D. J. Rohrbach, K. A. Carter, D. Luo, S. Shao, S. Lele, J. F. Lovell, and U. Sunar. Quantitative imaging of light-triggered doxorubicin release. *Biomedical Optics Express* **6**, 3546–55 (2015). PMID26417522.

55. D. M. McClatchy, E. J. Rizzo, W. A. Wells, P. P. Cheney, J. C. Hwang, K. D. Paulsen, B. W. Pogue, and S. C. Kanick. Wide-field quantitative imaging of tissue microstructure using sub-diffuse spatial frequency domain imaging. *Optica* **3**, 613 (2016). http://dx.doi.org/10.1364/optica.3.000613.s001.

56. D. M. McClatchy, E. J. Rizzo, W. A. Wells, C. C. Black, K. D. Paulsen, S. C. Kanick, and B. W. Pogue. Light scattering measured with spatial frequency domain imaging can

predict stromal versus epithelial proportions in surgically resected breast tissue. *Journal of Biomedical Optics* **24**, 1 (2018). https://www.spiedigitallibrary.org/journals/journal-of-biomedical-optics/volume-24/issue-07/071605/Light-scattering-measured-with-spatial-frequency-domain-imaging-can-predict/10.1117/1.JBO.24.7.071605.full.

57. B. W. Maloney, S. S. Streeter, D. M. McClatchy, B. W. Pogue, E. J. Rizzo, W. A. Wells, and K. D. Paulsen. Structured light imaging for breast-conserving surgery, part I: optical scatter and color analysis. *Journal of Biomedical Optics* **24**, 1 (2019). https://www.spiedigitallibrary.org/journals/journal-of-biomedical-optics/volume-24/issue-09/096002/Structured-light-imaging-for-breast-conserving-surgery-part-I/10.1117/1.JBO.24.9.096002.full.

58. S. S. Streeter, B. W. Maloney, D. M. McClatchy, M. Jermyn, B. W. Pogue, E. J. Rizzo, W. A. Wells, and K. D. Paulsen. Structured light imaging for breast-conserving surgery, part II: texture analysis and classification. *Journal of Biomedical Optics* **24**, 1 (2019). https://www.spiedigitallibrary.org/journals/journal-of-biomedical-optics/volume-24/issue-09/096003/Structured-light-imaging-for-breast-conserving-surgery-part-II/10.1117/1.JBO.24.9.096003.full.

59. M. Sibai. Quantitative Surface and Sub-Surface Fluorescence Spatial Frequency Domain Imaging for the Enhanced Resection of Glioma. Unpublished doctoral dissertation – University of Toronto, 2017. https://tspace.library.utoronto.ca/bitstream/1807/95676/1/Sibai_Mira_201806_PhD_thesis.pdf

60. C. M. Robbins, G. Raghavan, J. F. Antaki, and J. M. Kainerstorfer. Feasibility of spatial frequency-domain imaging for monitoring palpable breast lesions. *Journal of Biomedical Optics* **22**, 1 (2017). https://www.spiedigitallibrary.org/journals/journal-of-biomedical-optics/volume-22/issue-12/121605/Feasibility-of-spatial-frequency-domain-imaging-for-monitoring-palpable-breast/10.1117/1.JBO.22.12.121605.full.

61. M. Yang, E. Baranov, J.-W. Wang, P. Jiang, X. Wang, F.-X. Sun, M. Bouvet, A. R. Moossa, S. Penman, and R. M. Hoffman. Direct external imaging of nascent cancer, tumor progression, angiogenesis, and metastasis on internal organs in the fluorescent orthotopic model. *Proceedings of the National Academy of Sciences of the United States of America* **99**(6), 3824–3829 (2002). http://www.pnas.org/content/99/6/3824.full.pdf.

62. D. Kedrin, B. Gligorijevic, J. Wyckoff, V. V Verkhusha, J. Condeelis, J. E. Segall, and J. Van Rheenen. Intravital imaging of metastatic behavior through a mammary imaging window. *Nature Methods* **5**, 1019–21 (2008). PMID18997781.

63. M. Alieva, L. Ritsma, R. J. Giedt, R. Weissleder, and J. van Rheenen. Imaging windows for long-term intravital imaging. *IntraVital* **3**, e29917 (2014). http://www.tandfonline.com/doi/abs/10.4161/intv.29917.

64. M. Balu, A. Mazhar, C. K. Hayakawa, R. Mittal, T. B. Krasieva, K. Kö, V. Venugopalan, and B. J. Tromberg. In Vivo Multiphoton NADH Fluorescence Reveals Depth-Dependent Keratinocyte Metabolism in Human Skin. *Biophysical Journal* **104**, 258–267 (2013). http://ac.els-cdn.com/S0006349512050564/1-s2.0-S0006349512050564-main.pdf?_tid=d4650a14-9dc6-11e7-92d9-00000aacb361&acdnat=1505886475_af9dd8d10787ae9625c7a4cf1bc821fd.

65. R. B. Saager, M. Balu, V. Crosignani, A. Sharif, A. J. Durkin, K. M. Kelly, and B. J. Tromberg. In vivo measurements of cutaneous melanin across spatial scales : using multiphoton microscopy and spatial frequency domain spectroscopy spatial scales : using multiphoton microscopy and. *Journal of Biomedical Optics* **20**, 066005 (2015).

66. R. K. Jain. Normalization of tumor vasculature: an emerging concept in antiangiogenic therapy. *Science* **307**, 58–62 (2005). PMID15637262.

67. C. Carmona-Fontaine, M. Deforet, L. Akkari, C. B. Thompson, J. A. Joyce, and J. B. Xavier. Metabolic origins of spatial organization in the tumor microenvironment. *Proceedings of the National Academy of Sciences of the United States of America* **114**, 2934–2939 (2017). PMID28246332.

68. R. J. Gillies, D. Verduzco, and R. A. Gatenby. Evolutionary dynamics of carcinogenesis and why targeted therapy does not work. *Nature Reviews. Cancer* **12**, 487–493 (2012). PMID22695393.

69. J. D. Martin, D. Fukumura, D. G. Duda, Y. Boucher, and R. K. Jain. Reengineering the Tumor Microenvironment Heterogeneity. *Cold Spring Harbor Perspectives in Medicine* **6**(12), a027094 (2016). PMID27663981.

70. A. Rapisarda and G. Melillo. Role of the hypoxic tumor microenvironment in the resistance to anti-angiogenic therapies. *Drug Resistance Updates : Reviews and Commentaries in Antimicrobial and Anticancer Chemotherapy* **12**, 74–80 (2009). PMID19394890.

71. G. Fluegen, A. Avivar-Valderas, Y. Wang, M. R. Padgen, J. K. Williams, A. R. Nobre, V. Calvo, J. F. Cheung, J. J. Bravo-Cordero, D. Entenberg, J. Castracane, V.

Verkhusha, P. J. Keely, J. Condeelis, and J. A. Aguirre-Ghiso. Phenotypic heterogeneity of disseminated tumour cells is preset by primary tumour hypoxic microenvironments. *Nature Cell Biology* **19**(2), 120–132 (2017). https://www.nature.com/ncb/journal/v19/n2/pdf/ncb3465.pdf.

72. O. Trédan, C. M. Galmarini, K. Patel, and I. F. Tannock. Drug resistance and the solid tumor microenvironment. *Journal of the National Cancer Institute* **99**, 1441–1454 (2007). PMID17895480.

73. K. Karrobi, A. Tank, S. Tabassum, V. Pera, and D. Roblyer. Diffuse and nonlinear imaging of multiscale vascular parameters for in vivo monitoring of preclinical mammary tumors. *Journal of Biophotonics* **12**, e201800379 (2019). PMID30706695.

74. P. G. Anderson, J. M. Kainerstorfer, A. Sassaroli, N. Krishnamurthy, M. J. Homer, R. A. Graham, and S. Fantini. Broadband optical mammography: Chromophore concentration and hemoglobin saturation contrast in breast cancer. *PLoS ONE* **10**, e0117322 (2015). PMID25781469.

75. B. J. Tromberg, Z. Zhang, A. Leproux, T. D. O'Sullivan, A. E. Cerussi, P. M. Carpenter, R. S. Mehta, D. Roblyer, W. Yang, K. D. Paulsen, B. W. Pogue, S. Jiang, P. A. Kaufman, A. G. Yodh, S. H. Chung, M. Schnall, B. S. Snyder, N. Hylton, D. A. Boas, S. A. Carp, S. J. Isakoff, and D. Mankoff. Predicting responses to neoadjuvant chemotherapy in breast cancer: ACRIN 6691 trial of diffuse optical spectroscopic imaging. *Cancer Research* **76**, 5933–5944 (2016). PMID27527559.

76. C. Zhou, R. Choe, N. Shah, T. Durduran, G. Yu, A. Durkin, D. Hsiang, R. Mehta, J. Butler, A. Cerussi, B. J. Tromberg, and A. G. Yodh. Diffuse optical monitoring of blood

flow and oxygenation in human breast cancer during early stages of neoadjuvant chemotherapy. *Journal of Biomedical Optics* **12**, 051903 (2007). PMID17994886.

77. Q. Zhu, S. Tannenbaum, S. H. Kurtzman, P. DeFusco, A. Ricci, H. Vavadi, F. Zhou, C. Xu, A. Merkulov, P. Hegde, M. Kane, L. Wang, and K. Sabbath. Identifying an early treatment window for predicting breast cancer response to neoadjuvant chemotherapy using immunohistopathology and hemoglobin parameters. *Breast Cancer Research* **20**, 56 (2018). https://breast-cancer-research.biomedcentral.com/articles/10.1186/s13058-018-0975-1.

78. Y. Izumi, L. Xu, D. di Tomaso, Emmanuelle Fukumura, and R. K. Jain. Tumour biology: Herceptin acts as an anti-angiogenic cocktail. *Nature* **416**, 279–80 (2002). PMID11907566.

79. F. Yuan, Y. Chen, M. Dellian, N. Safabakhsh, N. Ferrara, and R. K. Jain. Time-dependent vascular regression and permeability changes in established human tumor xenografts induced by an anti-vascular endothelial growth factor/vascular permeability factor antibody. *Proceedings of the National Academy of Sciences of the United States of America* **93**, 14765–14770 (1996). PMID8962129.

80. J. W. Baish, Y. Gazit, D. A. Berk, M. Nozue, L. T. Baxter, and R. K. Jain. Role of Tumor Vascular Architecture in Nutrient and Drug Delivery: An Invasino Percolation-Based Network Model. *Microvascular Research* **51**, 327–346 (1996).

81. D. Fukumura and R. K. Jain. Tumor microvasculature and microenvironment: Targets for anti-angiogenesis and normalization. *Microvascular Research* **74**, 72–84 (2007). http://ac.els-cdn.com/S002628620700060X/1-s2.0-S002628620700060X-

main.pdf?_tid=a9d63472-6814-11e7-a6c1-00000aab0f6b&acdnat=1499982541_f5ddd9d964a5f7116c50f7ea0312b004.

82. W. A. Wells, P. E. Barker, C. MacAulay, M. Novelli, R. M. Levenson, and J. M. Crawford. Validation of novel optical imaging technologies: the pathologists' view. *Journal of Biomedical Optics* **12**, 051801 (2007). http://biomedicaloptics.spiedigitallibrary.org/article.aspx?doi=10.1117/1.2795569.

83. V. Demidov, A. Maeda, M. Sugita, V. Madge, S. Sadanand, C. Flueraru, and I. A. Vitkin. Preclinical longitudinal imaging of tumor microvascular radiobiological response with functional optical coherence tomography. *Scientific Reports* **8**, 38 (2018). http://www.nature.com/articles/s41598-017-18635-w.

84. S. Tabassum, V. Pera, G. Greening, T. J. Muldoon, and D. Roblyer. Two-layer inverse model for improved longitudinal preclinical tumor imaging in the spatial frequency domain. *Journal of Biomedical Optics* **23**, 076011 (2018). https://www.spiedigitallibrary.org/journals/journal-of-biomedical-optics/volume-23/issue-07/076011/Two-layer-inverse-model-for-improved-longitudinal-preclinical-tumor-imaging/10.1117/1.JBO.23.7.076011.full.

85. S. Preibisch, S. Saalfeld, and P. Tomancak. Globally optimal stitching of tiled 3D microscopic image acquisitions. *Bioinformatics* **25**, 1463–5 (2009). PMID19346324.

86. X. Song, B. W. Pogue, S. Jiang, M. M. Doyley, H. Dehghani, T. D. Tosteson, and K. D. Paulsen. Automated region detection based on the contrast-to-noise ratio in near-infrared tomography. *Applied Optics* **43**, 1053–1062 (2004). PMID15008484.

87. C. K. Hayakawa, K. Karrobi, V. Pera, D. Roblyer, and V. Venugopalan. Optical sampling depth in the spatial frequency domain. *Journal of Biomedical Optics* **23**, 1–14 (2018). PMID30141285.

88. V. Pera, K. Karrobi, S. Tabassum, F. Teng, and D. Roblyer. Optical property uncertainty estimates for spatial frequency domain imaging. *Biomedical Optics Express* **9**, 661–678 (2018). PMID29552403.

89. K. Gibby, W.-K. You, K. Kadoya, H. Helgadottir, L. J. Young, L. G. Ellies, Y. Chang, R. D. Cardiff, and W. B. Stallcup. Early vascular deficits are correlated with delayed mammary tumorigenesis in the MMTV-PyMT transgenic mouse following genetic ablation of the NG2 proteoglycan. *Breast Cancer Research* **14**, R67 (2012). PMID22531600.

90. B. Gligorijevic, D. Kedrin, J. E. Segall, J. Condeelis, and J. van Rheenen. Dendra2 photoswitching through the Mammary Imaging Window. *Journal of Visualized Experiments : JoVE* **28**, (2009). PMID19578330.

91. D. A. Gil, G. Kaushik, E. Torr, E. S. Berge, C. Soref, P. Uhl, G. Fontana, J. Antosiewicz-Bourget, C. Edington, M. P. Schwartz, L. G. Griffith, J. A. Thomson, W. T. Daly, W. L. Murphy, and M. C. Skala. in *Proceedings of SPIE 10497, Imaging, Manipulation, and Analysis of Biomolecules, Cells, and Tissues XVI*, edited by D. L. Farkas, D. V. Nicolau, and R. C. Leif (SPIE, 2018), p. 20.

92. M. Berndt-Schreiber. Morphological operations in Fundus image analysis. *Journal of Medical Informatics & Technologies* **11**, 79–86 (2007).

93. K. Bahadar Khan, A. A Khaliq, M. Shahid, and S. Khan. An efficient technique for retinal vessel segmentation and denoising using modified isodata and CLAHE. *IIUM Engineering Journal* **17**, 31–46 (2016). http://journals.iium.edu.my/ejournal/index.php/iiumej/article/view/611.

94. K. Bahadar Khan, A. A Khaliq, and M. Shahid. A Morphological Hessian Based Approach for Retinal Blood Vessels Segmentation and Denoising Using Region Based Otsu Thresholding. *PLoS ONE* **11**, e0158996 (2016). https://dx.plos.org/10.1371/journal.pone.0158996.

95. J. Dash and N. Bhoi. Retinal blood vessel segmentation using Otsu thresholding with principal component analysis. In *2018 Second International Conference on Inventive Systems and Control (ICISC)* (IEEE, 2018), pp. 933–937. doi:10.1109/ICISC.2018.8398938

96. D.-J. Kroon and C. H. Slump. Coherence filtering to enhance the mandibular canal in cone-beam CT data. In *Proceedings of the 4th Annual Symposium of the IEEE-EMBS Benelux Chapter* (2009), pp. 41–44.

97. D.-J. Kroon, C. H. Slump, and T. J. J. Maal. Optimized anisotropic rotational invariant diffusion scheme on cone-beam CT. In T. Jiang et al. (eds.) *Medical Image Computing and Computer-Assisted Intervention – MICCAI 2010, 13th International Conference.* pp. 221–228. *Lecture Notes in Computer Science*, Vol. 6363. Springer, 2010

98. Shashank, M. Bhattacharya, and G. K. Sharma. Optimized coronary artery segmentation using Frangi filter and anisotropic diffusion filtering. In *Proceedings of the 2013 International Symposium on Computational and Business Intelligence.* (IEEE, 2013),

pp. 261–264.

99. S. Gu, Y. Zhen, N. Wang, and J. Pu. Computerized detection of retina blood vessel using a piecewise line fitting approach. In *Proceedings of SPIE 8670, Medical Imaging 2013: Computer-Aided Diagnosis*, edited by C. L. Novak and S. Aylward (International Society for Optics and Photonics, 2013), p. 86702I. doi:10.1117/12.2007786

100. R. Manniesing, M. A. Viergever, and W. J. Niessen. Vessel enhancing diffusion: A scale space representation of vessel structures. *Medical Image Analysis* **10**, 815–825 (2006). PMID16876462.

101. A. F. Frangi, W. J. Niessen, K. L. Vincken, and M. A. Viergever. Multiscale vessel enhancement filtering. In *Medical Image Computing and Computer-Aided Intervention – MICCAI'98*, edited by W. M. Wells, A. Colchester, and S. Delp. *Lecture Notes in Computer Science*, Vol. 1496 (Springer, Berlin, Heidelberg, 1998), pp. 130–137.

102. J. Mazzaferri, B. Larrivée, B. Cakir, P. Sapieha, and S. Costantino. A machine learning approach for automated assessment of retinal vasculature in the oxygen induced retinopathy model. *Scientific Reports* **8**, 3916 (2018). http://www.nature.com/articles/s41598-018-22251-7.

103. D. Chen, J. Deng, X. Xie, P. Nithiarasu, and D. Smith. Efficient reconstruction of coronary vessels from 2D angiography. In *CMBE13: 3rd International Conference on Computational & Mathematical Biomedical Engineering.* edited by P. Nithiarasu, K.M. Lew, and R. Löhner (CMBE, Hong Kong, 2013), pp. 425–428. https://www.compbiomed.net/getfile.php?type=10/site_documents&id=CMBE13_PROCEEDINGS.pdf

104. X. Yang, K.T.T. Cheng, and A. Chien. Geodesic active contours with adaptive configuation for cerebral vessel and aneurysm segmentation. In *Proceedings of the 22nd International Conference on Pattern Recognition, ICPR 2014* (IEEE, 2014), pp. 3209–3214. doi:10.1109/ICPR.2014.553

105. F. Hu, H. Martin, A. Martinez, J. Everitt, A. Erkanli, W. T. Lee, M. Dewhirst, and N. Ramanujam. Distinct angiogenic changes during carcinogenesis defined by novel label-free dark-field imaging in a hamster cheek pouch model. *Cancer Research* **77**, 7109–7119 (2017). http://cancerres.aacrjournals.org/content/canres/77/24/7109.full.pdf.

106. J. A. Montoya-Zegarra, E. Russo, P. Runge, M. Jadhav, A.-H. Willrodt, S. Stoma, S. F. Nørrelykke, M. Detmar, and C. Halin. AutoTube: a novel software for the automated morphometric analysis of vascular networks in tissues. *Angiogenesis* **22**(2), 223–236 (2018). http://link.springer.com/10.1007/s10456-018-9652-3.

107. A. J. Sankoh, M. F. Huque, and S. D. Dubey. Some comments on frequently used multiple endpoint adjustment methods in clinical trials. *Statistics in Medicine* **16**, 2529–2542 (1997). http://doi.wiley.com/10.1002/%28SICI%291097-0258%2819971130%2916%3A22%3C2529%3A%3AAID-SIM692%3E3.0.CO%3B2-J.

108. M. A. Franceschini, K. T. Moesta, S. Fantini, G. Gaida, E. Gratton, H. Jess, W. W. Mantulin, M. Seeber, P. M. Schlag, and M. Kaschke. Frequency-domain techniques enhance optical mammography: Initial clinical results. *Proceedings of the National Academy of Sciences of the United States of America* **94**, 6468–6473 (1997). PMID9177241.

109. W. R. Zipfel, R. M. Williams, R. Christie, A. Y. Nikitin, B. T. Hyman, and W. W.

Webb. Live tissue intrinsic emission microscopy using multiphoton-excited native fluorescence and second harmonic generation. *Proceedings of the National Academy of Sciences of the United States of America* **100**, 7075–7080 (2003). PMID12756303.

110. A. C. Ruifrok and D. A. Johnston. Quantification of histochemical staining by color deconvolution. *Analytical and Quantitative Cytology and Histology* **23**, 291–299 (2001). PMID11531144.

111. F. Ayers, A. Grant, D. Kuo, D. J. Cuccia, and A. J. Durkin. Fabrication and characterization of silicone-bassed tissue phantoms with tunable optical properties in the visibile and near infrared domain. In *Proceedings of SPIE 6870, Design and Performance Validation of Phantoms Used in Conjunction with Optical Measurements of Tissue*, edited by R. J. Nordstrom (International Society for Optics and Photonics, 2008), p. 687007. https://doi.org/10.1117/12.764969

112. C. A. Ritter, M. Perez-Torres, C. Rinehart, M. Guix, T. Dugger, J. A. Engelman, and C. L. Arteaga. Human breast cancer cells selected for resistance to trastuzumab in vivo overexpress epidermal growth factor receptor and ErbB ligands and remain dependent on the ErbB receptor network. *Clinical Cancer Research* **13**, 4909–19 (2007). PMID17699871.

113. R. Schafer, H. M. Leung, and A. F. Gmitro. Multi-modality imaging of a murine mammary window chamber for breast cancer research. *BioTechniques* **57**, 45–50 (2014). PMID25005693.

114. H. M. Leung and A. F. Gmitro. Fluorescence and reflectance spectral imaging system for a murine mammary window chamber model. *Biomedical Optics Express* **6**,

2887 (2015). https://www.osapublishing.org/abstract.cfm?URI=boe-6-8-2887.

115. T. Yardeni, M. Eckhaus, H. D. Morris, M. Huizing, and S. Hoogstraten-Miller. Retro-orbital injections in mice. *Lab Animal* **40**, 155–60 (2011). PMID21508954.

116. G. Kaushik, D. A. Gil, E. Torr, E. S. Berge, C. Soref, P. Uhl, G. Fontana, J. Antosiewicz-Bourget, C. Edington, M. P. Schwartz, L. G. Griffith, J. A. Thomson, M. C. Skala, W. T. Daly, and W. L. Murphy. Quantitative Label-Free Imaging of 3D Vascular Networks Self-Assembled in Synthetic Hydrogels. *Advanced Healthcare Materials* **8**, 1801186 (2019). http://doi.wiley.com/10.1002/adhm.201801186.

117. A. Saria and J. M. Lundberg. Evans blue fluorescence: quantitative and morphological evaluation of vascular permeability in animal tissues. *Journal of Neuroscience Methods* **8**, 41–49 (1983). https://www.sciencedirect.com/science/article/pii/016502708390050X.

118. J. Yao, K. Maslov, S. Hu, and L. V Wang. Evans blue dye-enhanced capillary-resolution photoacoustic microscopy in vivo. *Journal of Biomedical Optics* **14**, 054049 (2009). PMID19895150.

119. J. M. Du Manoir, G. Francia, S. Man, M. Mossoba, J. A. Medin, A. Viloria-Petit, D. J. Hicklin, U. Emmenegger, and R. S. Kerbel. Strategies for delaying or treating In vivo acquired resistance to trastuzumab in human breast cancer xenografts. *Clinical Cancer Research* **12**, 904–916 (2006). http://clincancerres.aacrjournals.org/content/clincanres/12/3/904.full.pdf.

120. J. R. Bumstead, J. J. Park, I. A. Rosen, A. W. Kraft, P. W. Wright, M. D. Reisman, D. C. Côté, and J. P. Culver. Designing a large field-of-view two-photon microscope using

optical invariant analysis. *Neurophotonics* **5**, 1 (2018). https://www.spiedigitallibrary.org/journals/neurophotonics/volume-5/issue-02/025001/Designing-a-large-field-of-view-two-photon-microscope-using/10.1117/1.NPh.5.2.025001.full.

CURRICULUM VITAE

KAVON KARROBI

Department of Biomedical Engineering
Boston University
44 Cummington Mall
Boston, MA 02215

Mobile: 510-851-9994
Email: kkarrobi@bu.edu
Current Lab: www.bu.edu/botlab

EDUCATION

2014-2020	Ph.D. in Biomedical Engineering, Boston University, Boston, MA Expected conferred degree 2020 January
2010-2014	B.S. in Biomedical Engineering, Boston University, Boston, MA Minor in Chemistry *Magna Cum Laude*

POSITIONS HELD

2014-2020 Graduate Student, Boston University, Biomedical Engineering, Boston, MA
Advisor: Prof. Darren Roblyer, Biomedical Optical Technologies Laboratory

Project(s): Developed Diffuse and Nonlinear Imaging (DNI) for monitoring multiscale vascular parameters associated with treatment response in preclinical mammary tumors

2012-2014 Research Assistant, Boston University, Mechanical Engineering, Boston, MA
Advisor: Prof. Tyrone Porter, Nanotechnology and Medical Acoustics Laboratory

Project(s): Engineered targeted lipid and lipid-polymer hybrid nanoparticles, as well as lipid-coated double emulsion particles as drug and gene (DNA, siRNA) delivery systems for applications in cancer therapy, immunotherapy, and treatment of vascular diseases

2013 Research Assistant, UCSF, Bioengineering, San Francisco, CA
Advisor: Prof. Francis C. Szoka Jr.

Project(s): Fabricated and analyzed variants of a murine neonatal Fc receptor (FcRn) binding protein (FcBP) designed to optimize the pharmacokinetics and delivery of therapeutic recombinant proteins based on in silico affinity maturation models

2011 Research Assistant, UC Berkeley, Molecular and Cell Biology, Berkeley, CA
Advisor: Prof. Peter Duesberg

Project(s): Studied aneuploidy (destabilized karyotypes) in cancer cells and how aneuploidy influenced the progression of benign to malignant tumors

PEER REVIEWED JOURNAL PUBLICATIONS

2019

MB Applegate, Kavon Karrobi, J Angelo, W Austin, S Tabassum, E Aguénounon, K Tilbury, R Saager, S Gioux, D Roblyer, "*openSFDI: An open-source guide for constructing a spatial frequency domain imaging system.*" Journal of Biomedical Optics, 2019 (under review). *Companion website: www.opensfdi.org

Kavon Karrobi, A Tank, S Tabassum, V Pera, D Roblyer, "*Diffuse and nonlinear imaging of multiscale vascular parameters for in vivo monitoring of preclinical mammary tumors.*" Journal of Biophotonics, 2019 Jan 31; e201800379. PMID30706695.

2018

CK Hayakawa, Kavon Karrobi, V Pera, D Roblyer, V Venugopalan, "*Optical sampling depth in the spatial frequency domain.*" Journal of Biomedical Optics, 2018 Sep 14; 24(7), 071603. PMID30141285.

V Pera, Kavon Karrobi, S Tabassum, F Teng, D Roblyer, "*Optical property uncertainty estimates for spatial frequency domain imaging.*" Biomedical Optics Express, 2018 Feb 1; 9(2), 661. PMID29552403.

2014

T Ta, E Bartolak-Suki, EJ Park, Kavon Karrobi, NJ McDannold, TM Porter, "*Localized delivery of doxorubicin in vivo from polymer-modified thermosensitive liposomes with MR-guided focused ultrasound-mediated heating*." Journal of Controlled Release, 2014 Nov 28; 194:71-81. PMID25251982.

HONORS and FELLOWSHIPS

2017-2023	The NCI Predoctoral to Postdoctoral Fellow Transition Award (F99/K00, NIH)
2018	Photonics Center Travel Award, Boston University, Boston, MA
2018	Quantitative Biology and Physiology Best Presentation Award (Co-Winner)
2018	West End House Volunteer of the Year Award
2016	NSF CIRTL Teaching as Research Fellow
2015-2016	NIH T32 Training Fellowship, Quantitative Biology and Physiology
2014-2015	Boston University Distinguished Biomedical Engineering Fellowship
2013	Amgen Scholar UCSF
2012-2013	Boston University Undergraduate Research Opportunities Program
2012	Tau Beta Pi National Engineering Honor Society
2012	Alpha Eta Mu Beta National Biomedical Engineering Honor Society
2012	Boston University Photonics Center NSF REU
2010-2013	Boston University College of Engineering Dean's List (6 semesters)
2010-2014	Boston University Dean's Scholarship

ABSTRACTS and PRESENTATIONS

2019

Kavon Karrobi, A Pilvar, A Tank, K Doshi, DJ Waxman, D Roblyer, "*Towards in vivo preclinical monitoring of multiscale vascular structure-function relationships in resistant breast cancers with an integrated diffuse and nonlinear imaging system.*" SPIE Photonics West BiOS, 2019 Feb (San Francisco, CA); O*ral presentation*

2018

Kavon Karrobi, A Tank, S Tabassum, V Pera, D Roblyer, "*Diffuse and nonlinear imaging (DNI) of multiscale vascular parameters for in vivo monitoring of preclinical mammary tumors*." BU BME Quantitative Biology and Physiology Symposium, 2018 Dec (Boston, MA); O*ral presentation*

Kavon Karrobi, A Tank, S Tabassum, V Pera, D Roblyer, "*Diffuse and nonlinear imaging of multiscale vascular structure-function relationships for in vivo monitoring of breast cancer treatment resistance.*" GRC/GRS Lasers in Medicine and Biology, 2018 July (Lewiston, ME); *Poster presentation*

Kavon Karrobi, A Tank, S Tabassum, V Pera, D Roblyer, "*Diffuse and nonlinear imaging of multiscale vascular parameters for in vivo monitoring of breast cancer treatment resistance.*" NCI Subcellular to Cellular Cancer Imaging Workshop, 2018 April (Bethesda, MD); *Poster presentation*

Kavon Karrobi, MB Applegate, S Tabassum, D Roblyer, "*Diffuse and nonlinear imaging for in vivo multiscale preclinical monitoring of mammary tumors.*" SPIE Photonics West BiOS, 2018 Jan (San Francisco, CA); *Oral presentation*

2016

Kavon Karrobi, R Istfan, S Tabassum, Y Zhao, A Pant, C Hyakawa, V Venugopalan, D Roblyer, "*Multiscale preclinical imaging for the early prediction of tumor resistance to chemotherapy.*" BU Annual Photonics Center Symposium, 2016 Dec (Boston, MA); *Poster presentation*

2013

Kavon Karrobi, MT Burgess, T Ta, TM Porter, "*Engineering lipid-polymer hybrid nucleic acid delivery vehicles for gene therapy*." BMES Annual Meeting, 2013 Sept (Seattle, WA); *Poster presentation*

Kavon Karrobi, JT Sockolosky, M Spreafico, MP Jacobson, FC Szoka, "*Engineering a human-to-mouse species switch in the affinity of a neonatal Fc receptor (FcRn) binding peptide based on computational design*." UCSF SRTP Annual Symposium, 2013 July (San Francisco, CA); O*ral and Poster presentations*

TEACHING and MENTORSHIP

2019	BU BE700 Fluorescence in BME (Guest Lecture)
2019	BU BE700 Cancer Biology and Oncology for Engineers (Guest Lecture)
2017	BU BE700 Cancer Biology and Oncology for Engineers (Guest Lecture)
2017	BU STEM Exploration Day (Co-Director)
2016 Fall	BU BE401 Signals and Systems in BME Graduate Teaching Fellow
2016 Spring	BU BE436 Fundamentals of Fluid Mechanics Graduate Teaching Fellow
2015-2017	Mentor for undergraduate (UROP) and high school (RISE) BU research programs
2015-present	West End House Boys and Girls Club Boston STEM Tutor & Robotics Mentor
2014-2017	Boston University BME Graduate Student Council Outreach Chair
2013-2014	Boston University College of Engineering Tutor

PROFESSIONAL SERVICE

2014-present Ad hoc reviewer: Journal of Biomedical Optics, Biomedical Optics Express, Neoplasia, Cancer Research, Optics Letters

SOCIETIES

2017-present BU OSA/SPIE Student Chapter, Secretary and Outreach

2017-present SPIE, student member

2016-present OSA, student member

SKILLS

Optics: Diffuse Optical Imaging (e.g. Spatial Frequency Domain Imaging, SFDI), Multiphoton Microscopy, Beam alignment, Optical phantom fabrication, 3D printing, Flow cytometry, Dynamic light scattering

Molecular: Tumor animal models, Affinity chromatography, Nanoparticle fabrication, Zeta potential analyzer, Cell culture, Tissue sectioning and histology

Programming: MATLAB, ImageJ, LabVIEW, Arduino C

Languages: English, Intermediate Spanish